universität wien

DIPLOMARBEIT/ DIPLOMA THESIS

Titel der Diplomarbeit / Title of the Diploma Thesis

„Analysis of Isotopic Uranium and Plutonium Ratios in the Ocean by Accelerator Mass Spectrometry“

verfasst von / submitted by

Andreas Wiederin

angestrebter akademischer Grad / in partial fulfilment of the requirements for the degree of

Magister der Naturwissenschaften (Mag. rer. nat.)

Wien, 2020 / Vienna, 2020

Studienkennzahl lt. Studienblatt degree programme code as it appears on the student record sheet:	A 190 412 406
Studienrichtung lt. Studienblatt degree programme as it appears on the student record sheet:	Lehramtsstudium UF Physik UF Mathematik
Betreut von / Supervisor:	Univ.-Prof. Dipl.-Ing. Dr. Robin Golser

Abstract

The long-lived anthropogenic isotopes ^{239,240}Pu and ^{233,236}U have been released to the environment via nuclear bomb explosions as well as discharges both planned and accidental from nuclear power plants or fuel reprocessing plants. For the application of these isotopes as tracers for environmental processes, it is important to study their distribution and the relevant source terms in order to understand their physciochemical behavior in different compartments of the environment. Examples for such processes are water mass movements or sedimentation rates. There is very little data on the concentrations and isotopic ratios of plutonium and anthropogenic uranium in the Northeastern Pacific.

The environmental concentrations of ^{239,240}Pu, and the isotopic ratios ^{236}U/^{238}U and ^{233}U/^{236}U in seawater samples from various depths at two locations taken during the GEOTRACES cruise KH-17-03 in the eastern North Pacific were analyzed at the VERA AMS facility in Vienna. All ^{240}Pu/^{239}Pu ratios measured for the present study were compatible with a combination of global fallout with an isotopic ratio of 0.178 ± 0.014 (Krey et al. 1976) and tropospheric fallout from the Pacific Proving Grounds with ratios in the range of 0.24 to 0.34 (Buesseler 1997). Following a strong increase from the surface the depth profile from station CL-21 exhibits almost constant ^{239,240}Pu concentrations below 800m depth instead of the subsurface maximum typical for open seawater. This vertical distribution indicates relevant local effects contributing to the removal of plutonium from the water column in the eastern North Pacific. A previous study already reported a high vertical plutonium flux associated with a high concentration of particulate matter for the Northeast Pacific (Fowler et al. 1983). The complex seafloor topography with prominent seamounts, active underwater volcanoes, and the high seismic activity in the region may contribute to this effect most likely by increased

concentrations of biogenic and other particulate matter scavenging the particle reactive plutonium from the water column. Further samples from the region with additional data on suspended particulate matter and plankton activity are needed to explore these local effects.

The $^{236}U/^{238}U$ depth profiles show a maximum near the surface, followed by a steady decrease with depth. The $^{233}U/^{236}U$ depth profiles from stations CL-21 and CL-20 in the present study are the first ever obtained for an ocean water column. The $^{233}U/^{236}U$ ratios could only be measured reliably for the upper 800m of the water column. For the detection of ^{233}U in deeper water, a further reduction of the blank level is required. The isotopic uranium ratios measured are consistent with a decreasing influence of the anthropogenic isotopes ^{233}U and ^{236}U with depth and a constant ^{238}U concentration in the whole water column. The $^{233}U/^{236}U$ ratio for the CL-20 sampling station appears to be lower than that of CL-21. However, the difference is not statistically significant, and the ratios at both stations are compatible to those published in (Hain et al. 2020) for global fallout and support the hypothesis of large thermonuclear weapons tests as the main source for ^{233}U in the Pacific Ocean.

Zusammenfassung

Die langlebigen anthropogenen Isotope ^{239,240}Pu und ^{233,236}U wurden durch Atombombenexplosionen sowie durch geplante und unbeabsichtigte Emissionen aus Kernkraftwerken oder Brennstoff-Aufbereitungsanlagen an die Umwelt abgegeben. Für die Anwendung der Konzentrationen und Verhältnisse dieser Isotope als Tracer für Umweltprozesse wie Wassermassenbewegungen oder Sedimentationsraten ist es wichtig, ihre Verteilung in der Umwelt und die relevanten Quellen zu untersuchen, um ihr physio-chemisches Verhalten in unterschiedlichen Umgebungen zu verstehen. Über die Konzentrationen und Isotopenverhältnisse von Plutonium und anthropogenem Uran im Nordostpazifik liegen nur sehr wenige Daten vor.

Im Verlauf dieser Arbeit wurden die Umweltkonzentrationen von ^{239,240}Pu und die Isotopenverhältnisse ^{239}Pu/^{240}Pu, ^{236}U/^{238}U und ^{233}U/^{236}U in Meerwasserproben, die während der GEOTRACES-Forschungsfahrt KH-17-03 an zwei Positionen und in verschiedenen Tiefen im Nordostpazifik entnommen wurden, in der VERA AMS-Anlage in Wien analysiert. Alle für die vorliegende Studie gemessenen ^{240}Pu\$^{239}$Pu -Verhältnisse sind mit einer Kombination aus globalem Fallout mit einem Isotopenverhältnis von 0.178±0.014 (Krey et al. 1976) und troposphärischem Fallout von den Pacific Proving Grounds mit Verhältnissen im Bereich von 0.24 bis 0.34 (Buesseler 1997) kompatibel. Nach einem starken Anstieg ab der Oberfläche weist das Tiefenprofil der Station CL-21 anstelle des typischen Maximums in einigen Hundert Metern Tiefe nahezu konstante $^{239.240}$Pu -Konzentrationen ab einer Tiefe von 800 m auf. Diese untypische Verteilung weist auf relevante lokale Effekte hin, die zur vertikalen Bewegung von Plutonium in der Wassersäule im Nordostpazifik beitragen. Eine frühere Studie berichtete bereits 1983 über einen hohen vertikalen Plutoniumfluss in dieser Region, der mit einer hohen Partikelkonzentration korreliert ist (Fowler et al. 1983). Die komplexe Bathymetrie mit markanten Seeber-

gen, aktiven Unterwasservulkanen und die hohe seismische Aktivität in der Region könnten zu diesem Effekt beitragen, insbesondere durch erhöhte Konzentrationen von biogenen und anderen Partikeln, die das partikelreaktive Plutonium an sich binden. Weitere Proben aus der Region mit zusätzlichen Daten zu Schwebstoffen und Planktonaktivität sind erforderlich, um diese lokalen Effekte zu untersuchen.

Die $^{236}U/^{238}U$ Tiefenprofile haben ihr Maximum nahe der Oberfläche, gefolgt von einer stetigen Abnahme mit der Tiefe. Die $^{233}U/^{236}U$ Tiefenprofile von den Stationen CL-21 und CL-20 in der vorliegenden Arbeit sind die ersten, die jemals für eine Ozeanwassersäule erstellt wurden. Die $^{233}U/^{236}U$ Verhältnisse konnten nur für die oberen 800 m der Wassersäule bei CL-21 zuverlässig gemessen werden. Für den Nachweis von ^{233}U in tieferem Wasser ist eine weitere Reduzierung des Blanklevels erforderlich. Die $^{233}U/\ ^{236}U$ Verhaltnisse sind innerhalb der Unsicherheiten mit einem konstanten Verhaltnis in allen Tiefen kompatibel. Die gemessenen Uranverhältnisse passen zu einer annähernd konstanten ^{238}U-Konzentration in der Wassersäule, während der anthropogene Einfluss wie erwartet mit der Tiefe abnimmt.

Das Verhältnis $^{233}U/^{236}U$ für die CL-20-Probenahmestation scheint niedriger zu sein als das der CL-21 Proben, der Unterschied ist jedoch statistisch nicht signifikant. Die Isotopenverhältnisse an beiden Stationen sind kompatibel mit den in (Hain et al. 2020) Veröffentlichten für globales Fallout der Kernwaffentests und stützen die Hypothese großer thermonuklearer Waffentests als Hauptquelle für ^{233}U im Pazifik.

Contents

1 Motivation

Anthropogenic radionuclides have been produced for almost a century. Irene and Pierre Joliot-Curie discovered the first method for the creation of anthropogenic radionuclides by irradiation with alpha-particles in 1934 (Joliot et al. 1934). James Chadwick's discovery of the neutron (Chadwick 1932) and the advent of the particle accelerator also in the 1930s opened further avenues for the production of small quantities of various new anthropogenic radionuclides. The explanation of fission by Liese Meitner and Otto Frisch (Meitner et al. 1939) based on experiments by Otto Hahn and Fritz Strassmann with its potential for chain reactions gave rise to a thriving nuclear industry and military applications. Where anthropogenic radionuclides previously were extremely rare substances studied with great care in laboratories, vast amounts have been released into the environment since 1945. The most relevant sources for anthropogenic radionuclides in the environment were nuclear weapons testing and planned as well as accidental releases from nuclear reactors and the nuclear fuel cycle. Among these anthropogenic radionuclides are the uranium and plutonium isotopes studied in this thesis: ^{239}Pu, ^{240}Pu, ^{236}U, and ^{233}U.

These four are long-lived radionuclides, with ^{240}Pu having the shortest half-life at 6561 years. All are highly (radio-)toxic and ^{233}U and ^{239}Pu are fissionable materials. The potential hazards are one reason to closely monitor their release and distribution into the environment. While releases on the order of kilograms to tons are considered very large in the context of nuclear physics, these materials are quickly diluted in the atmosphere or the oceans, resulting in trace concentrations distributed over very large areas or even globally. While these trace amounts pose no immediate health hazard, increasingly sensitive measurement capabilities open up new uses for these isotopes as long-lived environmental tracers.

Accelerator mass spectrometry is an extremely sensitive method for analyzing trace amounts of these radionuclides in environmental samples. The $^{240}Pu/^{239}Pu$ ratio of a material depends on neutron flux and irradiation time during production and is therefore characteristic of the source. The contribution from different sources with well-known $^{240}Pu/^{239}Pu$ ratios can be calculated using a simple mixing model presented in 2.1.1. This enables the identification of the contribution of an additional unknown source if all other sources and their contribution are well known. Applications for this can be found in nuclear forensics or the monitoring of environmental releases from dumpsites, nuclear test sites, reprocessing plants, or reactor accidents even at large distances. Typical examples would be the quantification of plutonium fallout from the Fukushima accident into the Pacific Ocean (Hain et al. 2017)(Bu et al. 2014), or the Chernobyl accident into the Baltic Sea (Lindahl et al. 2005). The source terms for plutonium releases into the environment are typically well known (Lindahl et al. 2010) and the identification of their contributions to an environmental sample is the basis for the use of these plutonium isotopes as environmental tracers. Due to its non-conservative behavior in seawater, plutonium is scavenged by particles and quickly accumulated by organisms like plankton (Fowler et al. 1983).

In (Hain et al. 2017) one sample from the northeastern Pacific Ocean analyzed at VERA showed a $^{240}Pu/^{239}Pu$ ratio of 0.08 ± 0.02 compatible with weapons-grade plutonium. The estuary of the Columbia River located 770km from the sampling site makes the Hanford Site a potential source for this material, as the reactors there were used to produce large amounts of weapons-grade plutonium during the era of the cold war. Up to 25% of the plutonium in the Columbia river sediments was attributed to Hanford reactor operations (Beasley et al. 1984). While $^{240}Pu/^{239}Pu$ ratios down to 0.04 were measured in groundwater near the Hanford Site (Dai et al. 2005), the ratios in sediments downstream in the Columbia River are compatible with global fallout (Beasley et al. 1984). While this result combined with the distance to the sampling station makes the Hanford Site release hypothesis improbable it remains a possible local source for weapons-grade material. If a similar isotopic ratio can be confirmed, the depth profile and the two sampling stations might provide information on potential sources and re-mobilization of the

material. Finding no influence of additional sources would point to an artifact in the previous measurement, thus contributing to quality control and the constant improvement of the measurement procedures at VERA. The motivation behind the plutonium measurements in this thesis is therefore twofold: a follow-up to clarify the result reported in (Hain et al. 2017) and a general contribution to the knowledge about the distribution of these two plutonium isotopes in the Northeastern Pacific which helps to understand the migration of Pu in the environment. This is especially relevant, as there is very little data on the plutonium distribution in this region, even though (Fowler et al. 1983) already indicated local effects causing a comparably high vertical plutonium flux in the region.

Over the past two decades, the predominantly anthropogenic radionuclide ^{236}U has been established as an oceanographic tracer (Zhao et al. 1997 , Sakaguchi et al. 2012, Winkler et al. 2012). Uranium in seawater is far more conservative than plutonium, lending it a longer residence time and therefore range in the oceans. Bloch estimated the average residence time of uranium in the oceans at $2.3 \cdot 10^5$ years with an overall concentration of 3.3 ppb at a typical salinity of 35 psu (Bloch 1980). The primordial radionuclides ^{235}U and ^{238}U along with the latter‘s decay product ^{234}U are distributed almost uniformly in the oceans. Uranium both natural and anthropogenic is typically found in the form of the highly soluble uranyl carbonate ion $[UO_2(CO_3)_3^{4-}]$ in ocean water (Kusakabe 2017). While plutonium is best suited to track processes involving particle movements or biogeochemical processes as stated above, uranium in general and with it ^{236}U and ^{233}U is distributed mainly by diffusion, advection and the mixing of water masses.

Recent developments at VERA (Hain et al. 2020) have made the ^{233}U/^{236}U ratio accessible. Using this ratio in addition to the ^{236}U/^{238}U ratio allows to distinguish nuclear weapons fallout from reactor fuel-cycle emissions. To date there is a single ^{236}U/^{238}U depth profile from the northeast Pacific Ocean (Eigl et al. 2016) and none for the ^{233}U/^{236}U ratio. To maximize the use of the valuable GEOTRACES seawater samples, the ^{236}U/^{238}U and ^{233}U/^{236}U ratios were analyzed for all water samples in addition to ^{239}Pu, ^{240}Pu and the ^{240}Pu/^{239}Pu ratio in the course of this thesis to increase the knowledge about their environmental distribution.

2 Introduction

2.1 Sources for anthropogenic plutonium and uranium in the environment

Trace amounts of naturally occurring plutonium isotopes can be found in the general environment. In minerals with high uranium content like pitchblende a natural concentration of $m(^{239}\mathrm{Pu})/m(\mathrm{ore}) = 10^{-12}$ created by capture of ambient neutrons on ^{238}U was reported by Levine and Seaborg in 1950 (Levine et al. 1950). Even lower concentrations can be expected in the general environment due to the lower neutron flux and density of ^{238}U target nuclei outside uranium ores. In the waters of the Pacific Ocean, the natural plutonium is negligible compared to the anthropogenic plutonium.

The first anthropogenic plutonium was produced, isolated and identified as "Element 94" by Glenn T. Seaborg on December 14, 1940 at the cyclotron at the University of California, Berkeley (Seaborg et al. 1946). In reactors - beginning with the X-10 Graphite Reactor in 1943 - plutonium is primarily produced by neutron capture on ^{238}U followed by two subsequent beta decays to ^{239}Np and finally ^{239}Pu. The resonance integral for the (n, γ) neutron capture reaction on ^{238}U is (277 ± 3) b and the thermal neutron capture cross-section is (2.682 ± 19) b (IAEA 2020). Multiple successive neutron captures on the same nuclide form heavier isotopes of plutonium if they occur before the nuclide decays. Table 2.1.1 shows some characteristics of the plutonium isotopes relevant in this thesis based on (IAEA 2020).^{239}Pu has a probability of 73.5% to undergo spontaneous fission when capturing a thermal neutron, and a probability of $26,5\%$ to form ^{240}Pu.

Figure 2.1.1 (UN 2000) shows the total explosive yield for atmospheric and underground nuclear weapons tests for each year from 1945 to 2000. The same report estimates, that 10.87 PBq of ^{239}Pu and ^{240}Pu have been deposited in the oceans as the global fallout component of these tests. Nakano et al. estimated the tropospheric fallout component from the tests at Bikini and Enewetak test sites at 6 PBq ^{239}Pu and ^{240}Pu in (Nakano et al. 2003) based on exponential regression on surface soil samples from the Marshall Islands analyzed by Simon et al. (Simon et al. 1999). Tropospheric fallout is distributed downwind from the detonation or release site. The average residence time of particles in the troposphere was estimated at 30 days by Libby, with rain being the main removal mechanism (Libby 1958). Libby proposed the distribution of tropospheric fallout along bands around the globe, with a general decline with distance and a strong dependence on precipitation. While these narrow bands may be an oversimplification, it can be assumed, that most tropospheric fallout will be distributed along the atmospheric cell it was released in. This cell model of atmospheric circulation is illustrated in figure 2.1.2 from (Piana 2020)

Isotope	Half-Life [Yr]	Decay modes	$\sigma(n_{th}, \gamma)$ [b]	$\sigma(n, f)$ [b]
^{239}Pu	24110 ± 30	α,sf $(3 \cdot 10^{-10}\%)$	269.3	748.1
^{240}Pu	6561 ± 7	α,sf $(6 \cdot 10^{-6}\%)$	289.5	0.056
^{242}Pu	$(3.75 \pm 0.02) \cdot 10^5$	α,sf $(6 \cdot 10^{-4}\%)$	18.9	0.16

Table 2.1.1: Half-life in years, relevant decay modes and cross-sections for thermal neutron capture and thermal neutron induced fission in barn for ^{239}Pu, ^{240}Pu and ^{242}Pu. All three nuclides are primarily $\alpha-$emitters, the percentage undergoing spontaneous fission is given in the brackets (IAEA 2020).

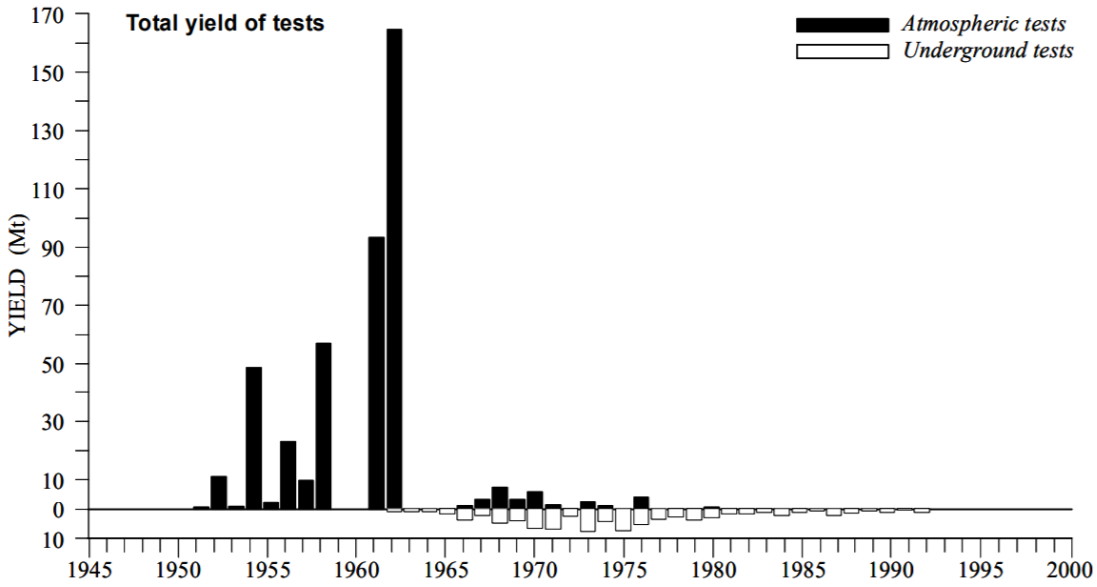

Figure 2.1.1: Total yield for atmospheric and underground nuclear tests in Megatons equivalent TNT taken from (UN 2000)

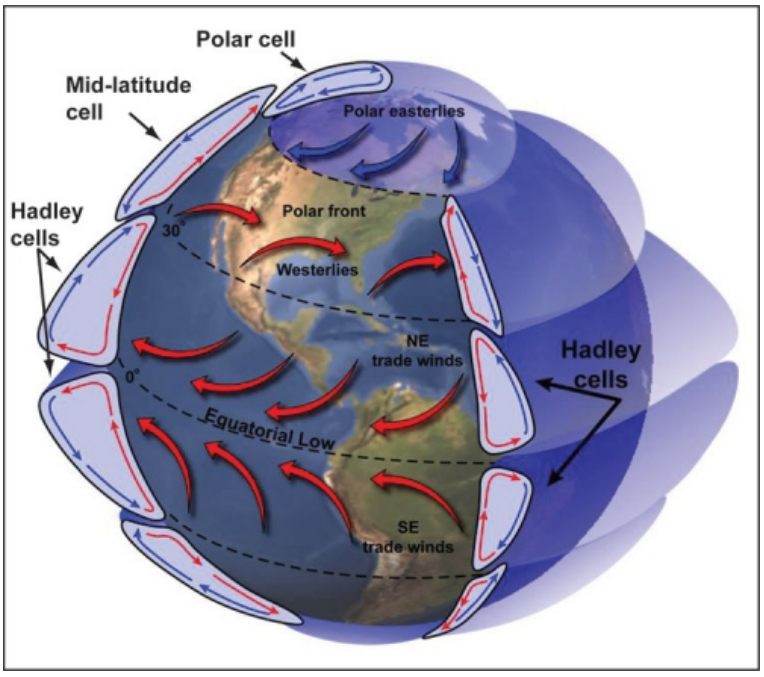

Figure 2.1.2: A simple model of atmospheric circulation in the troposphere with Hadley cells from the equator to 30°, the polar cells around the poles and the mid-latitude cells in between taken from (Piana 2020).

The US tests on Bikini and Enewetak were conducted mainly close to ground on small islands, so a large tropospheric fallout component estimated at 60% by Lee et al. can be expected, much of which would have entered the Pacific Ocean (Lee et al. 2005). The USSR mainly conducted high altitude tests, leading to increased global stratospheric and less tropospheric fallout (Buesseler 1997). With the easternmost USSR test site Semipalatinsk 3200 km and the Chinese test site Lop Nur 2500 km from the Pacific Ocean, it seems reasonable to assume that a much smaller fraction of the tropospheric fallout component from these test sites compared to the American island tests reached the Pacific. In total, the largest contribution to the plutonium content of the Pacific Ocean from tropospheric fallout can be attributed to the Bikini and Enewetak test sites, with an isotopic ratio of 0.24 - 0.34 (Buesseler 1997) against the 0.178 ± 0.014 in global fallout (Krey et al. 1976). This elevated ratio at the Pacific Proving Grounds (PPG) is mainly attributed to the high yield thermonuclear tests near or on the ground in the 1950s, like the Mike shot in 1952 with a $^{240}Pu/^{239}Pu$ ratio of 0.363 ± 0.004 (Diamond et al. 1960). The tropospheric fallout component in the Pacific Ocean and with it the $^{240}Pu/^{239}Pu$ isotopic ratio is largest near the test sites and along the main ocean current system passing the test sites consisting of the North Equatorial Current and the Kuroshio (Wu et al. 2019). The sampling stations analyzed for this thesis lie between this North Pacific Current and the Subpolar Gyre fed by this major current, so a contribution from the PPG and with it an elevated ratio compared to global fallout is expected. Due to the non-conservative behavior of plutonium in seawater and the large distance along the currents the tropospheric component is likely to be reduced compared to samples closer to the PPG.

In addition to fallout from weapons testing, releases from fuel production and processing plants and nuclear power plant accidents may contribute to the plutonium in the Pacific Ocean. Based on (Hain et al. 2017) and (Wu et al. 2019), the Fukushima Daiichi nuclear power plant accident did not contribute significantly to the plutonium inventory of the Pacific. The IAEA reports in (IAEA 2006) that 0.013 PBq ^{239}Pu and 0.018 PBq ^{240}Pu were released to the environment during the Chernobyl nuclear accident, with most of it being deposited in the immediate vicinity in fuel element fragments. Due to the large distance and low quantity com-

pared to the nuclear weapons tests, no significant contribution to the plutonium inventory of the Pacific Ocean is expected from Chernobyl.

Reprocessing plants can be a significant source for actinides in the environment. Gray et al. report a maximum annual discharge of 0.55 PBq from the Sellafield reprocessing Plant in Great Britain into the Irish Sea in 1974 (Gray et al. 1995). The discharges had a wide range of isotopic ratio for $^{240}Pu/^{239}Pu$ from 0.05 to 0.25 depending on whether the plant was used for weapons-grade plutonium separation or fuel reprocessing at the time (Lindahl et al. 2010). Transport from Sellafield via the Arctic Ocean to the Pacific will be small, as the water generally flows from the Pacific Ocean through the Bering Strait towards the Arctic, not the other way around (Loughlin et al. 1999). No significant plutonium discharges have been reported for the Tokai reprocessing plant located on the east coast of Japan.

There is very little data on ^{239}Pu and ^{240}Pu releases from the Hanford Site. Beasley and Jennings estimated the proportion of plutonium originating from Hanford in sediments near the Columbia River estuary at 3.5% in 1984 (Beasley et al. 1984), indicating a small but noticeable local influence. Further upstream, in the McNary Reservoir the Hanford Site influence was estimated at 25%, indicating a significant input into the Columbia River, but also a fast removal by sedimentation of carrying particles that transported more than 90% of the $^{239}Pu+^{240}Pu$ activity. This indicates the potential for remobilization from sediments either mechanically or through a change in chemical conditions in some parts of the river, that may have increased the contribution near the estuary since 1984. The main purpose of the Hanford reactors was the production of weapons-grade plutonium. Dai et al. found $^{240}Pu/^{239}Pu$ ratios in the range of 0.04 to 0.15 in groundwater samples in and around the Hanford Site and explained this range with a varying combination of global fallout and discharges from the Hanford Site reactors and PUREX plant (Dai et al. 2005). Based on this result, the ratio of 0.04 can be assumed an lower bound for the isotopic ratio of the weapons-grade plutonium produced at the Hanford Site as the plutonium detected in the ground water could be already a mixture with global fallout plutonium. Table 2.1.2 gives an overview of the $^{240}Pu/^{239}Pu$ ratios of plutonium released by the sources discussed above.

Source	$^{240}Pu/^{239}Pu$
Pacific Proving Grounds	0.24 - 0.34 [1]
Chernobyl NPP	0.408 ± 0.003 [2]
Fukushima NPP	0.323 ± 0.017, 0.330 ± 0.032 [2]
Hanford Site	≤ 0.04[3]
Sellafield Reprocessing Plant	0.05 - 0.25 [4]
Nevada Test Site	0.032 ± 0.003 [5]
Global fallout	0.178 ± 0.014 [6]

Table 2.1.2: $^{240}Pu/^{239}Pu$ atomic ratio for various sources. [1] (Buesseler 1997), [2] (Zheng et al. 2012), [3] (Dai et al. 2005), [4](Gray et al. 1995) [5](Hicks et al. 1984) [6](Krey et al. 1976)

If n sources with characteristic $^{240}Pu/^{239}Pu$ ratios R_i have contributed to an environmental sample with a factor x_i, then the ratio R_s for the sample can be calculated according to a simple linear mixing model (Lindahl et al. 2010) as

$$\begin{aligned} R_s &= x_1 R_1 + ... + x_n R_n \\ 1 &= x_1 + ... + x_n \end{aligned} \tag{2.1.1}$$

This system of two linear equations in 2n+1 variables can be used to calculate two unknown variables if the remaining 2n-1 are known. Most plutonium samples have a contribution by global fallout and one additional relevant local source, with more complicated situations in some cases like the Arctic Ocean and the Baltic Sea (Lindahl et al. 2010).

^{236}U, a radionuclide with a half-life of $2.342 \cdot 10^7$ years (IAEA 2020) can be formed via (n, γ) thermal neutron capture on ^{235}U, the $^{238}U(n, 3n)^{236}U$ reaction involving fast neutrons or the $\alpha-$decay of ^{240}Pu. The thermal neutron cross-sections of ^{235}U are $\sigma[^{235}U(n, f)] = 583\,b$ and $\sigma[^{235}U(n, \gamma)^{236}U] = 98\,b$ (IAEA 2020) so in about one of six times a thermal neutron interacts with a ^{235}U nucleus, ^{236}U is formed. This reaction can occur either in the environment due to ambient

neutrons of either cosmogenic or nucleogenic origin or in nuclear fuel elements during burn-up. The pre-anthropogenic $^{236}U/^{238}U$ ratio is in the range of 10^{-10} to 10^{-14} (Zhao et al. 1997) depending on the ^{235}U concentration and neutron flux of the specific environment. The same ratio reaches up to 10^{-2} in spent nuclear fuel (Steier et al. 2008). Due to this difference of up to 12 orders of magnitude the $^{236}U/^{238}U$ ratio in environmental samples is very sensitive to the influence of anthropogenic uranium. The pre-anthropogenic ^{236}U abundance was estimated in (Steier et al. 2008) at 1.5 kg in recoverable uranium ores, an additional 22 kg in the upper 1000 m of land surface and less than 0.5 kg in the oceans. The total anthropogenic ^{236}U was estimated at 10^6 kg. While most of the reactor produced ^{236}U is still contained in fuel elements, releases can drastically alter the environmental isotopic ratios. In (Casacuberta et al. 2014) the releases from the two largest reprocessing plants, Sellafield (UK) and La Hague (France) are estimated at 115 kg of ^{236}U, whereas (Castrillejo Iridoy et al. 2020) revises the numbers for Sellafield alone to (165 ± 15) kg for the period from 1971-1976 and (72 ± 6) kg since 1985. This makes the two reprocessing plants a relevant local source of ^{236}U in the Atlantic Ocean.

Small amounts of ^{236}U were released from the Fukushima reactor accident in 2011. based on ICP-MS measurements of soil samples Yang reports ^{236}U activities in the range of $(0.469 - 24.4) \cdot 10^{-5}$ Bq kg^{-1} and $^{236}U/^{238}U$ ratios of $(0.099 - 1.35) \cdot 10^{-7}$ (Yang et al. 2017). Sakaguchi et al. reported a total release of $1.2 \cdot 10^6$Bq ^{236}U activity for the reactor accident. This was based on AMS measurements of ^{236}U, $^{239,240}Pu$ and $^{134-137}Cs$ in black colored road dusts in high radiation areas near the reactor and a previous result on the total amount of ^{137}Cs released. (Sakaguchi et al. 2014)

The is very little specific data on the impact of local reprocessing plants to the inventory of radionuclides in the Pacific. In a review paper on artificial radionuclides in the western North Pacific Hong only lists one paper that addressed the issue (Hong et al. 2004). In this paper Cooper et al. found no evidence for an additional local source of ^{129}I in the western North Pacific or the Sea of Japan (Cooper et al. 2001). A literature search revealed no publication mentioning the Japanese reprocessing plant at Tokai as a relevant source for radionuclides in the

Pacific. Sakaguchi et al. found no indication for additional ^{236}U sources in the Sea of Japan (Sakaguchi et al. 2012), neither did Eigl et al. in the North Pacific Ocean (Eigl et al. 2016). A local contribution from the Hanford Site to the northeastern Pacific Ocean can not be excluded based on the scarce data available. In (Zachara et al. 2007) a total of 200.000 kg of uranium of varying isotopic composition is reported to have been released to the vadose zone in and around the Hanford Site, and ^{236}U/^{238}U ratios of up to $7.870{\cdot}10^{-5} \pm 0.16\%$ are reported for sediment close to underground storage tanks. The author is not aware of any published ^{236}U data in the Columbia River or its estuary.

Nuclear weapons involving highly enriched ^{235}U will also produce ^{236}U via neutron capture, while for large thermonuclear weapons the fast neutron reaction becomes predominant. The ^{3}He(d, n)He reaction in the fusion stage of such a weapon produces 14 MeV neutrons. The cross-section for the ^{238}U$(n, 3n)^{236}$U reaction for neutrons around 14 MeV is in the range of 0.4 b to 0.6 b (Wang et al. 2013) and large amounts of natural uranium consisting mainly of ^{238}U were used as tamper in the third stage of the Teller-Ulam design (Sublette 2020). The global ^{236}U inventory due to weapons fallout has been estimated at 900 kg (Sakaguchi et al. 2012) and 1060 kg (Winkler et al. 2012). The local fallout for the Pacific Ocean has been estimated at 240 kg in the latter publication.

The decay of global fallout ^{240}Pu to ^{236}U contributes to the ^{236}U inventory. In (Sakaguchi et al. 2009) this was estimated to result in a ^{236}U/^{238}U ratio of $2.6{\cdot}10^{-12}$ to $5.3 \cdot 10^{-11}$ for Japanese soil with 4-80 Bq/m^2. In the oceans this activity is not concentrated in a thin layer as in soil but spread out over the whole water column through diffusion, scavenging and advection. Consequently, the contribution of ^{240}Pu decays can be neglected for the ^{236}U measurements.

^{233}U is either formed by the thermal neutron capture reaction on ^{232}Th, or via (n,2n) or (n,3n) reactions involving fast neutrons. The ^{232}Th(n,γ)^{233}Th reaction has a cross-section of (7.35 ± 0.03)b followed by two beta decays with intermediary half-lifes of 21.83 minutes and 26.975 days first to ^{233}Pa and finally to ^{233}U (IAEA 2020). Reactions with fast neutrons potentially open up three additional production paths for ^{233}U.

The formation of ^{237}Np via the ^{238}U(n,2n)^{237}U reaction followed by the β^- decay ^{237}U$\rightarrow^{237}$Np has a 6MeV threshold for the (n,2n) reaction (Tsaletka et al. 1960). ^{237}Np decays to ^{233}Pa with a half-life of $(2.144 \pm 0.007) \cdot 10^6$ years, from which a final β^- decay yields ^{233}U. The cross-section is between 0.5b and 1.5b in the energy range of 7-15MeV (Gorbachev et al. 1980). A similar (n,2n) reaction on ^{234}U with the same threshold energy but cross-sections between 0.2 b and 0.7 b in the same energy range directly yields ^{233}U. Finally the ^{235}U(n,3n)^{233}U reaction requires an even higher neutron energy, and (Gorbachev et al. 1980) report cross-sections of (0.023 ± 0.062) b for 12.4 MeV and (0.114 ± 0.021) b for 14.1 MeV neutrons.

Only a small fraction of neutrons - mainly from cosmic rays and resulting spallation reactions - in the environment will reach the threshold energy for the (n,2n) or even (n,3n) reactions, so the largest pre-anthropogenic contribution will be from thermal neutron capture on ^{232}Th due to it's high abundance, followed by the decay chain resulting from the ^{238}U(n,2n)^{237}U reaction. ^{233}U/^{238}U ratios of $(1.3 \pm 0.2) \cdot 10^{-13}$ in pitchblende and $(4 \pm 2) \cdot 10^{-11}$ in monazite were reported in (Peppard et al. 1952), whereas for yellowcake the ratio was shown to be in the order of 10^{-14} in (Hain et al. 2020). In contrast to natural ^{236}U and ^{239}Pu this production pathway might be a relevant source of natural ^{233}U, especially in areas with a high ^{232}Th concentration.

For anthropogenic ^{233}U the first and the last of these four production paths are most relevant, as the long half-life of ^{237}Np and the low ^{234}U concentration in nuclear weapons or fuel as well as the small cross-sections limit the contributions from the remaining two paths. In nuclear power reactors only 2.4% and 0.01% of the fission neutrons reach the threshold energies for the (n,2n) and (n,3n) reactions (Madland 1982). In combination with the small reaction cross-sections compared to the 98 b for the ^{235}U(n,γ)^{236}U reaction described above, the production of ^{233}U can be assumed to be much lower than that of ^{236}U in typical nuclear reactors. A mass of $5.626 \cdot 10^{-3}$ g ^{233}U and $4.219 \cdot 10^3$ g ^{236}U has been reported for spent fuel with 38.6 GWd/MTU from Surry Nuclear Power Plant based on ORIGEN-ARP calculations (Naegeli 2004). When the masses of the two nuclides are taken into consideration, this results in a ^{233}U/^{236}U ratio of $\approx 1.35 \cdot 10^{-6}$.

^{233}U has been bred from ^{232}Th on a small scale and used in experimental reactor designs in several countries, including Germany, the USA, Great Britain and most recently India. Roughly 2 tons of ^{233}U were produced in the USA, mainly at the Hanford Site. In 2013 as much as 96 kg of ^{233}U from that program were unaccounted for (Alvarez 2013). Some of this lost ^{233}U might have leaked into the environment. According to (Zachara et al. 2007) small quantities of ^{232}Th were also used in some Hanford Site reactors to flatten the neutron flux, so even fuel elements not connected to the ^{233}U production might show elevated ^{233}U/^{236}U ratios compared to other facilities.

In thermonuclear weapons the fusion stage creates an abundance of fast neutrons, and combined with the presence of highly enriched ^{235}U in at least some of the designs used, this might have lead to a much more efficient ^{233}U production via the ^{235}U(n,3n)^{233}U reaction. In (Hain et al. 2020) the average ^{233}U/^{236}U ratio for global fallout has been established as $(1.40 \pm 0.15)\%$. Local and tropospheric fallout from detonations at low altitude may also exhibit increased ^{233}U/^{236}U ratios due to neutron capture on ^{232}Th present at $\approx$ 3ppm on the ground (Child et al. 2013).

According to (Hansen et al. 2007) several nuclear weapons tests used ^{233}U or a mixture of fissile materials containing ^{233}U. Hanson quotes internal US government documents released due to the freedom of information act indicating the requisition and use of ^{233}U in the test series Operation Teapot in 1955 at the Nevada Test Site as well as operations Redwing in 1956 and Hardtrack in 1958 in the Pacific Proving Grounds. US government memos also quoted in the same Book indicate some limited use of added ^{233}U in soviet weapons high yield tests in 1953 and 1955. Information about nuclear weapons testing is however still very scarce and usually not verifiable. Only one low yield (22 kT) test during Operation Teapot in 1955 is mentioned in various other sources like (Sublette 2020) and generally accepted. This test or possible tests might act as significant sources of local and tropospheric ^{233}U fallout while high altitude tests would have contributed to global fallout. In the course of the establishment of ^{233}U as an environmental tracer, it would be beneficial to investigate this matter by analyzing the ^{233}U/^{236}U ratios in samples where a strong local contribution from these tests can be expected.

2.2 Chemistry and environmental behavior of uranium and plutonium

Plutonium and uranium are elements of the actinide series of the periodic table, spanning from thorium to californium. Actinides together with the lanthanides located in the row above them in the periodic table form the inner transition metals. The elements of both groups have f orbitals (4f for lanthanides and 5f for actinides) in the valence shell. As the 4f orbital of the lanthanides is located deep within the structure of the lanthanide atoms, its electrons are not readily available for interactions and the chemical behavior is very similar to that of lanthanum. For the significantly heavier actinides relativistic effects become increasingly relevant, especially for the innermost orbitals. The contracted inner s and p orbitals provide increased shielding for the outer d and f orbitals from the positively charged nucleus, resulting in an expansion of these orbitals. For the lighter actinides this enables the 5f valence electrons to participate in chemical bonding. Rising charge over the course of the actinide series countermands this effect through the actinide contraction estimated at roughly 0.02Å between each element (Clark 2000).

For thorium the energy level of the 6d orbitals is below that of the 5f orbitals in the ground state. From over the light actinides from protactinium over uranium to neptunium these energies invert and for the light actinides a $[\mathrm{Rn}]5\mathrm{f}^{n-1}6\mathrm{d}^{1}7\mathrm{s}^{2}$, $n \in \{2, 3, 4\}$ configuration is observed. The single d electron is available for chemical bonds and leads to complex chemical behavior similar to the transition metals. For heavier actinides beginning with americium, the gap widens sufficiently to stabilize the ground state configuration $[\mathrm{Rn}]5\mathrm{f}^{n}7\mathrm{s}^{2}$, with fewer oxidation states and a somewhat simpler chemistry (Clark 2000). Plutonium lies between these two subgroups of the actinides, and with several electronic configuration near degeneracy and the above-mentioned delocalization of the 5f orbitals it exhibits the most complex behavior of any element (Clark 2000).

The chemical behavior of actinides is mainly influenced by the oxidation state they are in, with very similar behavior for different actinides in the same oxidation states. The oxidation states III+ through VI+ have been observed for plutonium in typical environmental conditions (Cleveland 1979). They can all coexist in aqueous

solution simultaneously, and even in comparable concentrations. Plutonium is the only known element with this property, and its chemistry is accordingly complex. Table 2.2.1 lists these states along with the corresponding ions and effective charges in aqueous solutions (Cleveland 1979).

Oxidation state	III+	IV+	V+	VI+
Corresponding ion	Pu^{3+}	Pu^{4+}	PuO_2^+	PuO_2^{2+}
Effective charge	+3	+4	+2.2	+3.3

Table 2.2.1: Oxidation states, effective charges and corresponding ions for plutonium in aqueous solutions based on data from (Runde 2000)

At trace concentrations typical of environmental samples, all plutonium-plutonium reactions like disproportionation, polymerization or plutonium-colloid formation (Runde 2000) can be neglected, as they will be dominated by other processes like the adsorption of plutonium onto other colloids due to the low interaction rate. The effects of radiolysis and the energy deposited in the system by decays can also be neglected. Whilst this removes some of the complications of plutonium chemistry, there still remain four relevant oxidation states that are heavily dependent on the environment of the plutonium atoms.

According to (Runde 2000) plutonium in seawater is likely to be either in the IV+ or V+ state. The IV+ state due to its highest effective charge (see table 2.2.1) either forms very stable complexes like $Pu(OH)_4$ or is absorbed on surfaces or suspended particles, leading to comparably fast sedimentation. The reduced effective charge for the V+ and VI+ states is due to the rapid formation of the trans-dioxo plutonyl cations PuO_2^+ and PuO_2^{2+} in aqueous solution. Plutonium V+ has the lowest effective charge of the relevant oxidation states, and typically remains dissolved in water (Runde 2000).

The rate by which plutonium sinks from the top layers is positively correlated with the total mass flux, biological and otherwise. In (Wilson et al. 2009) concentration factors of 3.1 ± 10^5 for plutonium in plankton were published, demonstrating the importance of biological uptake in general and the excretions of plankton in particular for the vertical plutonium flux in the oceans. The biological particles

decompose after some time and release the plutonium back into the water. Some non-biological particles react to the change of chemical conditions encountered at various depths and may decompose, while others are stable and carry the adsorbed plutonium straight to the seafloor. A combination of suspension, scavenging and partial re-suspension leads to a typical vertical distribution of plutonium in the open sea as shown in figure 2.2.1. Typical plutonium profiles from surface deposition are characterized by a pronounced subsurface maximum at a depth between 600 m and 1000 m. Over time after the deposition the maximum sank and became less pronounced. This can be explained by the processes described in the previous paragraph. Introducing a very high mass flux of particulate matter typical for coastal regions alters this pattern drastically as can be seen in figure 2.2.2 showing a depth profile from the DYFAMED station in the Mediterranean Sea (Lòpez Lora 2019). An extensive introduction to uranium chemistry can be found in (Morss et al. 2011) that was used for the following description of the most relevant chemical properties of this element. The IV state in the form of the U^{4+} ion acts as a strong acid in aqueous solutions and is stable when no oxidation agents are present. The VI+ state in the form of the linear uranly(VI+) ion UO_2^{2+} is the most stable in aqueous solutions. As with plutonium the stability of the oxidation states is heavily influenced by the presence of complexing ligands and the pH value of the solution. Redox reactions that only involve electrons are fast, whereas those involving a change in chemical composition are much slower.

In alkaline to moderately acidic conditions compounds involving U^{4+} are insoluble, whereas the hexavalent UO_2^{2+} creates highly soluble complexes with a variety of potential ligands like carbonate, hydroxide or oxalate. In seawater, almost all uranium is in the VI+ state, typically in the form of the highly soluble complex $UO_2(CO_3)_3^{4-}$ (Krishnaswami et al. 2016) and consequently behaves much more conservative than plutonium in the oceans. UO_2^{2+} when not shielded inside this carbonate complex can be adsorbed by various suspended particulates like SiO_2 (Mahmoud 2018) or efficiently coprecipitated with iron hydroxide (Qiao et al. 2015). The average residence time in ocean waters of $2.3 \cdot 10^5$ years (Bloch 1980) allows for an almost uniform distribution of uranium in seawater with a linear dependence on the salinity (Owens et al. 2011).

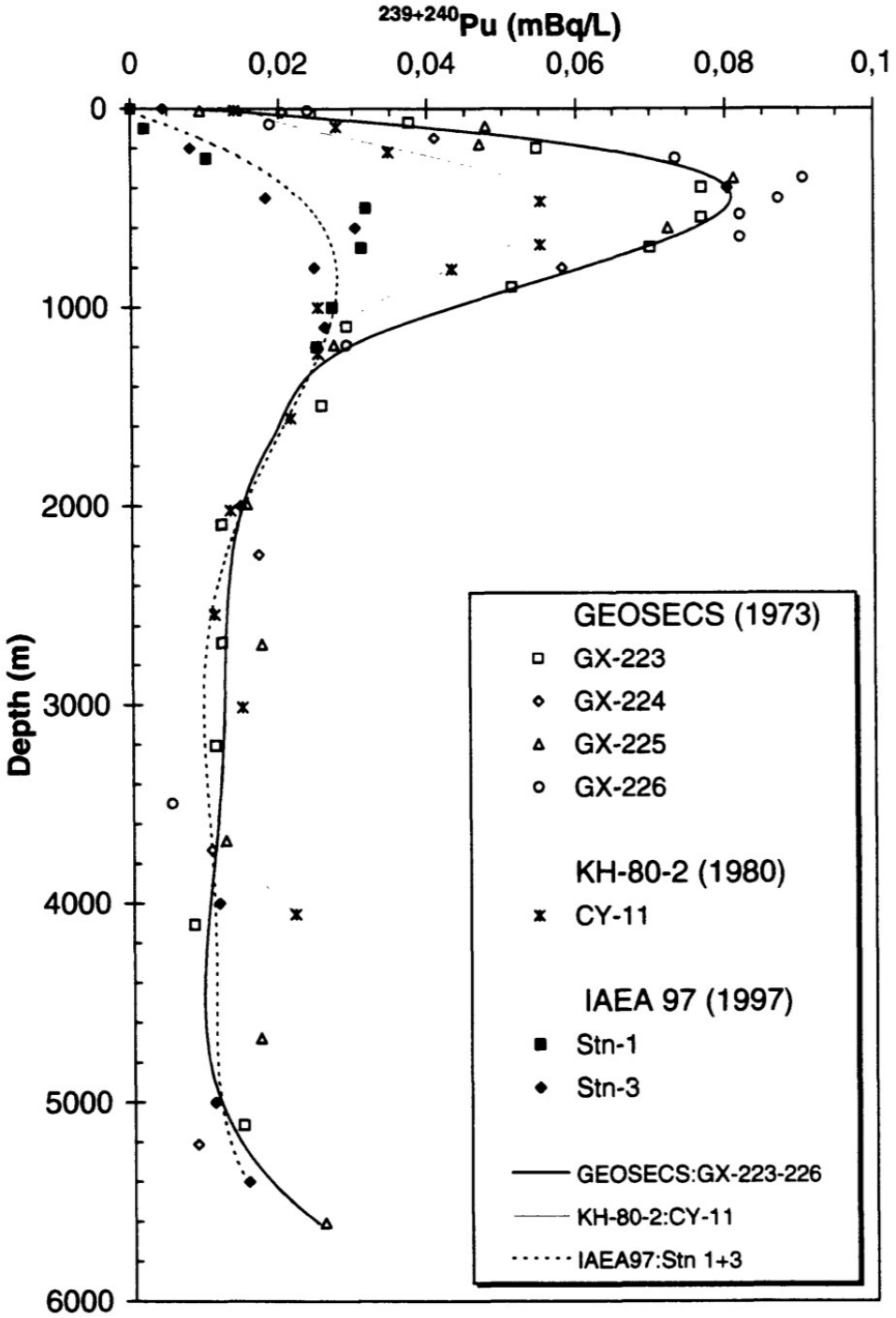

Figure 2.2.1: Depth profiles for the $^{239+240}$Pu activity for several exemplary sampling stations in the Pacific (Livingston et al. 2001). The fit curves show the spreading out and sinking of the subsurface maxima from 1973 to 1997. For information about the sampling locations see 5.6

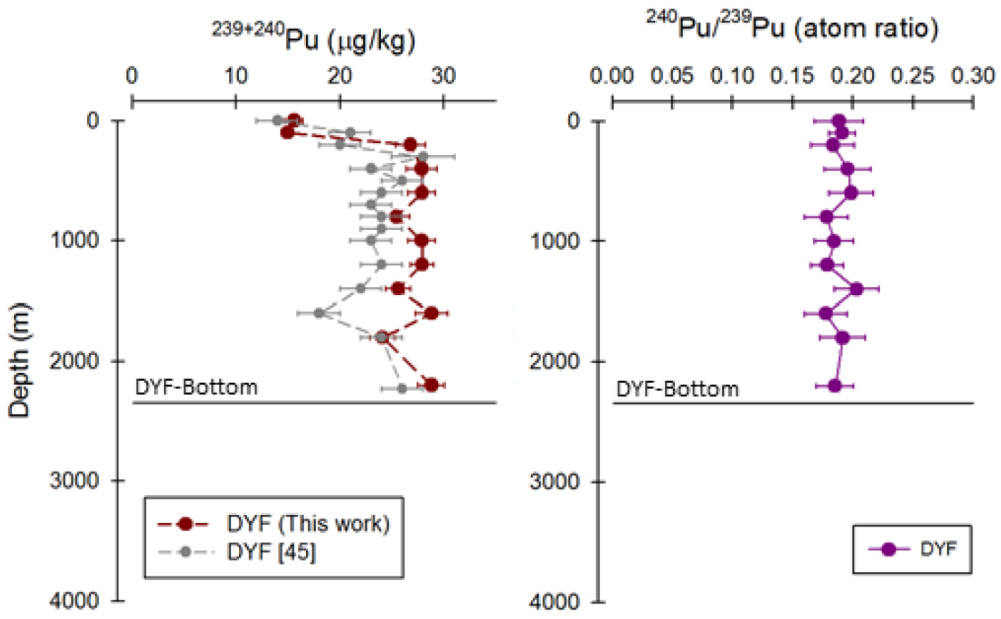

Figure 2.2.2: $^{239+240}$Pu concentration and ^{240}Pu/^{239}Pu at DYFAMED station in the Mediterranean Sea 45 km southeast of Niece (Lòpez Lora 2019)

The most notable isotopic fractionization effect is an elevated ^{234}U concentration. The recoil from the α decay that increases mobility and therefore the solubility in ground- and seawater for this nucleus. In (Chen et al. 1986) the average ^{234}U/^{238}U ratio in seawater was determined at 144 ± 2 ‰ (2σ) above the radiative equilibrium ratio of $5.472 \cdot 10^{-5}$.

While the concentration of uranium from natural sources is almost constant if normalized to a salinity of 35 psu in the water column, anthropogenic uranium has not had enough time for such an even distribution. Due to the conservative behavior of the uranyl ion, it is mainly transported through diffusion and advection. The main inputs of anthropogenic uranium were either fallout from weapons tests deposited on the surface or near surface liquid discharges from reprocessing plants. Consequently, the concentration of ^{236}U is typically highest at or near the surface and decreases rapidly. A ^{236}U depth profile from the Japan Sea taken from (Sakaguchi et al. 2012) is shown in figure 2.2.3 and exemplifies the typical vertical distribution of ^{236}U in ocean waters. Based on either a normal distribution

eddy diffusion model (plot A) or a difference method fit (plot B) diffusion rates of 5.6 cm^2/s and 4.2 cm^2/s for ^{236}U were calculated and are comparable to other conservative nuclides such as ^{137}Cs according to Sakaguchi et al. Due to the almost constant ^{238}U content, $^{236}U/^{238}U$ ratios as determined in the course of this work can be expected to follow the same pattern.

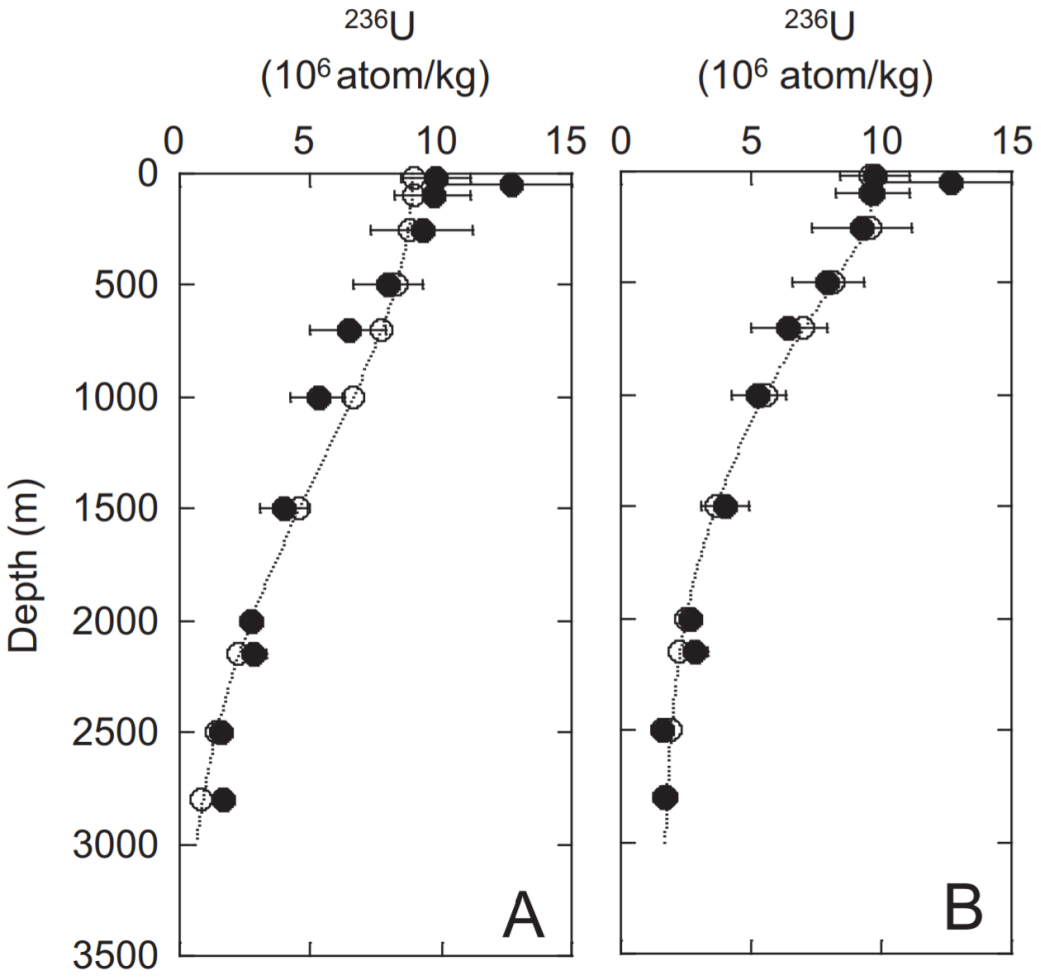

Figure 2.2.3: ^{236}U depth profile from the Japan Sea from (Sakaguchi et al. 2012). Filled circles represent data points from water samples, while the open circles and the dashed line represent two different models fitted in plots A and B.

3 Environmental samples and chemical sample preparation

3.1 The seawater samples

The samples analyzed in this thesis were collected during the GEOTRACES cruise KH-17-03 from Tokyo to Vancouver between 23 June and 7 August 2017. GEOTRACES is an international project operating sampling cruises with the aim of studying the biogeochemical processes involving trace elements and isotopes in the marine environment.

The ship Hakuho Maru hosts 10 dedicated research rooms and extensive equipment for sampling. In total 18 samples with a volume of 5L each, from two different sampling stations, i.e. CL-20 and CL-21, have been provided to VERA by Aya Sakaguchi (University of Tsukuba, Japan). All of these samples, which were collected at different depths, have been analyzed within the scope of this thesis.

Table 3.1.1 contains some basic information on the two sampling stations. Their locations, as well as those of the previously analyzed BD17 sample, the Columbia River Estuary and the Hanford Site are marked on a map created with Google Earth Pro shown in figure 3.1.1. GEOTRACES samples are acidified with 6M HCl to pH ≈ 2 on the ship to minimize the sorption of plutonium on the surface of the canisters and inhibit organic growth during shipping and storage (GEOTRACES 2010).

Station	Lat.	Long.	max. Depth [m]	Dates	Samples
CL-20	46° 59.96' N	134° 56.98' W	3600m	8/1/2017	4
CL-21	47° 00.00' N	130° 59.96' W	3100m	8/3/2017	14

Table 3.1.1: Coordinates, maximum depth, date of sampling and number of available samples for the two sampling stations CL-20 and CL-21 analyzed in the present study

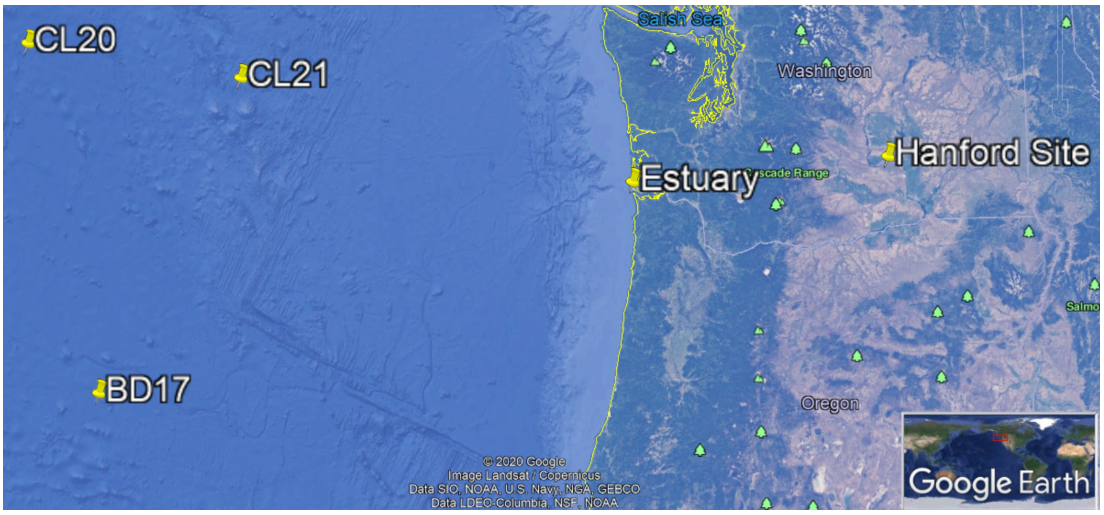

Figure 3.1.1: The map created with Google Earth Pro shows the locations of the two stations CL-20 and CL-21 analyzed for this thesis along with the BD17 station from the previous measurement (Hain et al. 2017). The Hanford Site and the Columbia River estuary are also marked as a potential source and pathway for anthropogenic actinides.

At sampling station CL-21 14 samples from surface to 3087m depth near the seafloor were taken, while for CL-20 only four samples from the surface to 600 m were available. Tables 3.1.2 and 3.1.3 contain the depth, the chemistry batch (three samples and one process blank were prepared in parallel as a batch), sample mass and number of ^{242}Pu atoms added as spike for all CL-21 and CL-20 samples. For both stations the salinity (stated in psu which is equivalent to ppt concentration), dissolved oxygen concentration (in μmol/kg) and the temperature (in °C) were measured against the pressure (in decibar). An one-meter increase in depth translates to a 1 db increase in pressure in pure water. For ocean water other factors such as temperature, salinity or the dependence of gravity both on the depth and the geographic position on the geoid earth complicate this simple depth-pressure relation depending on the accuracy required. Exemplary calculations for 1000 db and 3000 db based on recommendations in (Fofnoff 1983) show deviations of 11 m and 46 m respectively from the simple 1:1 conversion which is negligible for the purpose of showing the general trends for salinity, dissolved oxygen and temperature in the water column. For the sake of clarity and ease of comparison to the sampling depths instead of the pressure in decibars the depth in meters is used in the remainder of this section. As these measurements were done with different equipment than the sampling, the depths of these measurements and that of the samples are not equivalent but shows the general trends of the named quantities with increasing depth. Figure 3.1.2 shows depth profiles for the salinity and dissolved oxygen (left) and the salinity and the temperature (right) for CL-21 and CL-20 respectively.

Depth (m)	Name	Batch	Mass (g)
0	CL-21_0	4	5379 ± 10
20	CL-21_20	1	5329 ± 10
60	CL-21_60	3	5598 ± 10
100	CL-21_100	2	5342 ± 10
200	CL-21_200	5	5019 ± 10
300	CL-21_300	1	5551 ± 10
500	CL-21_500	2	5611 ± 10
800	CL-21_800	3	4866 ± 10
1000	CL-21_1000	2	5508 ± 10
1500	CL-21_1500	3	5058 ± 10
2000	CL-21_2000	1	5645 ± 10
2500	CL-21_2500	4	5406 ± 10
3000	CL-21_3000	4	5426 ± 10
3087	CL-21_3087	5	5125 ± 10

Table 3.1.2: Depth, name, chemistry batch and mass for each sample from CL-21

Depth [m]	Name	Batch	Mass [g]
0	CL-20_0	6	5022 ± 10
300	CL-20_300	6	4991 ± 10
400	CL-20_400	5	5100 ± 10
600	CL-20_600	6	5006 ± 10

Table 3.1.3: Depth, name, chemistry batch and mass for each sample from CL-20

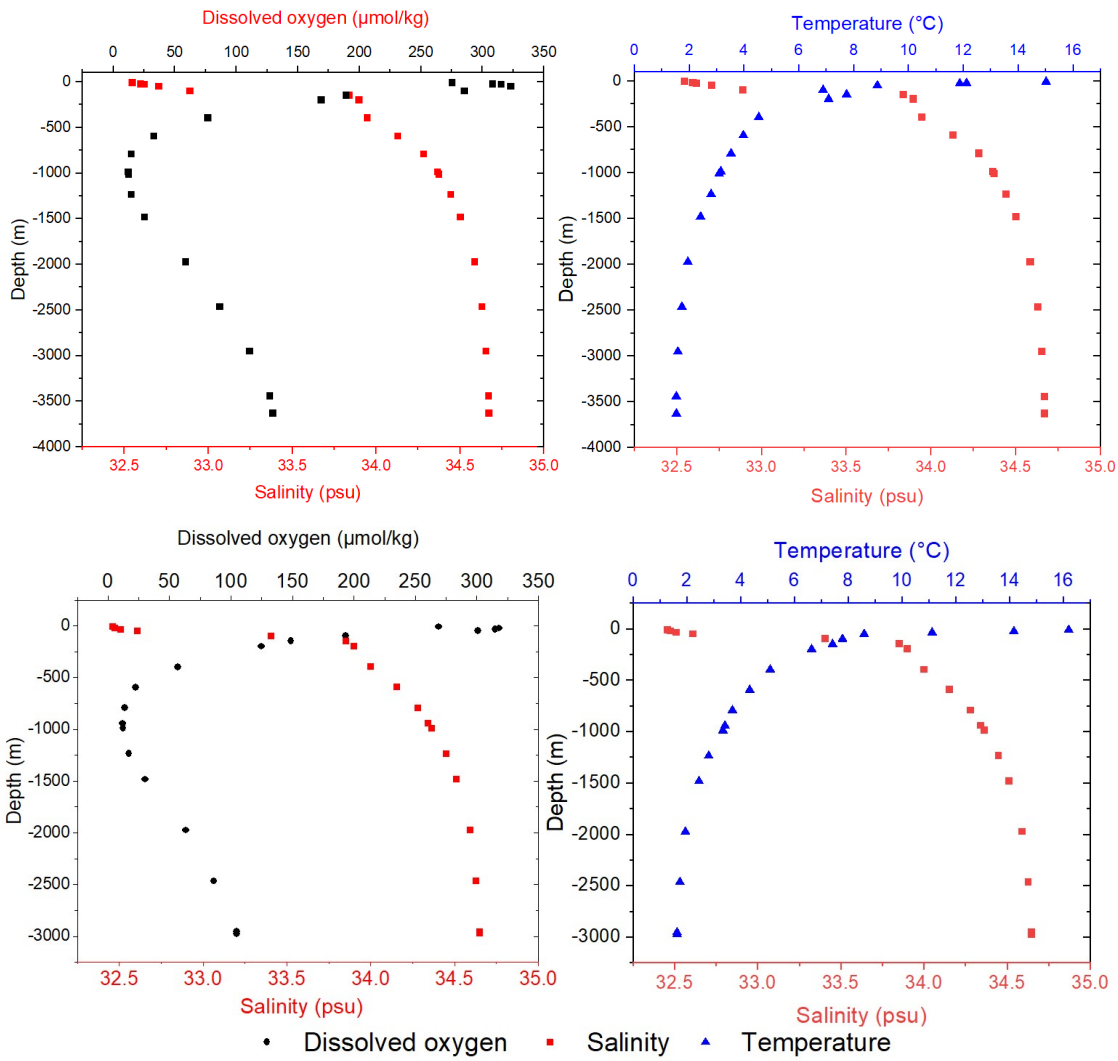

Figure 3.1.2: CL-20 (top) and CL-21 (bottom) depth profiles for salinity and dissolved oxygen (left) as well as salinity and temperature (right). Salinity (red squares) corresponds to the bottom horizontal axis, dissolved oxygen and temperature to the top horizontal axis of the respective diagrams.

The temperature generally falls from 15° C on the surface to below 2° C at 3000 m depth. Between 100 m depth and 400 m depth the temperature of CL-20 increases. Two data points, 149 m and 199 m, show a temperature 1-2°C above that expected for these depths by extrapolating from the remaining data points. The salinity for both appears to be elevated compared to the other depths. This may be an artifact or could indicate the influence or mixing of different water-masses in

this depth range so the assumption of homogeneity is problematic. Outside this depth range the salinity rises with depth, the rate is highly dependent on the depth. During the first 150 m it increases rapidly, then remains almost constant for 200 m and finally asymptotically approaches a constant value below 1600 m. The salinity in the Pacific Ocean is typically lower than in other oceans, as its evaporation-precipitation ratio is almost neutral. The Pacific Deep Water does not originate at the surface but is formed by upwelling of bottom waters like the Lower Circumpolar Deep Water or sinking intermediary waters like the Pacific Intermediary Water (Koshlyakov et al. 2004) and has a higher salinity than the upper waters. (Talley 2011) The overall maximum in dissolved oxygen is around 50 m below the surface, the minimum at 1000 m depth. Below this depth, the dissolved oxygen increases again up to a concentration of $\approx$100 μmol/kg in 3000 m depth, comparable to that at 400 m depth. As dissolved oxygen increases the redox potential in the water and a higher redox potential favors the soluble V+ oxidation state of plutonium (Runde 2000), this increased concentration near the seafloor might facilitate some remobilization from freshly sedimented plutonium IV+ adsorbed to particles. Most of the anthropogenic uranium is expected to be found in the upper 1500m of the water column die to the average residence time of $(3.2 - 5.6) \cdot 10^5$ years in seawater (Dunk et al. 2002) so this increased oxygen concentration is unlikely to have a significant effect on its vertical distribution. The concentration of dissolved oxygen of a water mass can be used as an indicator for the time since it was in contact with the atmosphere (Talley 2011). The Pacific Deep Water has a typical age of 700 to 1000 years based on radiocarbon dating (Gebbie et al. 2012). The increased oxygen concentration indicates the presence of younger water masses near the seafloor, most likely the Lower Circumpolar Deep Water (LCDW) which subducted around the Antarctic Continent. It is richer in oxygen and has a higher salinity than the PDW and is the densest water mass in the Pacific (Talley 2011). Figure 3.1.3 indicates the path of this water mass from there to the eastern North Pacific.

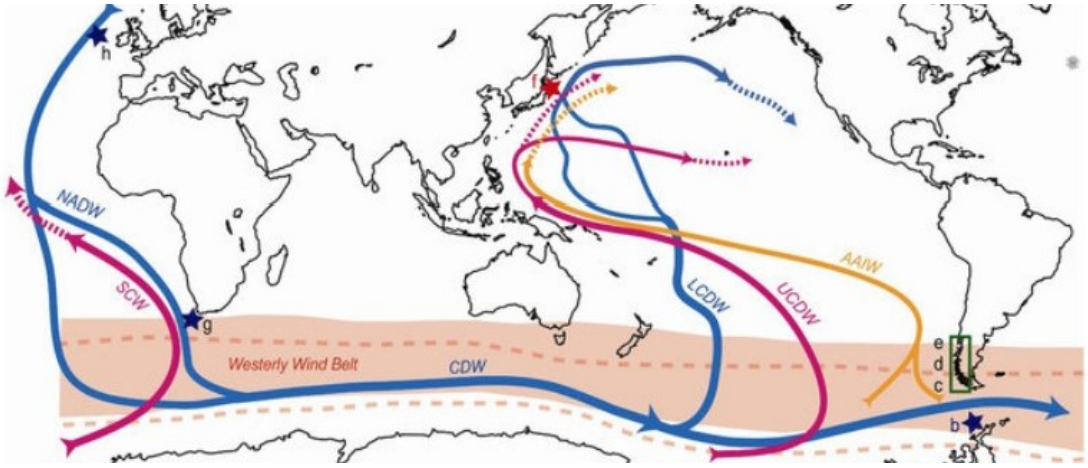

Figure 3.1.3: Deep Water Currents in the Pacific Ocean, with the LCDW (Lower Circumpolar Deep Current flowing from the Antarctic to the eastern North Pacific, typically beneath the much older Pacific Deep Water (PDW). (Rella et al. 2014)

By using the average temperature of 4.8° C and the average salinity of 34.04 ppt the average density of $1026.94 \pm 0.15\,\mathrm{kg/m^3}$ for seawater from the two sampling stations was calculated. This density is used when converting concentrations in at/kg to activities in $\mathrm{mBq/m^3}$.

The ^{238}U content in seawater within the typical salinity range can be approximated by the linear relation $^{238}\mathrm{U} = 0.1 \cdot \mathrm{S}\text{-}0.326$ (Owens et al. 2011) with the salinity S in psu and the ^{238}U concentration in ng/g. Owens states a constant uncertainty of ±0.061 for the fit and ignores the uncertainties of the salinity measurements. This method was applied to the two sampling stations in figure 3.1.4. The calculated concentrations for all depths for both sampling stations are below the concentrations (before normalization to a salinity of 35 ppt) of $3.171 \pm 0.008\,\mathrm{ng/g}$ to $3.296 \pm 0.007\,\mathrm{ng/g}$ measured by Chen in the North Pacific at (31°4´N, 159°1´W) (Chen et al. 1986). An SF-ICP-MS study of the ^{238}U concentration at three stations less than 50 km off the east coast of Japan produced comparable results at $2.961 \pm 0.060\,\mathrm{ng/g}$ to $3.222 \pm 0.051\,\mathrm{ng/g}$ again before normalization to a salinity of 35 ppt (Zheng et al. 2006).

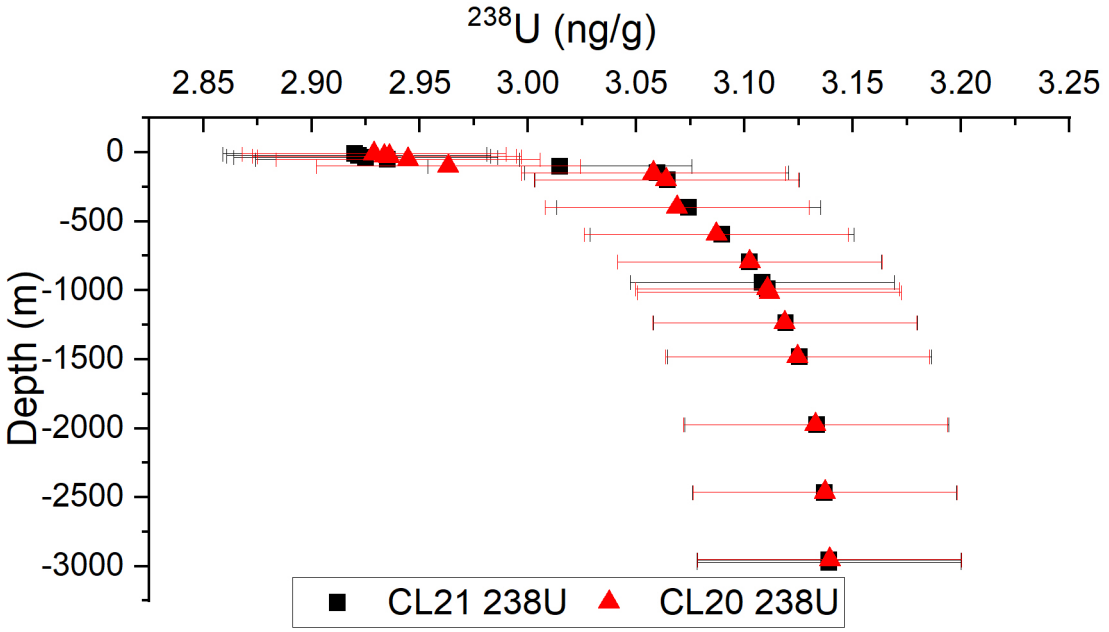

Figure 3.1.4: ^{238}U concentrations at CL-20 and CL-21 calculated from salinity according to (Owens et al. 2011)

3.2 Uranium Standards

The Vienna KkU in-house uranium standard at VERA is produced from a reserve of uranylnitrate separated and bottled sometime before 1919 from uranium ore at the K.K. Uranfabrik Joachimsthal. Due to its age and storage in sealed bottles, no influence from anthropogenic radionuclides is expected. The natural production of ^{236}U mainly from neutron capture on ^{235}U in this material results in a ^{236}U/^{238}U ratio of $(6.98 \pm 0.32) \cdot 10^{-11}$ (Steier et al. 2008). The Vienna-KkU standard can be seen as a machine blank for ^{233}U.

Vienna US-8 is another as of the time of this writing unpublished in-house uranium material with a ^{236}U/^{238}U ratio of $(1.01 \pm 0.03) \cdot 10^{-8}$ based on previous measurements at VERA. In all measurements for this work dilutions of these uranium standards were used. The Vienna-KkU-D30 contains $\approx 100\,\mu g$ U/3 g Fe while the Vienna-US8-D30 contains $\approx 30\,\mu g$ U/3 g Fe based on previous ion current measurements at VERA for these two in-house standards.

3.3 Chemical sample preparation

The central aims of the sample preparation are the production of a few mg of suitable solid target material needed for the AMS measurement, the reduction of interference from neighboring masses and the maximization of the overall detection efficiency. The separation of a plutonium and a uranium fraction both increases the overall detection efficiency on the respective element through an increased share of the measurement time on each target for all isotopes of interest and reduces the possible interference of ^{238}U through tailing or the hydride $^{238}UH^{3+}$ on the ^{239}Pu measurement.

The separation procedure applied using UTEVA and TEVA resins available from Eichrom Technologies is based on the fundamental work of Horwitz (Horwitz et al. 1995) and the procedure (Eichrom 2018) recommended by Eichrom Technologies. The procedure has been adapted by Karin Hain as described in (Hain et al. 2015) for plutonium and based on the results from (Qiao et al. 2015) for uranium. Some variations of the final procedure presented in the following were tested before the processing of the environmental samples, which will be described separately in the following section.

All reagents used were analytical grade for trace analysis in supra/ppb quality from VWR or Carl Roth. Where this was not possible (e.g. in house materials) only materials well established through testing and experience in our laboratory were used. Where laboratory utensils or equipment that have direct contact with the samples were reused, they were cleaned first with deionized water and then placed above boiling 6M HCl within a large, covered beaker on a heat plate for several hours. This procedure removes residues with freshly distilled HCl. While this procedure should remove residues very efficiently single-use utensils are preferable wherever possible when handling environmental actinide samples, as material adsorbed on the surface or implanted in the walls through recoil may remain regardless of the cleaning. In addition to this procedure, utensils that are known to have previously been used on ^{233}U-spiked or other high content samples for any of the isotopes of interest for this work have not been used at all.

All plutonium samples were measured relative to a ^{242}Pu spike which also serves to account for losses during chemical sample preparation. For this purpose the IRMM-085 solution was used (Taylor et al. 2000). The certified amount ratios for the relevant isotopes as stated in the reference certificate (Taylor et al. 2000) are $n(^{239}Pu)/n(^{242}Pu) = 0.0008268(40)$ and $n(^{240}Pu)/n(^{242}Pu) = 0.0001079(40)$. An in-house dilution of this standard produced from the stock solution on 09/08/2016 was the immediate source of the spike material. This concentration was corrected for evaporation with each use and was $(9.069 \pm 0.005) \cdot 10^9$ at/g for the first and $(9.094 \pm 0.005) \cdot 10^9$ at/g for the last environmental samples. An amount corresponding to $\approx 3 \cdot 10^8$ atoms of ^{242}Pu was added to each sample and blank and was determined using a precision scale. Figure 3.3.1 depicts a flowchart for the chemical sample preparation that was used to produce separate uranium and plutonium AMS targets from the ocean water samples. The environmental samples were processed in batches of three samples and one process blank created from 1 l deionized Milli-Q water. The samples were spiked with ^{242}Pu and left overnight to equilibriate and was preconcentrated by evaporation to ≈2.5 liters.

Significant preconcentration was achieved via coprecipitation of the actinides with Fe^{3+}. When raising the pH to 8.5 with NH_3 after adding the iron solution, $Fe(OH)_3$ particles precipitate. Plutonium in the IV+ state is efficiently scavenged at iron concentrations of 1 mg/l, while the V+ state requires more than 12 mg/l for efficient removal from the water (Lovett et al. 1990). A concentration of 15 mg/l was chosen to ensure a maximized plutonium yield irrespective of the oxidation state it is in. For coprecipitaton of uranium, good results have been reported at 10 mg/l Fe^{3+} in (Eigl et al. 2013).

The coprecipitation also serves to remove a large fraction of the salts present in the seawater sample, if the pH level is adjusted with care and not raised to 10 or above when salts present in the ocean water start to precipitate as well. The precipitate was recovered by decanting and centrifugation and washed repeatedly with Milli-Q water adjusted to pH 9 with NH_3. Initially only plutonium isotopes were to be measured, so the in-house pre-nuclear iron solution created from the inside of a railway track from the 19th century was used for both precipitation steps. When the decision was made to measure a separate uranium fraction for all samples,

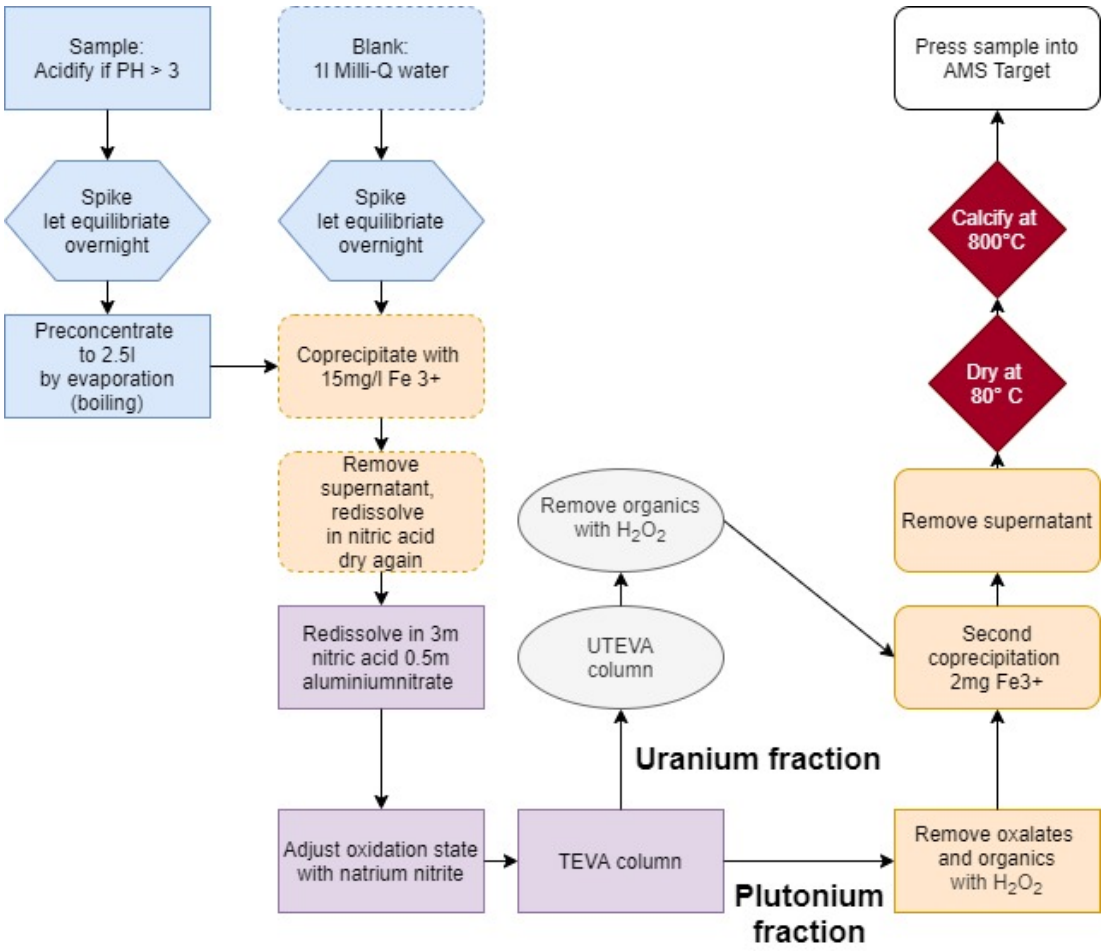

Figure 3.3.1: Flowchart of the chemical sample preparation. The procedure is grouped into the phases by color: preparation (blue), coprecipitation(orange) TEVA (purple) UTEVA (gray), drying and calcination (red) and preparation of the final target (white)

the first coprecipitation step had already been done for samples CL-21 20 m, CL-21 300 m and CL-21 2000 m along with the accompanying blank B2. While this material is free from anthropogenic radionuclides due to its age, it contains natural uranium. For all other environmental samples a chemically purified "Iron AAS Standard Solution" with 1000 mg/l Fe in 2% HNO_3 from Carl Roth was used to avoid diluting the $^{236}U/^{238}U$ ratios in the environmental samples. The $^{233}U/^{236}U$ and $^{239}Pu/^{240}Pu$ ratios of these three samples do not differ significantly from those of samples prepared using the Iron AAS Standard Solution, while the $^{236}U/^{238}U$ ratios fit in with the overall vertical distribution.

The main separation step was achieved by the sequential use of TEVA and UTEVA extraction chromatography resins in the form of columns. TEVA resin uses an aliphatic quaternary amine (Eichrom 2020a), UTEVA uses diamyl, amylphosphonate - DAAP as extractant (Eichrom 2020b). These active components extract specific nitrate or chloride complexes formed by actinides in a suitable load solution and bind them to the resin in the column. The complex formed depends on the oxidation state of the actinide ion and the presence of potential ligands in the solution. The retention for a given actinide complex depends on the resin used, the acidity of the solution, the system (chloride vs nitrate) the column is conditioned to and competing complexing agents. Salts or organic residues can also adversely affect the retention of those actinide complexes on the columns. The presence of competing potential ligands that form strong complexes with actinides can drastically lower the retention on the column. Phosphate and oxalate are of particular significance for tetravalent actinides. Phosphate is present in many environmental samples, so Eichrom recommends the addition of aluminum to each sample in (Eichrom 2018), that will preferentially bind the phosphate. This was done by dissolving the dried sample in 12 ml 3 M HNO_3 - 0.5 M $Al(NO_3)_3$. Sodium nitrite is added to the heated sample under repeated panning to oxidize Pu(III) present to Pu(IV). The uranium is already in the oxidation state VI+ and cannot be oxidized further without much stronger oxidizing agents.

During the AMS measurement hydrides and tailing from ^{232}Th and ^{238}U might interfere with the measurements of ^{233}U and ^{239}Pu, so the two columns should be used in a way that maximizes the overall yield of plutonium and uranium in their respective fractions, while minimizing uranium in the plutonium fraction and thorium in the uranium fraction. The retention of an element or respectively a specific oxidation state by the resin is typically quantified by the k' value (Horwitz et al. 1995) shown in figures 3.3.2 for TEVA (left) and UTEVA (right). Figure 3.3.2 shows that the retention for tetravalent plutonium IV+ in TEVA resin has a clear maximum around 3M HNO_3 while the retention of hexavalent uranium VI+ is four orders of magnitude lower in the same conditions. Thorium IV+ lies between the two. The k' curves for TEVA in the HCl system are too close to each other to allow for a uranium-plutonium separation. Using 3 M HNO_3 as the load

solution for TEVA a high uptake for tetravalent plutonium and a partial uptake for tetravalent thorium can be expected.

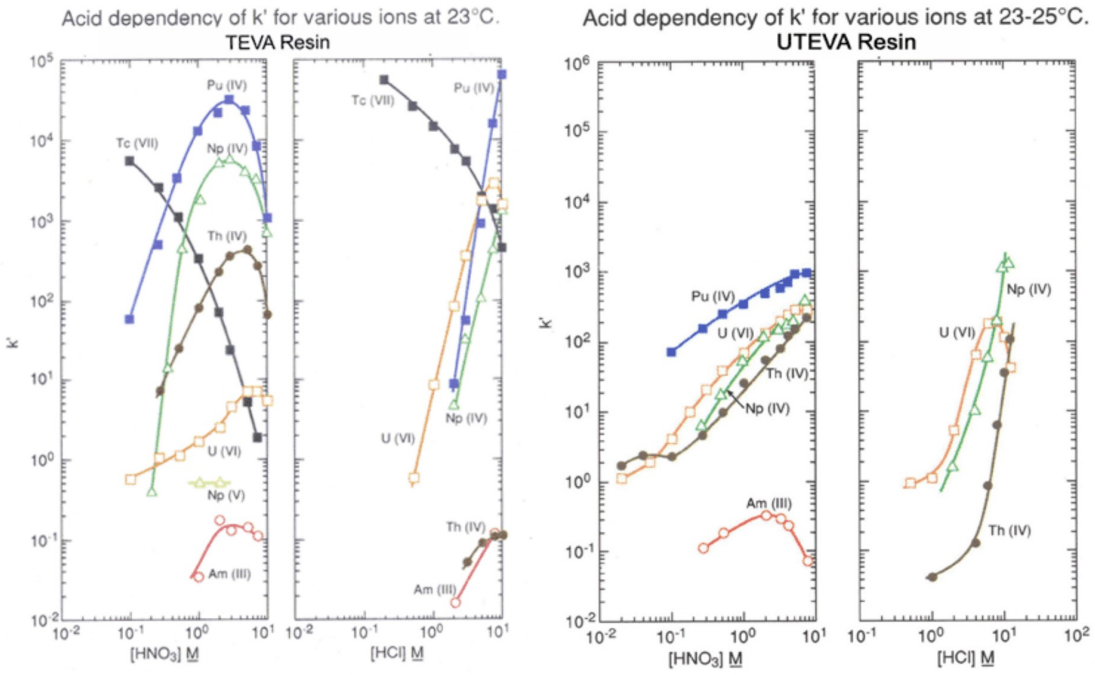

Figure 3.3.2: The k' value for TEVA (left) and UTEVA resin as a function of acidity, both in HNO_3 and HCl. (Horwitz et al. 1995)

The retention of U(VI) is 4-5 orders of magnitude lower than that of Pu(IV) under these conditions, so most of the uranium passes through the column with the load solution and the additional 3M HNO_3 rinse under these conditions. The solution which passes through the column up to this point contains the uranium fraction of the current sample and is set aside.

Oxalates form complexes with tetravalent actinides very readily and can be used for eluting them from the columns. A 2 M HNO_3 − 0.1 M oxalic acid is used to strip the tetravalent plutonium from the column. While most of the uranium will have passed through the column in the previous step, figure 3.2.2 still shows a small uranium retention for 3M HNO_3. This small fraction of U(VI) retained on the column is unaffected by the oxalate stripping solution resulting in a second uranium separation from the plutonium fraction. ^{238}U and ^{234}U measurements on

the uranium and plutonium targets from three samples (CL-21 20 m, 300 m and 2000 m) during the heavy/aug2019c beamtime showed, that the plutonium targets only contained $2.2‰ - 5.8‰$ of the ^{238}U content determined for the corresponding uranium targets.

When evaporated to dryness the oxalates in the plutonium fraction form white crystals growing on the walls of the crystallizing dishes holding the plutonium fraction at this stage as can be seen in figure 3.3.3 on the left. Dissolving the sample in 6 M HNO_3 and heating it to 170°C in a crystallizing dish closed with a watch-glass for up to two hours leads to an efficient decomposition of the oxalates. Organic compounds that might have been introduced by the resin are removed by repeated fuming with HNO_3 conc. and H_2O_2.

Figure 3.3.3: Dried plutonium fraction after TEVA prior (left) and after (right) the removal of the oxalates from TEVA elution

The retention of hexavalent uranium in 3M HNO_3 on a UTEVA column is two orders of magnitude higher than on the TEVA column, as shown in figure 3.3.2. The retention of tetravalent thorium is very similar in the nitrate system. Washing the loaded column with 8M HCl still retains most of the uranium VI+, while thorium is reduced by up to two orders of magnitude. The uranium can then be eluted with 0.025M HCl. Organic residues are again removed by with H_2O_2 as described for the plutonium fraction.

A second coprecipitation with Fe^{3+} to $Fe(OH)_3$ using the Iron AAS Standard Solution followed by drying at 80° overnight and calcification at $800°C$ for four hours yields the final AMS target material, a few milligrams of the Fe_2O_3 matrix

containing the uranium and plutonium trace isotopes as oxides. This material can then be pressed into the aluminum target holders or cathodes for the AMS measurement.

Tested Changes to the chemistry procedure

The use of oxalates requires a time-consuming decomposition step. In addition to this the growth of the oxalate mass from the sample during evaporation might adversely affect the chemical yield as in some cases the material was visibly growing towards the lip of the dish and crystals formed on the watch-glass. In the German product sheet for TEVA resin, (Triskem International 2015) Triskem international alternatively recommends the use of rongalite ($Na^{+}HOCH_2SO_2^{-}$) to reduce the tetravalent plutonium on the column to the III+ oxidation state and rinse it with 4M HNO_3. To evaluate this approach three test samples based on Milli-Q water were spiked with ^{242}Pu (IRMM-085 solution) for the first beamtime heavy/may2019a. Two test samples were prepared following the full plutonium fraction procedure detailed above for chemistry blanks, with "test 1" using oxalate and "test 2" rongalite for eluting the plutonium from the column. For the third sample "std a" which serves as an external standard, the spike was directly coprecipitated with Fe^{3+} and prepared following the remainder of the procedure after the second coprecipitation.

In a typical actinide measurement at VERA the countrates rise over time due to the characteristics of the ion source used. In a measurement with environmental samples one or more trace isotopes are measured alongside a reference isotope and normalized to it, so that all these external factors influencing the countrates can be compensated for. The ^{242}Pu spike would be that reference isotope in an environmental sample measurement and for the chemistry tests the only the raw ^{242}Pu countrate was available, so a rough estimation of these factors is required. The ^{239}Pu countrates on the environmental samples in later beamtimes typically changed by a factor of 2-4 over the duration of the beamtime of one week, with individual outliers up to a factor of 10. The main contribution to this will be an increased output from the ion source over time. This is a slow process compared

to the individual measurements. The measurement procedure with several shorter measurements on all targets spread over the whole beamtime instead of one long measurement each should ensure, that all three targets are affected in a similar way by this and other slow changing machine parameters. The statistical uncertainty based on the sum of all counts may underestimate the real uncertainty. The external uncertainty based on the standard deviation of all individual measurements would be heavily influenced by the drift in parameters just discussed, without taking the effect of the more or less even spreading of the short measurements over the range of this drift into account. Due to these considerations a factor of two or more between the countrates was initially considered the threshold for a significant result.

For each of the test samples and the standard the average countrate and the number of ^{242}Pu atoms spiked are recorded in table 3.3.1 The countrates of the test samples were normalized to the amount of ^{242}Pu spike used for std a to allow direct comparison of the count rates even though the differences in the amount of ^{242}Pu added is very small. For the average countrates the statistical uncertainty was used, while the uncertainty of the spike amount is based on the reproducibility of measurements with the precision scale used repeatedly during the spiking of each sample. The rongalite result is almost three orders of magnitude lower than the oxalic acid sample. During the sample preparation the TEVA column had a very slow flow-rate with the whole process from preconditioning to elution taking more than four hours, and large bubbles documented in figure 3.1.4 were formed. Small bubbles formed early on in both samples but increased drastically in number and size during the elution in the rongalite sample. One sample from (Hain 2016) showed a similar behavior with bubble formation and a very low chemical yield.

To check the reproducibility of the low chemical recovery when using rongalite, a second chemical test for the comparison of rongalite and oxalic acid as elutants was prepared for the heavy/jun2019c beamtime. The sample “test 4” used rongalite, and “test 5” oxalic acid while “std a” and “std b” were prepared by direct coprecipitation. Table 3.3.2 contains the results from this measurement.

Sample	n(^{242}Pu) (10^8 at)	Avg. countrate (cps)	Norm. countrate (cps)
test 1	2.710±0.050	8.582±0.077	9.63±0.20
test 2	2.913±0.050	0.0101±0.0033	0.0105±0.0035
std a	3.041±0.050	22.19±0.12	22.19±0.12

Table 3.3.1: Numbers of ^{242}Pu atoms spiked, corresponding average count rates and average countrates normalized to the amount of spike used for std a for the first chemistry test in beamtime heavy/may2019a. The sample test 2 prepared with rongalite as elutant has a countrate almost three orders of magnitude below the oxalic acid sample test 1.

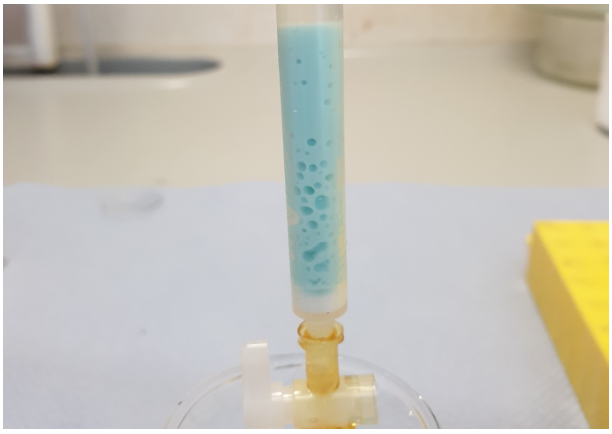

Figure 3.3.4: TEVA column of test 2 after the elution with rongalite. The formation of these large bubbles correlates with a drastically lowered ($\approx 10^{-3}$) chemistry yield based on one sample in (Hain 2016) and two chemistry tests in this study.

Sample	n(^{242}Pu) (10^8 at)	Avg. countrate (cps)	Norm. countrate (cps)
test 4	2.794±0.050	0.0483±0.0057	0.0602±0.0071
test 5	3.570±0.050	16.406±0.057	16.020±0.056
std b	4.526±0.050	39.155±0.089	30.158±0.069
std c	3.486±0.050	30.473±0.076	30.473±0.076

Table 3.3.2: Number of ^{242}Pu atoms spiked and corresponding average count rates for two more chemistry tests with rongalite (test 4) and oxalic acid (test 5) as elutants and the two standards std b and std c in the heavy/jun2019c beamtime. The countrates were normalized to the amount of spike used in std c.

The results of std b and std c show, that the initial threshold of a factor 2 for a significant result in the chemistry test was overly cautious and the distribution of shorter measurements over the duration of the beamtime is very effective at compensating for the influence of changing machine parameters on the average countrates. The rongalite sample test 4 is again three orders of magnitude below the oxalic acid sample test 5. Even though great care was taken to follow the procedure with both samples, similar bubbles formed in test 4 and the average countrate was again several orders of magnitude below that of test 5. Due to the second negative result the plan of using rongalite for the environmental samples was abandoned. While bubbles appeared in some of the samples processed later and eluted with oxalic acid, they were much smaller, formed slower and did not have such a drastic impact on the yield.

3.4 Observations and problems during chemical sample preparation

There were persistent problems with the process blanks in several batches during $Fe(OH)_3$ co-precipitation. The size of the individual flakes of the $Fe(OH)_3$ precipitate were consistently smaller than those formed in the seawater samples which complicated decanting of the solution. During the washing steps the precipitate from the blanks repeatedly dissolved partially. This was dealt with by complete re-dissolution with HNO_3 and repeated fresh precipitation through the addition of NH_3 so that the preparation of some blanks was very time-consuming. The obvious explanation is that the salinity of the seawater influences the conditions of the precipitation. No solution was found for this problem, as the addition of salts might introduce a new source of contamination and reduce the representativity of the blanks. Shaking the samples by hand instead of using a vortex mixer and a pipet to loosen up the precipitate compacted by the centrifuge for washing in combination with raising the pH during precipitation slightly higher than for the seawater samples reduced the problem to a manageable extent. The higher pH of ≈ 10 instead of ≈ 9 should be the least problematic approach, as these samples do not contain a relevant salt matrix that needs to be separated from the

actinides. The forced repetition of this co-precipitation step for some blanks leads to an increased amount of NH_3 and HNO_3 in them. However, no clear relation between the severity of this problem during the chemical procedure and elevated blank levels was found. During initial attempts to deal with this problem precipitate that was almost black instead of the usual rust color formed in blank B1 from the first environmental samples batch, indicating the reduction of Fe^{3+} to Fe^{2+} at some point. Due to the early stage of the batch the blank was discarded and a new blank was prepared.

Some of the TEVA columns were much slower than average, which was most probably caused by the presence of undissolvable white crystals in the column load solution which accumulated on the resin and drastically reduced the flow rate through the column. These crystals formed only when re-dissolving the $Fe(OH)_3$ residue in 3M HNO3 3 M HNO_3 - 0.5 M $Al(NO_3)_3$ after evaporation to dryness. Removing these crystals by centrifugation eliminated the problem of columns with very slow flow. In a PIXE measurement of these crystals at VERA by Christoph Eisenhut iron, aluminum, silicon and calcium were identified. While aluminum and iron can be explained by the prior addition of these elements to the samples, silicon and calcium are common in seawater. The impact of these crystals on the chemical yield can not be quantified, as the fraction of the actinides incorporated into the crystals is unknown. The problem might be larger for plutonium than for uranium, as it is the more particle reactive element and might adsorb to the crystals much more readily. However, for both elements the losses would affect the reference isotope as well as the trace isotopes, and the ratios would remain unaffected. There is no obvious correlation between the ^{242}Pu countrates and the occurrence of these crystals, so while this may have adversely affected the chemical yield for some samples, other factors played a larger role in this respect. The targets with the lowest ^{242}Pu countrates were blanks, where this problem did not occur.

4 Detection of actinides at VERA

4.1 The AMS setup for actinide measurements

Accelerator mass spectrometry is an extension of conventional mass spectrometry with the use of tandem particle accelerators for the suppression of molecular isobars. It is the most sensitive method available for the detection of a wide range of long-lived trace isotopes. A.E. Litherland defined the basic ideas of AMS as the discrimination between atomic species in the ion source, the destruction of molecular isobars and the identification of the individual ions (Litherland et al. 1981). In some important cases the discrimination between atomic species can already be achieved in the ionization process. The showcase application of AMS, ^{14}C benefits by the convenient fact that its abundant atomic isobar ^{14}N does not form stable negative ions (Litherland et al. 1981). There are almost no stable molecular ions with a charge of 3+ or higher, so to achieve the suppression of molecular isobars a tandem accelerator with foil or gas stripper is typically used. Triply charged hydrides of uranium and thorium are stable enough to reach the detector and need to be suppressed for measurements of ^{233}U, ^{236}U or ^{239}Pu (Lachner et al. 2012) which is typically achieved by adjusting the stripper gas pressure. This will be discussed in detail in 4.6. Detectors developed for nuclear or particle physics can be utilized to identify the individual ions selected by various filtering mechanisms. With these ideas and the principles of mass spectrometry in mind, the essential AMS setup is already outlined as two mass spectrometers called injector (low energy side) and analyzer (high energy side) connected by a tandem accelerator. This basic setup can then be extended by various components to solve specific problems and make new isotopes accessible.

The Vienna Environmental Research Accelerator (VERA) has been in use since 1996 (Kutschera et al. 1997). While the radiocarbon dating was and remains an important application, VERA has always been intended to be a universal AMS facility. Several upgrades like a TOF system (Steier 2000), a high-resolution electrostatic analyzer on the high energy side (Steier et al. 2004), the addition of a second high energy analyzing magnet (Steier et al. 2019) and the development of the ILIAMS RFQ ion beam cooler (Martschini et al. 2019) along with constant ongoing improvements and developments have vastly extended the range of isotopes that can be measured at VERA over the past two decades.

Figure 4.1.1 illustrates the current setup of the facility for actinide measurements. Only the components used for this setup are labeled in the figure. In the following subsections the main components or this setup are discussed based on (Steier 2000) where not noted otherwise.

4.1.1 Ion source

The S1 beamline at VERA has a Middleton type SNICS (Source of Negative Ions by Cesium Sputtering) ion source by NEC. In this type of ion source cesium is evaporated, thermally ionized and these positive primary ions are accelerated with a few kV towards the cathode holding the sample material (Middleton 1983). Up to 40 samples can be placed on a wheel inside the source The wheel can be turned using a software-controlled electric motor to access each sample during the measurements.

The interaction with the target material is quite complex and several effects are known or claimed to contribute to the formation of the beam of secondary negative ions. In the original description by Middleton the primary Cs ions sputter the material, kicking out atoms, molecules or even clusters from the sample material. As a layer of cesium covers the surface of the target, its work function is lowered. The cesium atoms implanted in the target by this process also act as electron donors for the sputtered particles leaving the sample (Middleton 1983).

The energy deposited by the impacts heats a small (nanometer range) area to temperatures of several thousand Kelvin resulting in the formation of plasma (Kieser

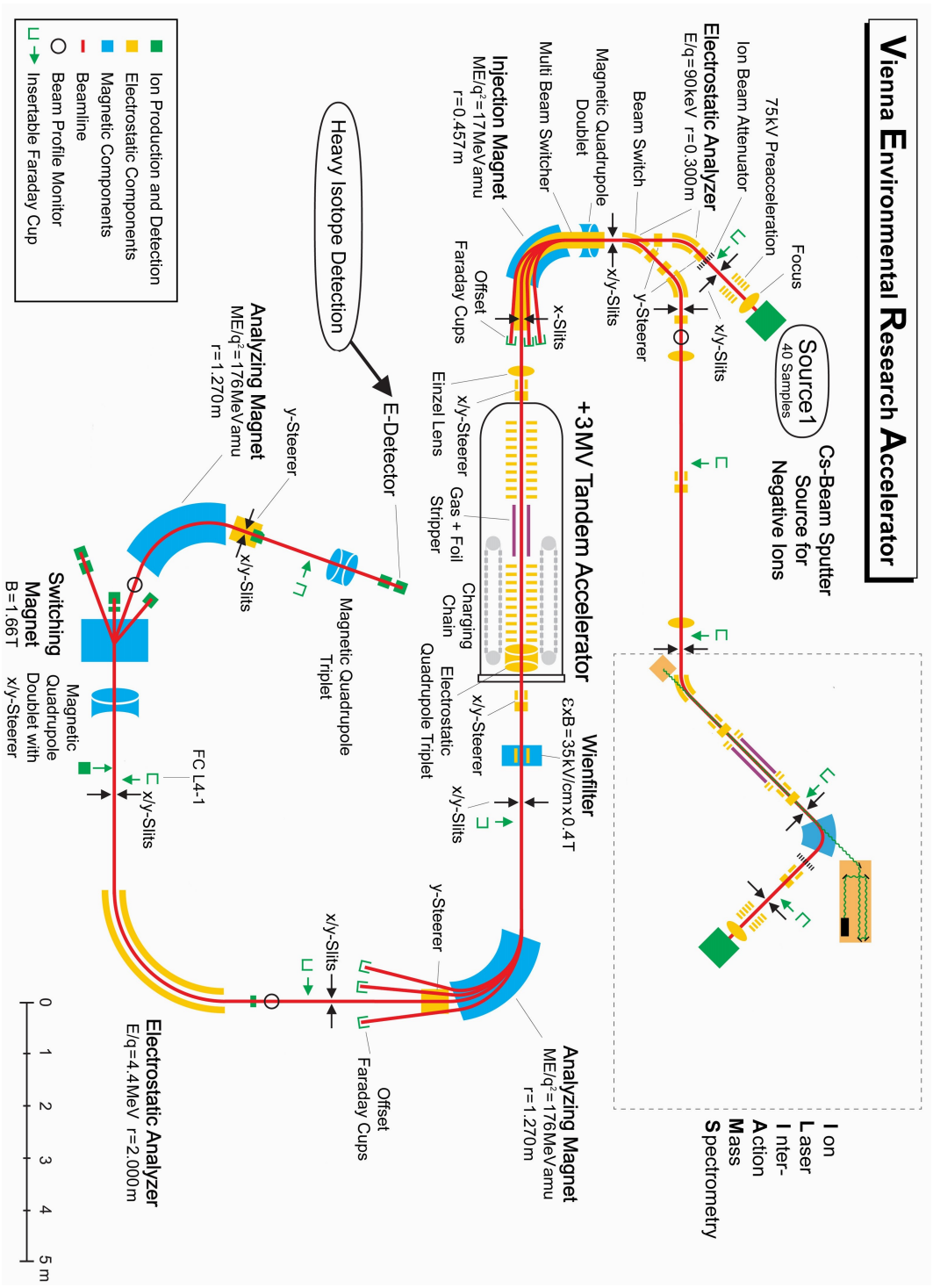

Figure 4.1.1: An overview of the current VERA setup used for actinide detection from the ion source 1 to the heavy isotope detector. The components are color-coded by type as explained in the box on the lower-left corner.

et al. 2012). The utilization of the chemical reactions facilitated by these conditions in the presence of a suitable matrix for increased ionization efficiency or reduced measuring time is the subject of ongoing development at VERA. In 1999 Middleton reported a correlation between the formation of plasma balls in recesses formed during sputtering and increased outputs of negative ions (Middleton et al. 1999). In 2016 John S. Vogel claimed to have observed that excited states of (neutral) cesium are formed in this plasma, and resonant electron transfer with neutral sputtered material contributes significantly to the secondary negative ion yield in addition to the surface ionization model (Vogel 2016). This second effect would be especially relevant if the target is recessed or a pronounced crater has been formed in the course of the sputtering process but is still subject of some debate. The yield of atomic actinide ions is far too low for practical purposes, so molecular negative ions containing the actinides like UO^- and PuO^- are used instead. The typical negative ion extraction efficiency for these oxides is $\approx 0.3\%$ (Fifield et al. 1996).

4.1.2 Electrostatic and magnetic analyzers

The trajectory of a particle in an electric field depends on its energy to charge ratio, and in a magnetic field on the momentum over charge ratio. Electrostatic and magnetic filters are applied to the ion beam leaving the source. Three types of these filters are used at VERA. Electrostatic analyzers, bending magnets and a Wien filter. Each field is adjusted so that ions with the nominal ratios can continue their path through the beamline, while those deviating from the nominal ratios are either directed into offset Faraday cups to be measured as a current, or they are stopped by collisions with slits in the outgoing beamline or the walls of the beamline.

Electrostatic analyzers consist of either cylindrical or spherical electrodes mounted at a distance d from each other with the beamline passing in between. The VERA setup uses an electrostatic analyzer with E/q up to 90 keV and radius $r = 0.3\,m$ on the low energy side, and one with E/q up to 4.4 MeV and $r = 2.0m$ on the high energy side.

The present configuration of VERA utilizes three 90° dipole magnets as described in (Steier et al. 2019) for the detection of actinides. The injection magnet on the low energy side has a ME/q^2 of up to 17MeV amu and a radius of r_0=0.457 m. The two analyzing magnets on the high energy side have a radius of $r_0 = 1.27$ m and a maximum ME/q^2 of 176MeV amu. The first is placed after the accelerator while the second is right before the detector, a Bragg-type ionization chamber. A switching magnet is used for directing the beam into the correct beamline.

A Wien Filter combines electrostatic deflector plates and a bending magnet in such a way, that the electrical and magnetic fields created are perpendicular to each other and the incoming ion beam. The force acting on a charged particle in a magnetic field depends on the velocity of that particle, while that in an electric field does not. This enables the use of the Wien filter as a velocity filter. For particles with the nominal velocity the fields cancel out, while those with a deviating velocity are deflected and cannot pass the Wien filter.

4.1.3 Accelerator and stripper

A pelletron tandem accelerator is an electrostatic accelerator using chains with insulated links for the mechanical transport of electrical charge to the terminal. VERA uses a 3MV pelletron with gas stripping. Incoming negative ions from the injector are accelerated to the positive high voltage applied to the central terminal of the accelerator, where interactions with the stripper gas result in the loss of electrons. This is a stochastic process, resulting in a distribution for the various possible charge states of the stripped ions. The choice of the stripper gas and its pressure as well as the velocity of the ions determined by the terminal voltage influence the mean of this charge state distribution. Based on the results from (Vockenhuber et al. 2011) and (Winkler et al. 2015) helium stripping and the charge state 3+ are used for actinide measurements at VERA. Most molecular ions with charge 3+ and above are unstable and consequently broken up through the stripping process, removing molecular isobars. However, in (Lachner et al. 2012) it was shown, that a fraction of triply charged hydrides of actinides may still reach the detector. An increased stripper gas pressure of ≈ 1 Pa instead of

the optimum for the yield at ≈ 0.4 Pa and where applicable chemical separation is used to suppress these hydrides. The yield for the 3+ charge state at this pressure and $\approx$ 1.65MeV terminal voltage is $\approx$ 19% (Steier et al. 2019). This problem is discussed in more detail and with respect to the measurements for this thesis in section 4.6. After the stripping, the now positively charged ions are subject to a second acceleration away from the positive high voltage.

Interactions of unwanted ions with residual gas molecules or molecular fragments from the stripping process contribute to the background in AMS measurements. Increasing the ion energy reduces the interaction cross-sections (Winkler et al. 2015) and therefore the contribution of these effects to the background. The mass-energy product of the analyzing magnets on the high energy side of 176 MeV amu limits the terminal voltage to ≈ 1.7 MV for actinides. This is achieved by shorting 3/9 sections of the terminal with an insertable rod, resulting in a terminal voltage of ≈ 1.65 MV with the exact value depending on the mass to be analyzed.

4.1.4 Ion optics

Electric lenses and magnetic quadrupole doublets are used to focus the beam, steerers for small deflections of the beam. These are placed at various points along the beamline to balance out focusing and bulging caused by the various fields acting on the ion beam as well as general dispersion due to charge or collisions. The slits placed after the electrostatic and magnetic analyzers remove particles that received a small spatial displacement due to deviating energy over charge or momentum over charge ratios in the previous analyzer. Slits are ideally placed where the previous filter focuses the nominal beam. By reducing the diameter of the opening, the resolution of the previous filter can be increased. When the diameter of the opening is smaller than that of the nominal beam the slits act as collimator and consequently the ion optical transmission is reduced.

4.1.5 Detectors

Faraday cups are used for the current measurements of ^{238}U. The offset cup after the injector magnet is used for the low energy current measurements and the cup FC L4-1 for those on the high energy side. The trace isotopes ^{233}U, ^{236}U, ^{239}Pu and ^{240}Pu are detected at a Bragg type ionization chamber of 30 cm length located after the last analyzing magnet and operated with isobutane. This detector registers individual ions as events.

4.1.6 Beam sequencing

For measuring reference and various trace ions, the settings of VERA are changed to allow different ions of interest to pass through the setup. There are two sequencing modes, slow or fast. For the plutonium targets, slow sequencing is performed by switching the electrical components so that each plutonium isotope can be measured in turn with a switching time of ≈ 5 s. For the uranium targets the fast sequencing system allows for the determination of the $(({}^{238}U^{3+}/3)/{}^{238}UO^{-})$ ratio once every second during the measurement of the trace isotopes ^{233}U and ^{236}U (Steier et al. 2019). This ratio that combines the charge state yield and the ion optical transmission is used along with the detection efficiency and other parameters to monitor the quality of the measurement.

4.2 Measurement procedure for actinides at VERA

Whilst the actinide measurements themselves once running benefit from fairly sophisticated automation, some steps for adjusting the basic setup of VERA to the needs of the planned measurement like the insertion of the shorting rods or ensuring the required detectors and cups are connected to the corresponding signal processing electronics need to be done manually. The setup from a previous actinide measurement is used as a starting point for the beam tuning. Should this fail to produce a ^{238}U countrate from an old carbon target, the main components are adjusted one by one, maximizing the ^{238}U current in a Faraday cup along the

beamline until a countrate is registered. From this point on, the AUTOMAX, a robust multi-dimensional tuning algorithm can take over to optimize the tuning over the course of several hours (Steier 2000).

For all uranium samples, mass ^{238}U is measured as a current in the Faraday cup FC L4-1 right before the switching magnet, while the masses 233, 236 and 239 are measured as events in the detector. The ^{236}U rare events are normalized to the ^{238}U beam current. A possible source of background on mass 236 are $^{235}UH^{3+}$ molecules which survive the stripping process and are sufficiently stable to reach the detector. Therefore, the mass 239 count rate is measured for the Vienna-KkU as a proxy to monitor the presence of these UH molecules in the detection system. On mass 233 a similar hydride background from ^{232}ThH is possible. While the sample preparation should suppress thorium in the samples by several orders of magnitude, ^{232}Th is still present in all samples at trace level and measured on all uranium targets.

The uranium concentration in the chemical blanks is too low to allow for a reliable measurement of ^{238}U currents in the Faraday cup FC L4-1, so ^{234}U events are also measured at the detector for the uranium blanks. From this countrate and the ratio of these two natural uranium isotopes usually in radiative equilibrium the ^{238}U current can be interpolated. The $^{234}U/^{238}U$ equilibrium ratio can be calculated from their half-lifes of $2.455 \cdot 10^5$ years and $4.468 \cdot 10^9$ years (IAEA 2020) as $0.5495 \cdot 10^{-5}$.

On all plutonium targets ^{239}Pu, ^{240}Pu and ^{242}Pu were measured as events. In addition to this, ^{238}U currents and ^{234}U events were measured on some of the plutonium targets to estimate the ^{238}UH background on mass 239 using the Vienna-KkU proxy. Worst case estimates for background due to hydrides in this study can be found in chapter 4.6.

One measurement of all the specified current and event isotopes is called a sequence. Several sequences make up a run on a target, after which the next target is measured for a run. When all samples have been measured, a turn is completed. The order in which the targets are measured for one turn is quasi-randomized, with two standards as the first two targets. The purpose of this randomization is to avoid situations where several targets with high currents are measured back

to back. The automatic regulation of the ion source might respond to several targets with high currents in a row by decreasing the output of the source which might lengthen the time necessary to achieve a sufficient counting statistic on other targets with low countrates in the same measurement.

The ^{236}U events of the in-house standard material US-8 are used to set regions of interest in a peak width vs peak height 2d spectrum, as shown in figure 4.2.1 for one of the samples analyzed with respect to plutonium for this thesis. The position in this plot allows for the discrimination between the (electronic) pulser signal (a), actual events in the chosen 3+ state (b), pile-up (c), lower charge states/multiple scatter events (d) and unexplained events visible in some but not all measurements, often coinciding with increased spark activity in the ion source (e). Only counts in the set trace isotope (b) and pulser (a) regions of interest are registered for the automated generation of the results file. Several potential problems like significant dead time losses due to very high countrates can be identified in these spectra and may require the use of attenuators or the setting of adapted regions of interest in each turn.

The durations chosen for the different masses represent a compromise between the expected countrates and practical considerations concerning the available time on the accelerator, the finite time each cathode can be sputtered before being empty and the stability of some machine parameters during a single long sequence. The length of each sequence is defined by the number of cycles, with each cycle having a duration of 95000μs for ^{232}Th and ^{234}U and 20 of these cycles per sequence. The cycle duration was set at 995000μs for all remaining event isotopes. 120 cycles per sequence were set for ^{236}U while 700 cycles were set for ^{233}U, 150 cycles for ^{239}Pu, 250 cycles for ^{240}Pu and 90 cycles for ^{242}Pu.

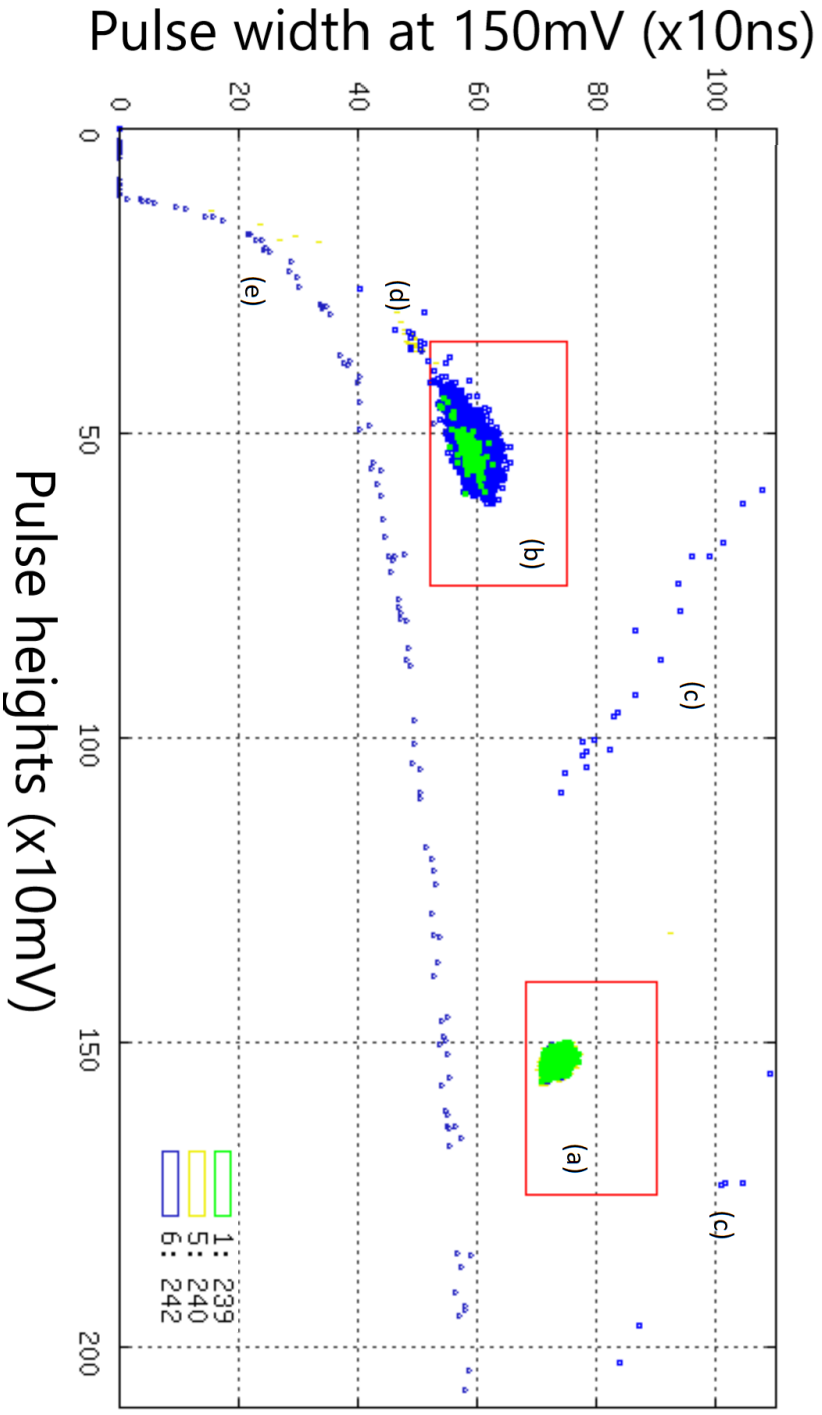

Figure 4.2.1: Pulse height versus peak width plot of a plutonium sample with the regions of interest for the electronic pulser (a) and trace isotope bin (b) in the red rectangles, pile-up (c) lower charge state/multiple scatter events (d) and a sporadic, not yet explained events (e)

4.3 Calculation of isotopic ratios and associated uncertainties

The total content or concentration of ^{239}Pu and ^{240}Pu in any sample can be calculated by normalization of the events to the internal ^{242}Pu spike. The usual ^{233}U spike used for the calculation of absolute ^{236}U concentrations could not be used, because the environmental ^{233}U from these samples was also measured. Instead the ratios ^{236}U/^{238}U and ^{233}U/^{236}U were determined. As ^{238}U is measured as a current with negligible statistical error the calculations for ^{236}U/^{238}U differ from those for the other ratios and nuclides and will be described first. For all four isotopes of interest the desired ratios are calculated in two ways. The turn-by-turn evaluation followed by weighted averaging is preferred whenever possible, as fluctuations in the measurement setup are compensated very accurately on a turn-by-turn basis. This also allows for a comparison of internal and external uncertainties. For targets with an average of less than 10 counts per run all runs are instead combined and evaluated together. As this combined evaluation is equivalent to a single long run over the total duration of all k runs on a given target, only the internal uncertainty of the measured values and their propagation can be taken into account.

When not stated otherwise, the 1σ uncertainties rounded to two significant digits are given for all data from this work. This also applies to the error bars in all plots.

4.3.1 Determining the ^{236}U/^{238}U and ^{233}U/^{236}U ratios

In the following the calculations for the ^{236}U/^{238}U ratios are presented. The calculations for the ^{233}U/^{238}U ratios are analogous and will be used to arrive at the ^{233}U/^{236}U ratios in a final step. For the turn-by-turn evaluation of ^{236}U the counts in the pulser bin p, the 236 counts in the X+ bin x, the average ^{238}U current I and the nominal pulser rate p_{rate} set to 68.75 cps are known. The detection efficiency de is calculated by dividing the well-established ^{236}U/^{238}U ratios for the Vienna-US8 standards by the ^{236}U/^{238}U ratio measured on this material in a given turn and averaging over all Vienna-US8 targets. For a given run i dividing the counts p

in the pulser bin by the pulser rate p_{rate} results in the measured time t_{236} on mass 236. Large discrepancies between t_{236} and the set duration of the measurement can be caused by frequent sparks in the ion source resulting in the discarding of the affected cycles by the data acquisition program due to the unstable currents or significant dead time losses due to high countrates for example on ^{234}U.

The charge that would have been accumulated by the average ^{238}U current I over the measurement time t_{236} is given by $Q_{238} = I \cdot t_{236}$. The count rate r_{236} is calculated by dividing the X+ 236 counts by t_{236} as $r^{236}\mathrm{U} = x/t_{236}$. The ratio can then be calculated as

$$^{236}\mathrm{U}/^{238}\mathrm{U} = \frac{x}{\left(\frac{Q_{238}}{3 \cdot e}\right)} \tag{4.3.1}$$

with the elementary charge $e = 1.602177 \cdot 10^{-19}$C. As the uncertainties of the duration, the current measurement and the elementary charge e are again neglected, the uncertainty of the x counts in the X+ bin , $\sqrt{x}$ is simply scaled by the factor $1/\frac{Q_{238}}{3 \cdot e}$. The normalized ratio r is calculated from this $^{236}\mathrm{U}/^{238}\mathrm{U}$ ratio by dividing it by the detection efficiency de. The uncertainty is scaled by the same factor: $\Delta r = \Delta^{236}\mathrm{U}/^{238}\mathrm{U} \cdot \frac{1}{de}$. At this point it becomes necessary to combine the results for all k runs on a given sample analyzed individually so far. From here on a_i will refer to the quantity a in run i. The weights for the weighted averages are the squared inverses of this uncertainty Δr. The turn-by-turn average ratio $^{236}\mathrm{U}/^{238}\mathrm{U}_{\ turnw}$ of all k runs on a given target can now be calculated as

$$^{236}\mathrm{U}/^{238}\mathrm{U}_{\ turnw} = \frac{\sum_{i=1}^{k}\left(\frac{1}{\left(\Delta^{236}\mathrm{U}/^{238}\mathrm{U}\right)_i}\right)^2 \cdot \left(^{236}\mathrm{U}/^{238}\mathrm{U}\right)_i}{\sum_{i=1}^{k}\left(\frac{1}{\left(\Delta^{236}\mathrm{U}/^{238}\mathrm{U}\right)_i}\right)^2} \tag{4.3.2}$$

The internal uncertainty for $\Delta^{236}_{int}\mathrm{U}/^{238}\mathrm{U}_{\ turnw}$ is calculated by Gaussian error propagation for this weighted mean, while the external uncertainty is calculated as the empirical standard deviation over all k runs. The final uncertainty $\Delta^{236}\mathrm{U}/^{238}\mathrm{U}_{\ turnw}$ is then defined as the larger of those two.

For the combined evaluation, the durations and counts in the X+ and pulser bins of all runs are each simply summed up. The calculations are then identical to those for a single run for the turn-by-turn evaluation.

When both ^{236}U/^{238}U and ^{233}U/^{238}U have been determined according to the procedure detailed above, the ^{233}U/^{236}U ratio can be calculated as

$$^{233}U/^{236}U = \frac{^{233}U/^{238}U}{^{236}\mathrm{U}/^{238}\mathrm{U}} \tag{4.3.3}$$

with the uncertainties calculated by Gaussian error propagation for multiplicatively linked quantities.

4.3.2 Normalization of ^{239}Pu and ^{240}Pu

In contrast to ^{236}U and ^{233}U, the two plutonium isotopes of interest for this thesis are measured relative to other event isotopes. In this subsection the necessary calculations are demonstrated using the example of ^{239}Pu and the ^{242}Pu spike. ^{240}Pu is then calculated from ^{239}Pu to avoid correlated uncertainties in the calculation of the ^{240}Pu/^{239}Pu ratio. For ^{233}U/^{236}U this approach was unnecessary, as the uncertainty of the ^{238}U current where a correlated uncertainty would be introduced is so small compared to those of the ^{233}U and ^{236}U countrates that it is ignored.

For calculating the turn-by-turn ^{239}Pu/^{242}Pu ratio for a sample, it is again necessary to first calculate them for each run and then combine them suitably. In a given run i the pulser counts p_{239} and p_{242} as well as the respective numbers of events in the X+ bins m_{239} and m_{242} have to be recorded for all runs. The calculation of the countrates r_{239_i} for ^{239}Pu and r_{242_i} for ^{242}Pu and their associated (internal) uncertainties Δr_{239_i} and Δr_{242_i} for a given run i is identical to that for the ^{236}U count rate r in the previous section. Dividing r_{239_i} by r_{242_i} yields the ratio $(r_{239}/r_{242})_i$ for run i. In contrast to the ^{236}U/^{238}U case where the statistical uncertainty of the ^{238}U current was negligible now both isotopes have a comparable statistical error, and Gaussian error propagation for statistically independent uncertainties is used to calculate $\Delta(r_{239}/r_{242})_i$.

The weights for the calculation of the weighted mean for the r_{239}/r_{242} ratio over all k runs on this target are defined as

$$w_i = \frac{1}{\left(\left(\Delta\frac{r_{239}}{r_{242}}\right)_i\right)^2} \tag{4.3.4}$$

The turn-by-turn ratio is then

$$\frac{r_{239}}{r_{242}} = \frac{\sum_{i=1}^{k} w_i \cdot \left(\frac{r_{239}}{r_{242}}\right)_i}{\sum_{i=1}^{k} w_i} \tag{4.3.5}$$

Using Gaussian error propagation, the internal uncertainty for this weighted mean $\Delta_{int}(r_{239}/r_{242})$ can be derived. The empirical standard deviation over all k runs is used to calculate the external uncertainty $\Delta_{ext}(r_{239}/r_{242})$. The uncertainty of the turn-by-turn ratio r_{239}/r_{242} is then defined as the larger of those two.

For the combined evaluation, each type of data relevant for the evaluation is first summed up over all k runs on a given target. As in the case of ^{236}U the equations including those for the uncertainties are then identical to that for a single run in the turn-by-turn evaluation described in detail above. Finally, the ratio ^{239}Pu/^{242}Pu is defined as the turn-by-turn calculated ratio r_{239}/r_{242} for all targets with more than 20 counts, and the combined r_{239}/r_{242} ratio for those with less counts.

4.4 Blank correction and calculation of concentrations

As process blanks only contain U from supra pure reagents, a very low overall uranium content is expected and therefore even small anthropogenic contaminations that might be of negligible impact on the ratios in environmental samples can result in very high ^{236}U/^{238}U and ^{233}U/^{238}U ratios. These ratios are therefore not suited for blank correction, leaving the average countrates for those isotopes as the best option for comparing the blank levels. These average countrates are not normalized, so the fluctuations and drifts in various machine parameters from ion

source output to transmission are not compensated for. Under these circumstances only a rough, qualitative assessment is possible. If the count rate on the isotope of interest in the environmental sample is equal or lower than that of the corresponding blank, the content of the sample is assumed to be below the sensitivity of the measurement due to the background, and the measured ratios are assumed to be dominated by this background. If the count rate of the sample is less than three times the count rate of the corresponding blank it is considered heavily influenced by the contaminations responsible for the content of the blanks. In that case only qualitative interpretations of samples in this category are possible and a potential contamination of them has to be considered. For larger countrates it is assumed that the original environmental isotopic ratio dominates the influence of contaminations at the blank level.

For plutonium the absolute number of ^{239,240}Pu atoms in the initial sample can be determined using the ^{242}Pu spike. The number $n(^{242}\mathrm{Pu})$ of ^{242}Pu atoms spiked to a sample and can be calculated from the concentration and the amount of spike solution added and is noted in tables 3.1.2 and 3.1.3 for all samples. From $n(^{242}\mathrm{Pu})$ along with the $^{239}\mathrm{Pu}/^{242}\mathrm{Pu}$ and $^{240}\mathrm{Pu}/^{239}\mathrm{Pu}$ ratios determined as described in the previous section, the numbers n(^{239}Pu) of ^{239}Pu and $n(^{240}\mathrm{Pu})$ of ^{240}Pu atoms can easily be calculated as:

$$n(^{239}\mathrm{Pu}) = n(^{242}\mathrm{Pu}) \cdot \frac{r^{239}\mathrm{Pu}}{r^{242}\mathrm{Pu}} \text{ and } n(^{240}\mathrm{Pu}) = n(^{239}\mathrm{Pu}) \cdot \frac{r^{240}\mathrm{Pu}}{r^{239}\mathrm{Pu}} \tag{4.4.1}$$

As both the ratio and the amount of the respective reference isotope have relevant uncertainties, the uncertainties of $n(^{239}\mathrm{Pu})$ and $n(^{240}\mathrm{Pu})$ can be calculated via Gaussian error propagation for multiplicatively linked quantities.

At this stage $n(^{239}\mathrm{Pu})$ and $n(^{240}\mathrm{Pu})$ can be blank corrected for each sample by subtracting from them the corresponding values of the appropriate chemical blanks. Subtracting quantities of similar magnitude leads to a dramatic increase of the relative uncertainty, as the individual uncertainties are quadratically added, so for reliable results the sample value should be higher than the blank by at least a factor of three. Samples closer to the blank level might be heavily influenced by the contaminations or background that resulted in that elevated blank level. For

some surface water samples $n(^{239}\mathrm{Pu})$ or $n(^{240}\mathrm{Pu})$ is even slightly below the corresponding blank level, while still compatible within the 1σ uncertainties. For these samples it is impossible to determine the ratio of plutonium collected during the sampling. While a blank correction by subtraction would result in negative values for $n(^{239}\mathrm{Pu})$ or $n(^{240}\mathrm{Pu})$ 0 is the natural lower limit for the number of atoms in any sample. The 1σ uncertainties of $n(^{239}\mathrm{Pu})$ and $n(^{240}\mathrm{Pu})$ taken from this lower limit are a reasonable choice for the upper limits of these values.

To calculate the concentration $c(^{239}\mathrm{Pu})$ or $c(^{240}\mathrm{Pu})$ in atoms per kilogram in a given sample, $n(^{239}\mathrm{Pu})$ or $n(^{240}\mathrm{Pu})$ are divided by the sample mass. The scale used has a measurement uncertainty of 2 g when near the maximum load capacity based on some simple reproducibility experiments. The samples were too large to be weighed directly and had to be partitioned. Up to 4 kilos of the sample were poured into the evaporator used for preconcentration and weighted in this vessel, while the rest was poured directly into a large beaker glass and weighed there. Under this lighter load of around 1kg the uncertainty of of the scale is reduced to the 1g stated on the device. Measuring a single sample mass combines four measurements (two vessels, empty and full). As the evaporator fraction was concentrated from $\approx$ 4 l to $\approx$1 l, losses during the transfer of the preconcentrated sample fraction from the evaporator to the beaker would have to be multiplied by the same factor. Even though care was taken to avoid all such losses, sometimes small droplets were spilled during transfers. The uncertainty for the sample mass is thus conservatively estimated at 10g while that for the process blank masses at 1g. The uncertainty for the concentrations can then be calculated from the uncertainty of the sample mass and of the $n(^{239}\mathrm{Pu})$ or $n(^{240}\mathrm{Pu})$ with Gaussian error propagation for multiplicatively linked quantities.

For the calculation of the concentration in at/m^3 the average density of the seawater samples was calculated as 1026.94 ± 0.15 kg per m^3 in chapter 3.1. In some publications ^{239}Pu, ^{240}Pu or $^{239+240}$Pu activities are stated as $\mathrm{mBq/m^3}$, μBq/kg or μBq/l instead of concentrations. Using the half-lifes 24110 ± 30 years for ^{239}Pu and 6561 ± 7 years for ^{240}Pu as stated in table 2.1.1, these can easily be calculated from the concentrations in atoms per kilo or atoms per cubic meter by the decay law and the appropriate factors for the unit conversions.

4.5 Quality of the data

For quality assurance two materials with well-known isotopic ratios were measured alongside the samples and blanks in the beamtimes relevant for this thesis: The Vienna-KkU and Vienna-US8 in house uranium standards introduced in 3.2. The Vienna US-8 material is used to determine the turn-by-turn detection efficiency to normalize the $^{236}U/^{238}U$ ratios for the Vienna-KkU targets as described in 4.3.1. Figure 4.5.1 shows the $^{236}U/^{238}U$ ratios for Vienna-KkU targets from the three beamtimes relevant for the environmental samples along with the reference ratio from (Vockenhuber et al. 2002) for the standard and the weighted mean for the targets over all three beamtimes. All targets fall within the 1σ range of the reference value $(6.98 \pm 0.32) \cdot 10^{-11}$ from (Vockenhuber et al. 2002) and the standard deviation of the mean of the measured targets overlaps with the reference value. The reproduction of the reference ratio on this uranium standard indicates that the measurements produced reliable results.

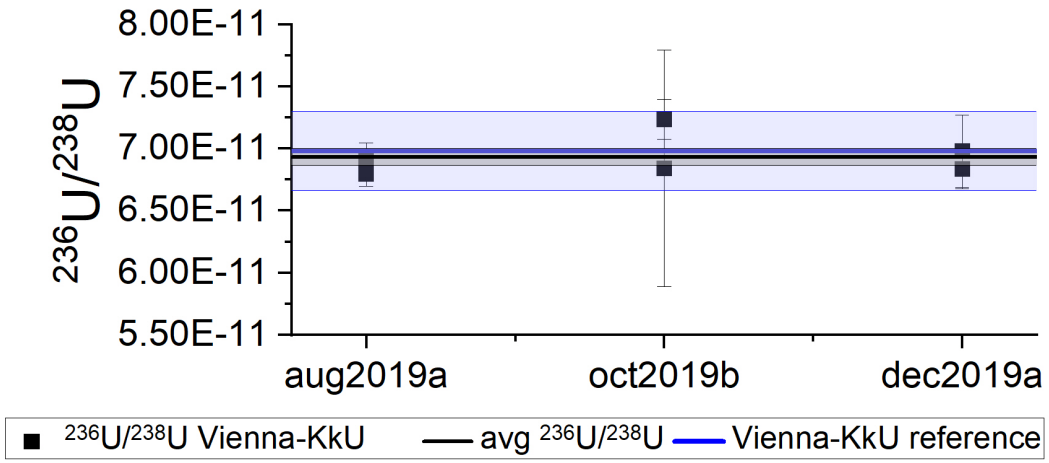

Figure 4.5.1: Measured $^{236}U/^{238}U$ isotopic ratio for the uranium standard Vienna-KkU. Each black point represents the result of a cathode of this material with 1σ uncertainty from all runs in the respective beamtime calculated as introduced in 4.3.1. One sample in the oct/2019b beamtime was only measured for a short time, resulting in a very large statistical uncertainty. The black line represents the weighted mean with a 1σ uncertainty of the mean shaded in gray, while the blue line with a 1σ uncertainty shaded in blue is the reference ratio published in (Vockenhuber et al. 2002).

4.6 Suppression of hydrides

The primordial radionuclides ^{232}Th, ^{235}U, and ^{238}U are separated by only one mass from the trace isotopes of interest, i.e. ^{233}U,^{236} U and ^{238}U. For these heavy nuclides this represents a much smaller relative mass difference than that between ^{13}C and ^{14}C. As stated in 4.1.3 metastable ^{232}ThH^{3+}, ^{238}UH^{3+} and ^{235}UH^{3+} hydride-ions exist and an increased stripper gas pressure is required to suppress them (Lachner et al. 2012).

The contribution of ^{238}UH^{3+} to the mass 239 count rate of the plutonium-targets is estimated in the following based on data from the heavy/aug2019c beamtime in the form of a worst-case estimation. The highest countrate on mass 239 for all uranium standards was achieved on the Vienna-KkU target on position 10 at (0.0269 ± 0.0072) cps. As part of this worst-case estimation it is assumed that all mass 239 events on this KkU target were due to surviving ^{238}UH^{3+}. The average ^{238}U current for this target was $6.1889 \cdot 10^{-9} A$. The plutonium sample with the highest interpolated average ^{238}U current based on ^{234}U events was CL-21_2000m at $7.89881 \cdot 10^{-12}$ A with a mass 239 count rate of (1.1420 ± 0.021) cps. Assuming the same ^{238}UH$^{3+}/^{238}$U ratio as for the KkU target from cathode 10, an average ^{238}UH^{3+} count rate of $(3.42 \pm 0.92) \cdot 10^{-5}$ cps on can be estimated on this target. As this is two orders of magnitude below even the lowest mass 239 countrates from the shallow water samples analyzed for this thesis, the influence of ^{238}UH^{3+} on the mass 239 events can be neglected. All events with mass 239 are therefore assumed to be ^{239}Pu and are referred to as such throughout this thesis.

As ^{235}UH^{3+} are chemically identical to the aforementioned ^{238}UH^{3+}, the hydride suppression for mass 236 is assumed to work equally well. Considering the natural isotopic ratio of ^{235}U/^{238}U ≈ 0.0072, a ratio of ^{235}UH$^{3+}/^{238}$U $< 10^{-14}$ would be expected. As this is two to five orders of magnitude below the ^{236}U/^{238}U ratios determined for the environmental samples this hydride ion will also be neglected and events on mass 236 are identified as ^{236}U in this thesis.

The triply charged thorium hydride ^{232}ThH^{3+} shows higher metastability than the uranium hydrides according to the aforementioned paper by Lachner et al., so there is a higher probability that they can reach the detector. Based on previous

experience with ^{233}U measurements at VERA at various stripper gas pressures it was assumed, that the increased stripper gas pressure for actinide measurements as described in 4.1.3 is sufficient to suppress $^{232}ThH^{3+}$.

However, a possible influence by $^{232}ThH^{3+}$ or other molecules or molecular fragments on the sporadic targets with very high mass 233 to mass 236 ratios occurring at VERA has to be considered separately. CL-21 1500m is the most extreme example from this group to date, with a 233/236 ratio of 0.599 ± 0.069 measured in the beamtime oct/2019b, while the average ^{232}Th countrate of (17586±28) cps lies well within the countrates of the other samples with much lower $^{233}U/^{236}U$ ratios ranging from (10477±24) cps on Cl-21 2500 m to (27341±43) cps for CL-21 100 m. The deviation of the measured pulser rate from the set rate indicates significant dead time losses of 13%-65% which are comparable to the losses at similar rates on other targets with much lower $^{233}U/^{236}U$ ratios. Based on these considerations, the high $^{233}U/^{236}U$ ratio cannot be explained by an increased ^{232}Th countrate and resulting $^{232}ThH^{3+}$ background.

5 Plutonium in the environmental samples

5.1 Combining the results from different beamtimes

The blank B1Pu corresponding to the plutonium samples CL-21 20 m, CL-21 300 m and CL-21 2000 m was not mounted on the wheel during the heavy/aug2019c beamtime by accident. The targets along with their blank were measured again during the heavy/dec2019a beamtime i.e. without any additional sample preparation. In order to increase the statistics of the corresponding results, the data from both measurements are combined. Significant discrepancies between the results from the two beamtimes might indicate a contamination introduced after the first beamtime, or a different ratio of the ion optical transmissions for ^{239}Pu, ^{240}Pu and ^{242}Pu. In order to verify whether the blank level obtained in beam time dec2019a is also representative for beamtime aug2019c, and as a measure of quality assurance the results for ^{239}Pu and ^{240}Pu from both beamtimes are compared in figure 5.1.1.

All n(^{240}Pu) and one of the n(^{239}Pu) results are in agreement within the 1σ uncertainties, while the remaining two ^{239}Pu results are within the 2σ uncertainties. Based on this the blank level from heavy/dec2019a can be used for the heavy/aug2019c results for the three targets CL-21 20 m, CL-21 300 m and CL-21 2000 m. The results were combined as the weighted mean over the blank corrected concentrations for all turns in both beamtimes.

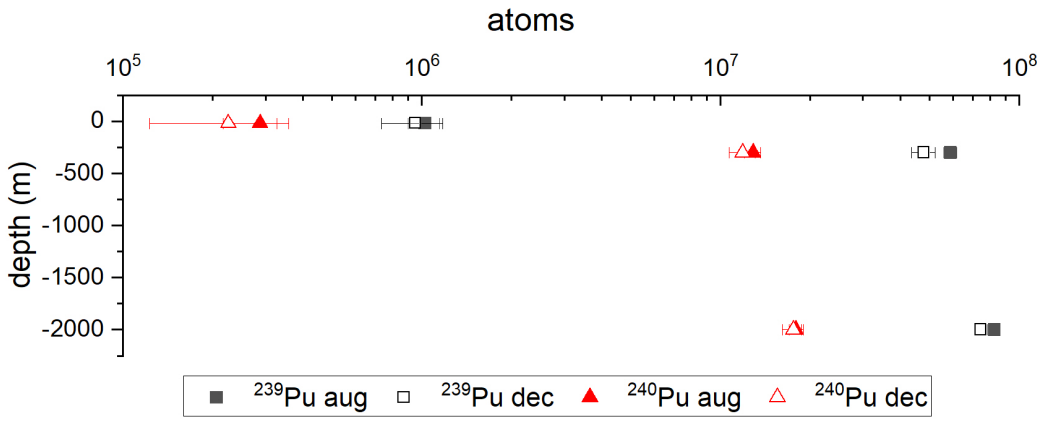

Figure 5.1.1: Comparison of n(^{239}Pu) and n(^{240}Pu) in atoms per sample before blank correction for the three samples in the first environmental sample batch from sampling station CL-21 in the two beamtimes aug2019c (aug) and dec2019a (dec).

5.2 Identification of mixed up targets

During the evaluation of the results from CL-21 the numbers of ^{239}Pu and ^{240}Pu for one sample and one blank were peculiar and will be investigated in the following section. The numbers of ^{239}Pu and ^{240}Pu atoms in each sample from station CL-21 before blank correction is shown in figure 5.2.1. The results for the corresponding blanks are plotted above this depth profile as labeled on the vertical axis. Each color and symbol corresponds to a chemistry batch. The positions of the blank B3Pu for batch 3 and the 1500 m sample are surprising in both plots. The amount of plutonium in this supposed blank is comparable to the high content of all the samples below 500 m depth. All other blanks are one or even two orders of magnitude lower than the blank from batch 3. The 1500 m sample on the other hand is comparable to surface water samples and the blanks from other batches, even though all other depths from 500 m to 3000 m fall within a very narrow band, two orders of magnitude above the 1500 m sample. The average ^{242}Pu countrates for B3Pu at 1.950 ± 0.037 cps and the CL-21 1500 m sample at 2.561 ± 0.049 cps indicate a comparable chemical yield for both targets. All runs on these two targets show the same pattern and no irregularities can be seen in the peak height vs width diagram, the currents or the source output.

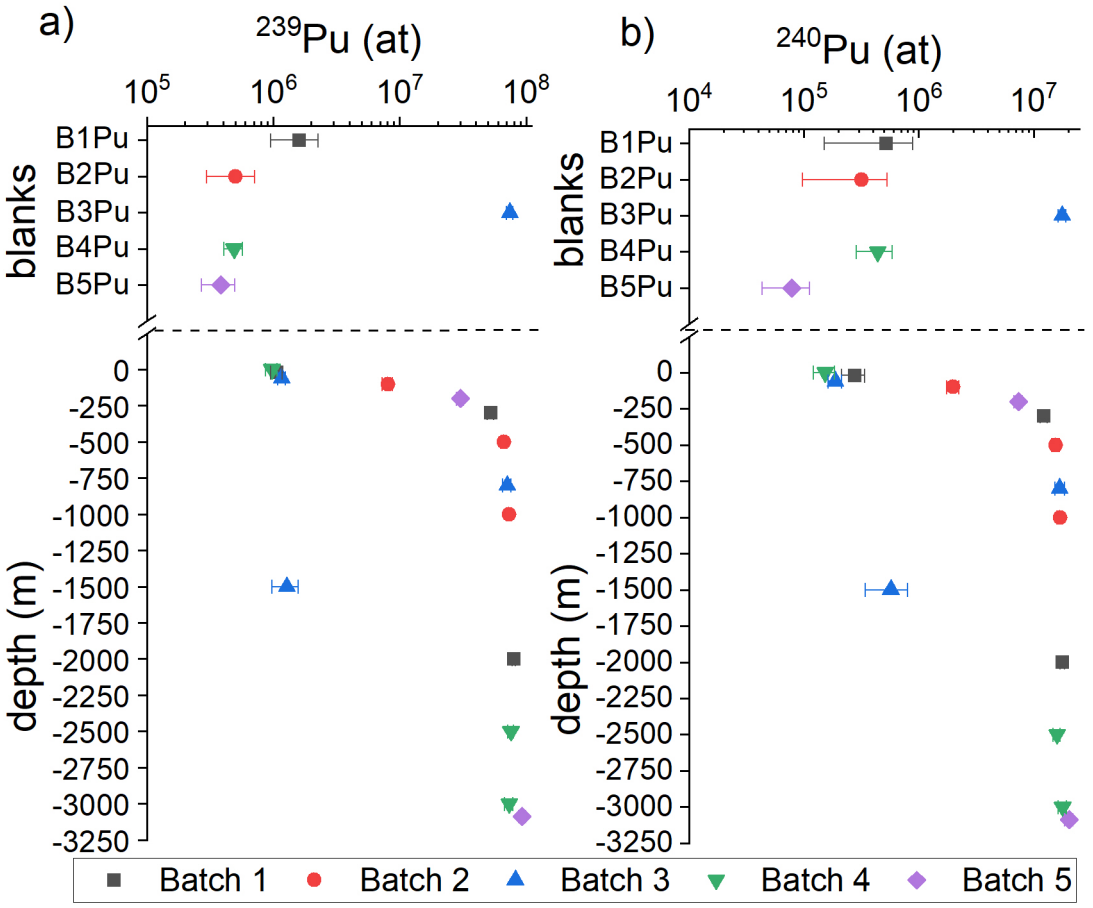

Figure 5.2.1: Vertical distributions of the numbers of n(^{239}Pu) (plot a)) and n(^{240}Pu) (plot b)) in atoms per sample before blank correction. The results of the blanks for each chemistry batch are plotted above the depth profiles. Each color and symbol corresponds to a chemistry batch. The results for B3Pu are extremely high for a blank, while those of CL-21 1500 m are extraordinarily low for this sampling depth.

There are two alternatives to consider: Either the data is correct as presented above, or B3Pu and CL-21 1500 m were mixed up and placed in the wrong position on the wheel. Assuming everything is correct, the data would indicate a massive contamination of the blank with ^{239}Pu, ^{240}Pu but not ^{242}Pu. Considering the concentrations the other environmental samples can be excluded as contamination sources, as the whole sample would have had to be used to produce the result measured in B3Pu. No ^{239}Pu and ^{240}Pu spike solutions are used at VERA. Reference material like IAEA443 Irish Seawater was not processed at the time of the

sample preparation, and all labware used for such materials is labeled as and not used for environmental samples. The only other plutonium samples with higher concentrations processed in the same lab in the months before the sample preparation for this work also used a different set of labware to avoid cross-contaminations. Environmental plutonium samples at the VERA labs are spiked with ^{242}Pu even before removing the sample from the transport vessel. A contamination of this blank by a large proportion of an already spiked environmental sample would be expected to show elevated ^{242}Pu countrates as well, as the amount of spike in the bank would be increased as well. The additional assumption of a lower chemical or ionization yield for B3Pu offsetting this additional input of ^{242}Pu spike would be required to explain the data. Besides, a decrease of the concentration of both, ^{239}Pu and ^{240}Pu, by two orders of magnitude at one specific depth only would be hard to explain. No comparable depth profile for plutonium in seawater was found during a literature search, and no mechanism that could produce such a distinct pattern at this depth comes to mind. No anomalies have been observed in the oceanographic parameters (salinity, temperature and DO). Categorizing CL-21 1500 m as an outlier would also be problematic, as the measurement of the spike worked well, all runs are consistent, and no other problems could be identified.

Each batch consisted of three samples and one blank which were processed in parallel wherever possible. The most probable scenario is that samples were mixed up during calcination or after pressing the material into the target holders as direct labeling of the quartz crucible as well as target holders is not possible. A reevaluation of the data under this assumption yields the depth profiles plotted in figure 5.2.2. In that case, the plutonium content of B4Pu is consistent with the other plutonium blanks. The numbers of ^{239}Pu and ^{240}Pu atoms in CL-21-1500m are now close to those in the samples above and below. Whilst this does not amount to definite proof, the balance of probability overwhelmingly points towards the mix-up hypothesis. From this point on it is assumed that the blank B3Pu and the plutonium target from sample CL-21-1500 m were mixed up at some stage, so the data from position 10 on the target wheel originally labeled CL-21 1500 Pu is now associated with B3Pu, whilst the data from position 7 originally labeled B3Pu is now associated with CL-21 1500 Pu.

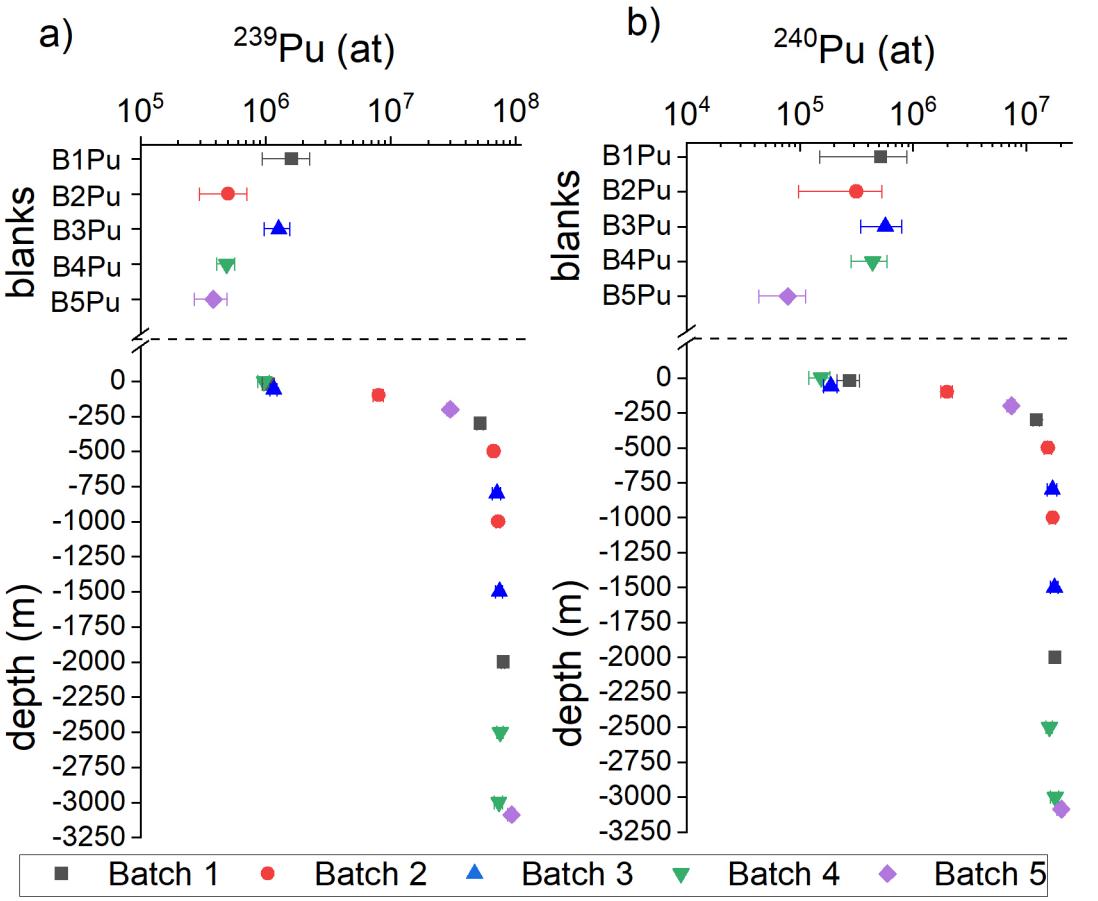

Figure 5.2.2: Vertical distributions of n(^{239}Pu) (plot a)) and n(^{240}Pu) (plot b)) atoms per sample before blank correction after exchanging the positions of B3Pu and CL-21 1500 m. The results of the blanks for each chemistry batch are plotted above the water column with the same color and symbol as the corresponding samples. The result for B3Pu is now comparable to the other blanks, and the number of ^{239}Pu and ^{240}Pu atoms in CL-21 1500 m fit in with those the samples above and below.

5.3 Blank correction

As discussed in 4.4 a quantitative blank correction can only be considered as reliable, if the blank level is much lower than the sample value. In figure 5.2.2 it can be observed, that results from samples close to the surface are near the blank level. The number of ^{239}Pu atoms in the samples from 20 m and 60 m are compatible with the blank level within the 1σ uncertainties, as is that of the 20 m sample for ^{240}Pu.

The samples from 0 m and 60 m are below the 1σ range of the corresponding blank levels for n(^{240}Pu). For the samples where the measured n(^{239}Pu) and n(^{240}Pu) values are below those of the corresponding blanks, a quantitative blank correction is not possible, instead upper and lower limits are stated as discussed in 4.4. While the number of ^{239}Pu atoms in the CL-21-0 m sample is comparable to the two samples just discussed, the lower blank level in batch 4 formally allows for the quantitative blank correction. As the number of ^{239}Pu atoms in this sample is just less than twice that in the corresponding blank B4Pu the sample may however still be heavily influenced by the contaminations resulting in the blank level.

For CL-21-100 m n(^{239}Pu) and n(^{240}Pu) are already well above those of the corresponding chemistry blank B2Pu. All other samples are at least an order of magnitude above their corresponding blank levels for ^{239}Pu and ^{240}Pu. For these samples a quantitative blank correction can be applied. The same procedure is used for the samples from station CL-20: Figure 5.3.1 shows n(^{239}Pu) and n(^{240}Pu) for the two relevant blanks B6Pu and B7Pu and the four CL-20 samples.

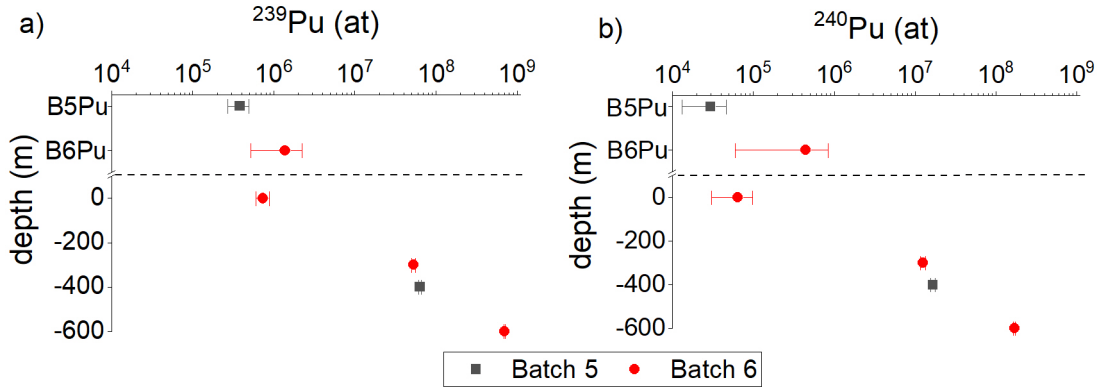

Figure 5.3.1: Blank levels and vertical distribution of n(^{239}Pu) (left) and n(^{240}Pu) (right) before blank correction for CL-20. The two relevant blanks are plotted above the four samples at the labeled vertical positions.

5.4 Vertical distribution of plutonium at CL-21

The blank corrected concentration and activity of ^{239}Pu and ^{240}Pu at sampling station CL-21 is plotted against the depth in figure 5.4.1.

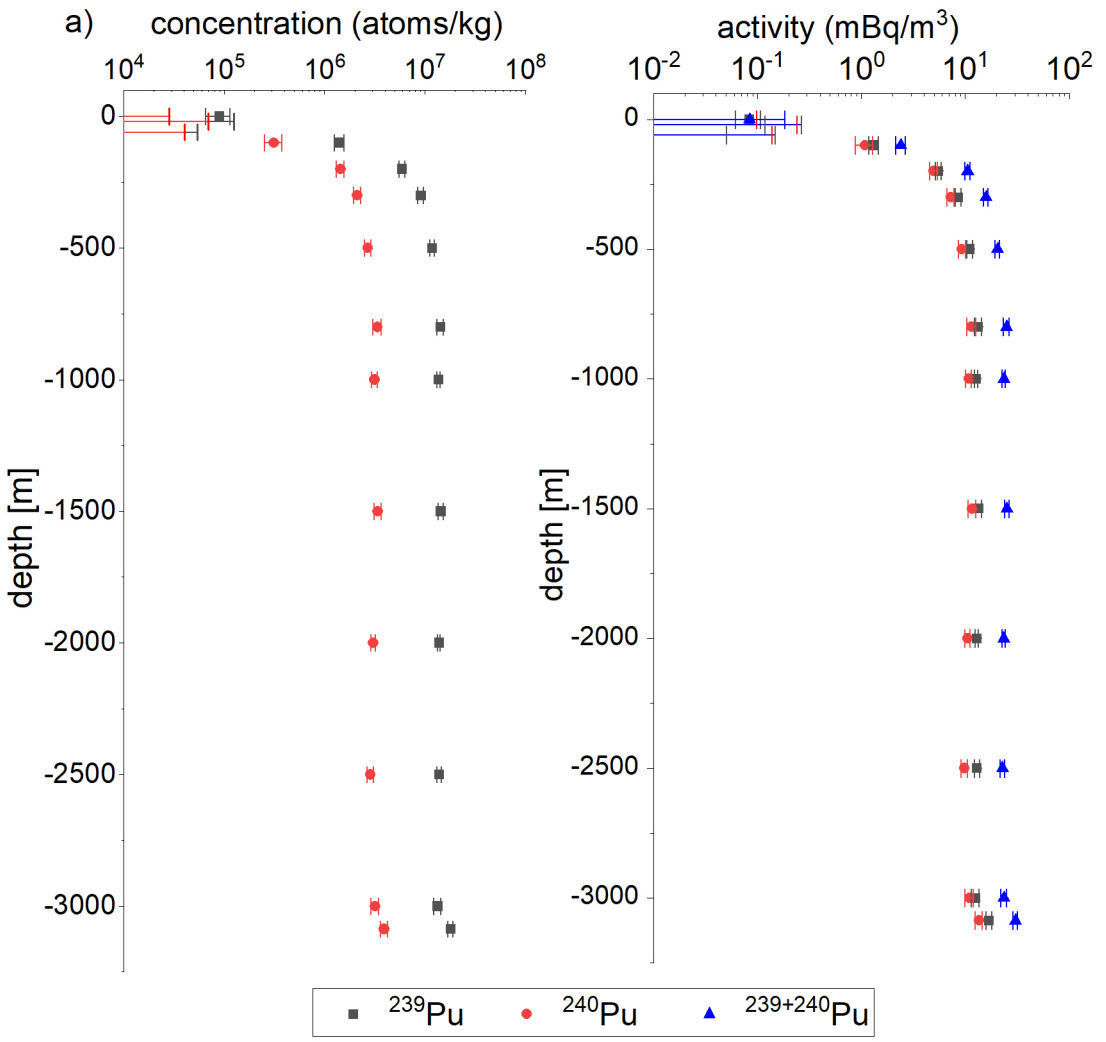

Figure 5.4.1: Depth profiles of ^{239}Pu and ^{240}Pu concentrations (a) and specific activity (b) at sampling station CL-21. The upper limits for the samples from 0-60 m at or below the blank level are shown as 1σ uncertainty error bars, with the lower limit outside the plot.

The underlying data is listed in table 5.4.1 at the end of this section. The activity of $^{239+240}$Pu is included in the activity plot to allow for direct comparison with decay counting results obtained by $\alpha-$spectrometry. The upper limits for the samples from 0-60 m at or below the blank level are shown as 1σ uncertainty error bars, with the lower limit of 0 atoms/kg outside the plot.These isotope depth profiles shown in figure 5.4.1 are unusual, as they lack the characteristic feature of

the typical plutonium depth profile - a prominent subsurface maximum between 500 m and 1000 m depth. The concentrations for both plutonium isotopes are almost constant between 800 m and 3000 m depth. The profile looks similar to the DYFAMED profile introduced in 2.2.2. A subsurface maximum is generally attributed to the decomposition of sinking biogenic particles and the resulting resuspension of the plutonium. A high vertical particle flux has been reported for the eastern North Pacific in (Fowler et al. 1983) and might in conjunction with the local bathymetry and geology explain the unusual vertical distribution including the overall maximum near the bottom seen at this sampling station. This will be addressed in more detail in 5.6. Figure 5.4.2 shows the corresponding vertical distribution of the isotopic ratio of $^{240}Pu/^{239}Pu$ for CL-21 for all depths where reliable blank corrected concentrations could be calculated, in other words from 100 m to 3087 m depth. These ratios are also included in table 5.4.1. The weighted

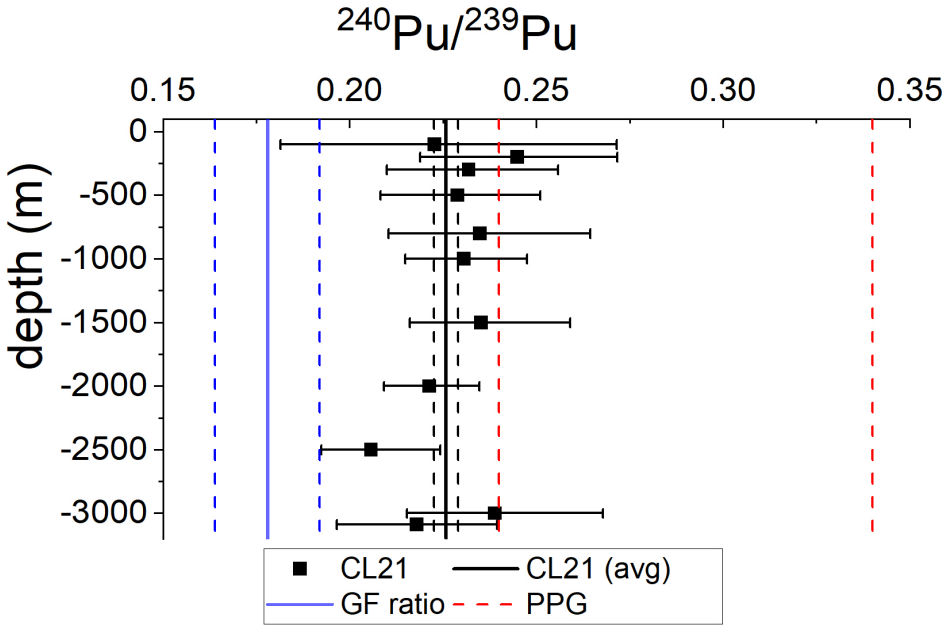

Figure 5.4.2: Vertical distribution of the $^{240}Pu/^{239}Pu$ ratios at sampling station CL-21 along with the average ratios for global fallout (blue) and tropospheric fallout from the Pacific Proving Grounds (PPG, red area) as introduced in 2.1.2

average $^{240}Pu/^{239}Pu$ ratio for CL-21 is 0.2259 ± 0.0033. All samples overlap with this mean within their 1σ uncertainties and no clear trend beyond the statistical scatter is discernible. In consequence no relevant change in the isotopic ratio of

$^{240}Pu/^{239}Pu$ with increasing depth can be derived from the data in figure 5.4.2. The average ratio stated above is considered to describe the isotopic ratio at all depths best, and the ratio is assumed to be constant. The blue line in figure 5.2.4 shows the typical $^{240}Pu/^{239}Pu$ ratio for global fallout of 0.178±0.014 and the red line marks the average tropospheric fallout ratio from the Pacific Proving Grounds of 0.24-0.34 (Krey et al. 1976) (Buesseler 1997). The $^{240}Pu/^{239}Pu$ ratio at sampling station CL-21 falls between these two major sources for plutonium in seawater of the Pacific Ocean. Applying the mixing model introduced in chapter 2.1.1 is problematic due to the wide range of the PPG tropospheric fallout ratios, even if only these two sources are considered. Depending on the ratio chosen the contribution of the PPG to the plutonium in this sample varies from 31% with the maximum PPG ratio of 0.34 to 82% with the minimum ratio of 0.24. It is remarkable, that the ratio is elevated compared to global fallout even at this large distance from the PPG. There is no indication for the influence of weapons-grade plutonium at CL-21. As the samples from 0 m, 20 m and 60 m were too close to the blank level for one or both of the isotopes of interest nothing can be said about the $^{240}Pu/^{239}Pu$ ratio near the surface, where the weapons-grade signature was found for the BD-17 0 m sample in (Hain et al. 2017).

Table 5.4.1 contains the data underlying the depth profiles for sampling station CL-21with 1σ-uncertainties. For the two samples at 20 m and 60 m the 1 σ upper limit is given instead of concentrations, and consequently no isotopic ratios can be calculated from these upper limits.

Depth (m)	^{239}Pu (10^6 at/kg)	^{240}Pu (10^6 at/kg)	^{240}Pu/^{239}Pu
0	0.090 ± 0.024	$\leq$0.029	-
20	≤ 0.13	≤ 0.070	-
60	≤ 0.054	≤ 0.041	-
100	1.41 ± 0.15	0.314 ± 0.060	0.223 ± 0.049
200	5.92 ± 0.38	1.45 ± 0.13	0.245 ± 0.027
300	9.13 ± 0.60	2.12 ± 0.17	0.232 ± 0.024
500	11.84 ± 0.68	2.71 ± 0.21	0.229 ± 0.022
800	14.3 ± 1.1	3.35 ± 0.33	0.235 ± 0.030
1000	13.66 ± 0.53	3.15 ± 0.20	0.231 ± 0.017
1500	14.41 ± 0.88	3.39 ± 0.28	0.235 ± 0.024
2000	13.84 ± 0.45	3.06 ± 0.16	0.221 ± 0.013
2500	13.88 ± 0.79	2.86 ± 0.20	0.206 ± 0.019
3000	13.4 ± 1.1	3.20$\pm$0.29	0.239 ± 0.029
3087	18.1 ± 1.1	3.94 ± 0.31	0.218 ± 0.022

Table 5.4.1: Concentrations of ^{239}Pu, ^{240}Pu and the isotopic ratio ^{240}Pu/^{239}Pu at sampling station CL-21

5.5 Vertical distribution of plutonium at CL-20

The vertical distribution of the ^{239}Pu and ^{240}Pu concentrations and the corresponding specific activities at sampling station CL-20 are plotted in figure 5.5.1. As there are only four samples down to a depth of 600 m out of a total depth of $\approx$ 3630 m only a small part of the full depth profile was analyzed and thus is available for discussion within the frame of this thesis. While concentrations and activity of the three upper samples are comparable to samples from similar depths from CL-21, the 600 m sample is an order of magnitude above all other plutonium samples analyzed for this thesis. This would be consistent with a rise to the prominent subsurface maximum typical for plutonium depth profiles in the open oceans. Without any data beyond 600 m it is however impossible to determine the overall distribution, as it might also remain relatively constant for the remaining depths as seen in CL-21. If the latter was the case, the average plutonium concentration at CL-20 would be an order of magnitude above that at CL-21 just 300km to the east.

The vertical distribution of the ^{240}Pu/^{239}Pu ratio is plotted in figure 5.5.2. The weighted average of the ^{240}Pu/^{239}Pu ratios is 0.2423 $\pm$ 0.0049. This average ^{240}Pu/^{239}Pu ratio for sampling station CL-20 (black) is included in figure 5.5.2 along with those of sampling station CL-21 (green), the global fallout ratio (blue) and the Pacific Proving Grounds (red). The 1 σ uncertainties for all four samples overlap with the uncertainty of the average ratio and as with sampling station CL-21 the average ratio is assumed to be the best predictor for the isotopic ratio at all depths. The data for figures 5.2.5 and 5.2.6 is documented in table 5.5.1.

The calculated average ^{240}Pu/^{239}Pu ratio at station CL-20 is higher than at CL-21. However, a two-sample t test reveals the difference is not statistically significant. The isotopic ratio at CL-20 is consistent with a combination of tropospheric fallout from the Pacific Proving Grounds and global fallout.

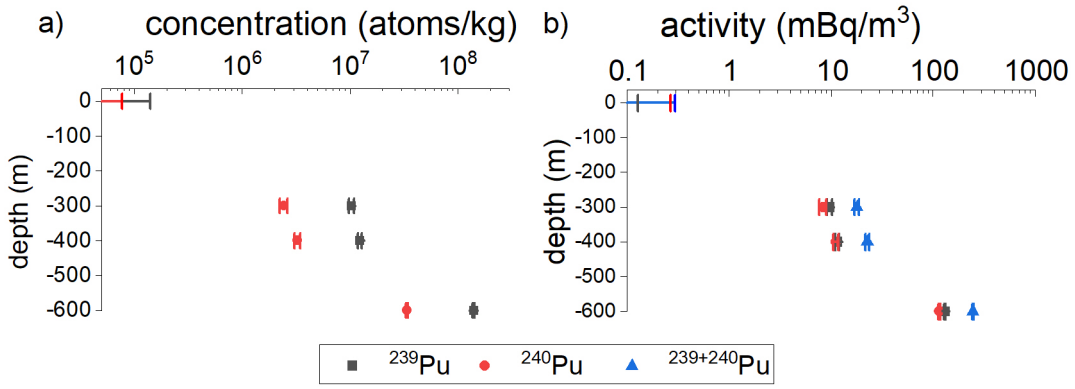

Figure 5.5.1: Vertical distribution of ^{239}Pu and ^{240}Pu concentration (left) and activity (right) at sampling station CL-20 from surface to 600 m depth

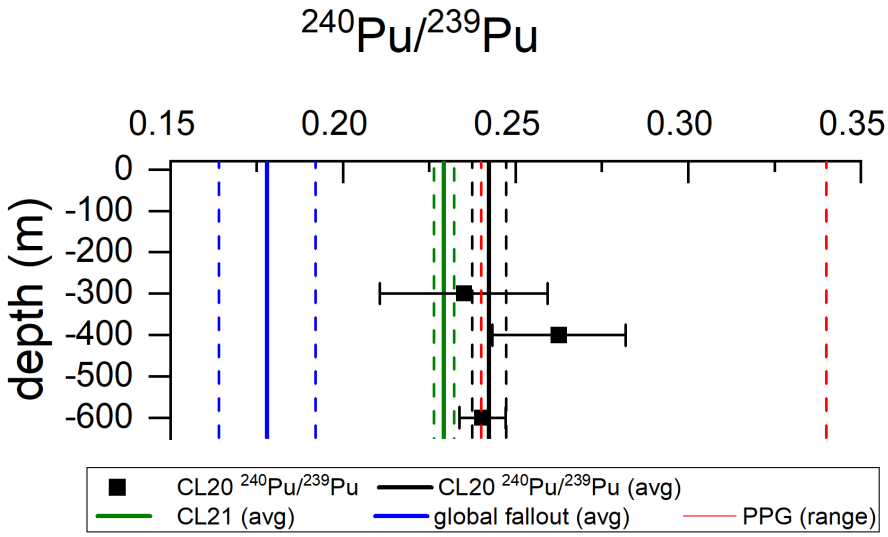

Figure 5.5.2: Vertical distribution of the ^{240}Pu/^{239}Pu ratio at sampling station CL-20 from surface to 600m depth. The average ratios for CL-21, CL-20, global fallout and the wide range for the PPG as introduced in 2.1.2 are included as well.

Depth	^{239}Pu (10^7 at/kg)	^{240}Pu (10^7 at/kg)	^{240}Pu/^{239}Pu
0	≤ 0.014	≤ 0.0077	-
300	1.031 ± 0.061	0.242 ± 0.020	0.235 ± 0.024
400	1.235 ± 0.053	0.324 ± 0.019	0.262 ± 0.019
600	13.90 ± 0.24	3.363 ± 0.076	0.240 ± 0.0068

Table 5.5.1: Concentrations of ^{239}Pu, ^{240}Pu and the isotopic ratio ^{240}Pu/^{239}Pu at sampling station CL-20

5.6 Interpretation of the plutonium results

As pointed out before the vertical distribution of plutonium at station CL-21 does not follow the typical shape for plutonium profiles in the open ocean and therefore requires a closer inspection of the surroundings to identify possible explanations. Figure 5.6.1 shows the major currents in the North Pacific, the general areas of the PPG as well as the sampling stations CL-21 and CL-20 from this work and the BD-17 station from (Hain et al. 2017). The locations of sampling stations from a collection of previous studies from the Pacific Ocean are shown in figure 5.6.1 on the right, the corresponding depth profiles can be found in figures 5.6.3 and 5.6.4.

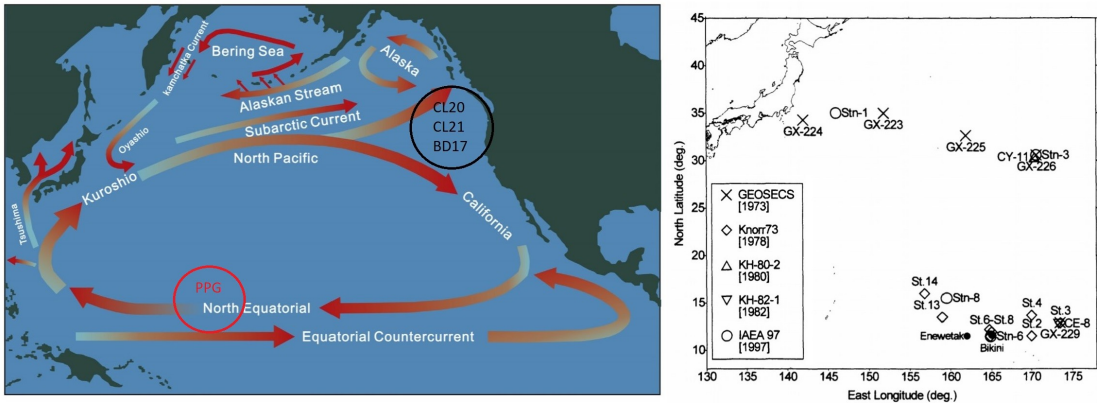

Figure 5.6.1: Major currents in the North Pacific (left) (Chen et al. 2014) and the general areas of the PPG (red circle) and the sampling stations BD-17, CL-21 and CL-20 (black circle). On the right the locations of the sampling stations from the western North Pacific collected in (Livingston et al. 2001) are shown.

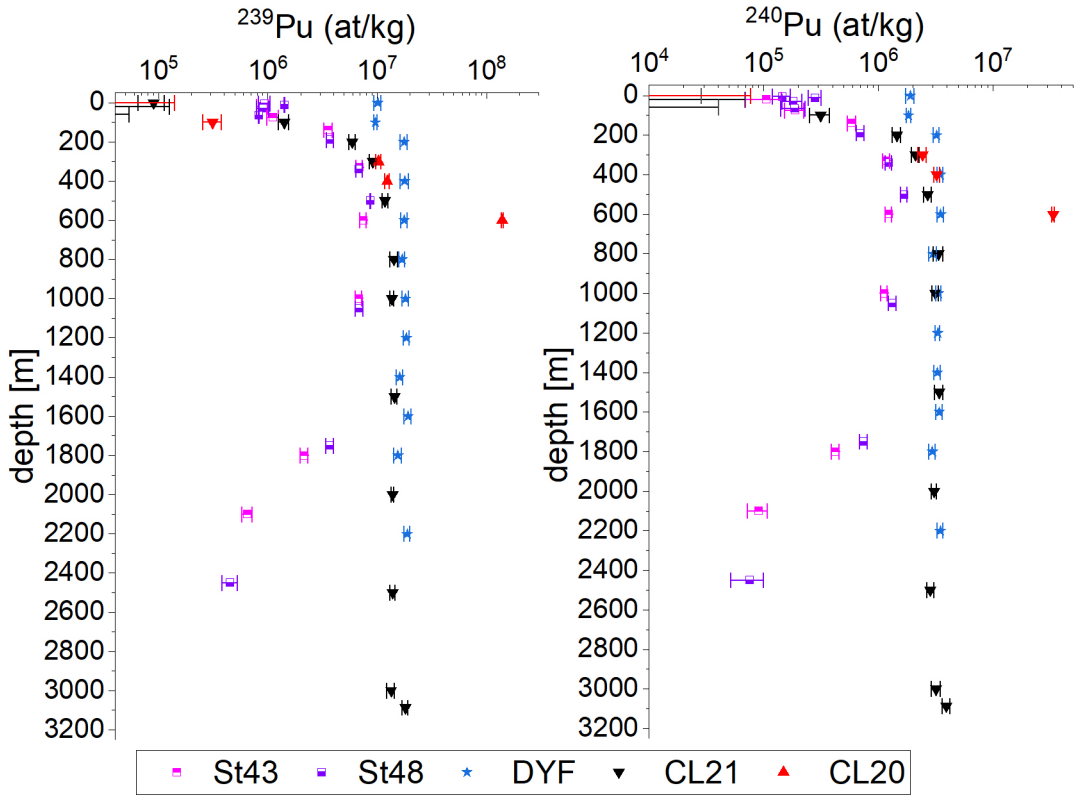

Figure 5.6.2: Vertical distribution of the concentrations of ^{239}Pu and ^{240}Pu at stations CL-21, CL-20 along with St43 and St48 from the Canada Basin and one from the DYFAMED station in the Mediterranean Sea published in (Lòpez Lora 2019).

In figure 5.6.2 the results from stations CL-21 and CL-20 are plotted along with those from (Lòpez Lora 2019). St43 and St48 are samples from the Canada Basin, while DYF is the DYFAMED station from the Mediterranean Sea already shown in 2.2.2. The profiles from the Canada Basin in the Arctic Ocean show a subsurface maximum spread over the depth range from 300 m to 1000 m. The DYFAMED profile and that from CL-21 are remarkably similar with an almost uniform concentration below 600 m, and except for surface water at CL-21 the concentrations of these two stations are consistently higher than the maximum values from the Canada Basin. The 600 m sample from station CL-20 has by far the highest concentration of both ^{239}Pu and ^{240}Pu.

In Figures 5.6.3 and 5.6.4 the calculated $^{239+240}$Pu vertical activity distribution from CL-21 and CL-20 are overlaid with two collections of $^{239+240}$Pu depth profiles

from the Pacific Ocean taken from (Livingston et al. 2001). The GEOSECS, KH-80-2 and IAEA 97 Stn-1 and Stn-3 samples in figure 5.6.3 were taken between latitude 30°N to 35°N and longitude 140°E and 175°E in an area influenced by the Kuroshio, Kuroshio Extension and North Pacific Current. Those in figure 5.6.4 were taken at Latitude 10°N to 17°N and Longitude 155°E to 175°E on the North Equatorial Current. In addition to the collection from Livingston described before and the results from this work in figure 5.6.3 the GEOSECS station 235 at 16°45'N 161°23'W southwest of Hawaii (Bowen et al. 1980) and the Sagami Bay on the east coast of Japan sampled in 1992 (Yamada et al. 2007) were plotted. In figure 5.6.4 the results from the VERTEX I station off the coast of central California sampled in 1980 (Fowler et al. 1983) was added to the collection and the samples from this work. A literature search revealed no other plutonium depth profiles from the eastern North Pacific. As the raw data for some of the profiles was not available to the author, the different data sets were combined graphically. The accuracy of the overlay is adequate for a qualitative comparison of the vertical distribution.

The linear activity axis used in figures 5.6.2 and 5.6.3 for compatibility with the Livingston plot visually highlights the exceptionally high activity of the CL-20 600 m sample compared to that of all other samples in this comparison. Depending on the depth profile used for comparison, the specific activity is a factor 2.6 to 8 higher than the maxima of the other depth profiles. An investigation of the individual runs similar to that in 6.2 for some of the uranium samples revealed no inconsistencies between the runs or anomalies in the data. The IAEA profiles Stn-1 and Stn-3 upstream the North Pacific Current already showed a spread of the subsurface maxima over a larger depth range in 1997 as can be seen in figure 5.6.3. Consequently, such a sharp increase between 400 m and 600 m depth in a sample taken 20 years later is surprising. While a laboratory contamination could explain such a high concentration, this would most likely have had an impact on the $^{240}Pu/^{239}Pu$ ratio as well, which as already stated is not the case. The corresponding blank had a $^{240}Pu/^{239}Pu$ ratio of 0.32 ± 0.34. The low ^{239}Pu and ^{240}Pu content two orders of magnitude below that of the sample resulting in this large uncertainty of the isotopic ratio does not support the laboratory contamination hypothesis, and the absence of anomalies in this or the previous chemistry batch

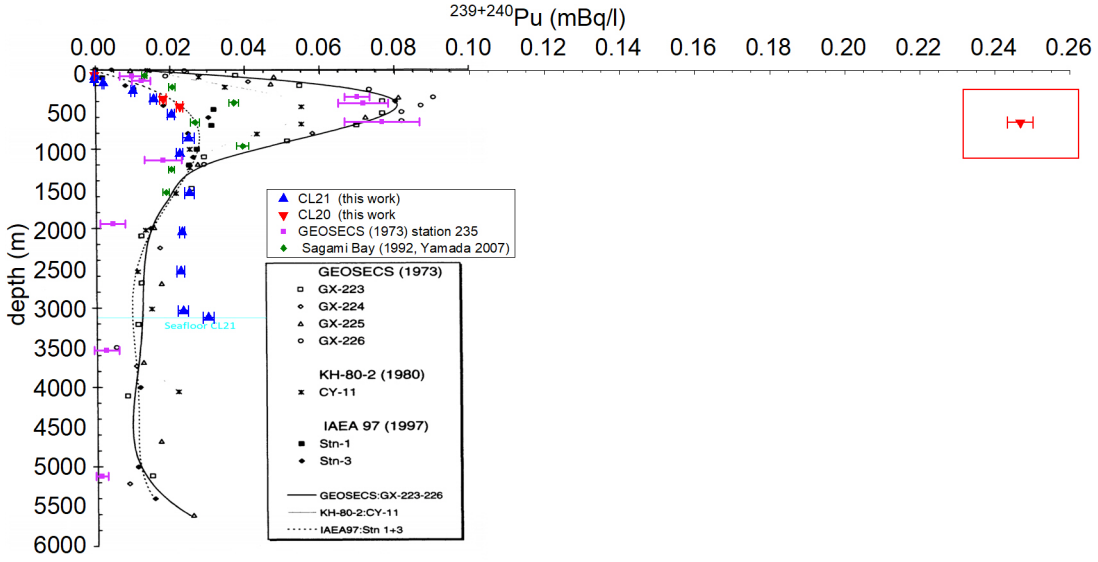

Figure 5.6.3: Overlay of the $^{239+240}$Pu activity from CL-21, CL-20, the GEOSECS station 235 south of Hawaii (Bowen et al. 1980) and a collection of depth profiles from the northern West Pacific including fitted curves indicating the temporal variation published in (Livingston et al. 2001).

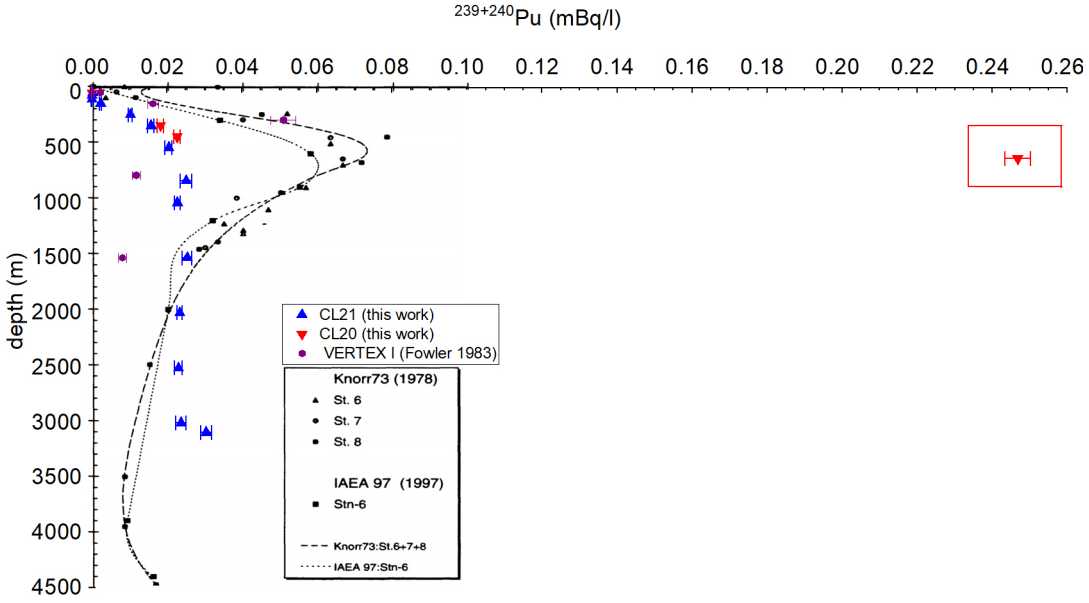

Figure 5.6.4: Overlay of the $^{239+240}$Pu activity from sampling stations CL-21 and CL-20, the VERTEX I station 100km off the California coast sampled in 1980 (Fowler et al. 1983) and a collection of depth profiles from the Western Pacific published in (Livingston et al. 2001)

(the preparation of batches 5 and 6 had several days overlap in the laboratory) further reduces its probability. The already mentioned concentration of plutonium by a factor of up to 10^5 in plankton and other organisms shown by (Wilson et al. 2009) may provide an alternative explanation. Biogenic material in the open ocean is far from uniformly distributed as can be seen in figure 5.6.5 showing the average primary biomass production in January and June 2017 based on the "Global ocean biogeochemistry hindcast" data-set of the Copernicus Marine Service (Perruche et al. 2018). Fowler also demonstrated the relevance of rarer large biogenic particles accumulating smaller particles on the way down for the vertical plutonium flux (Fowler et al. 1983). Without further oceanographic expertise, we can not decide whether a single high content sample could be caused by the chance capture of these large particles and the associated matter. It is unfortunate, that no samples below this depth were available for station CL-20 to clarify the situation.

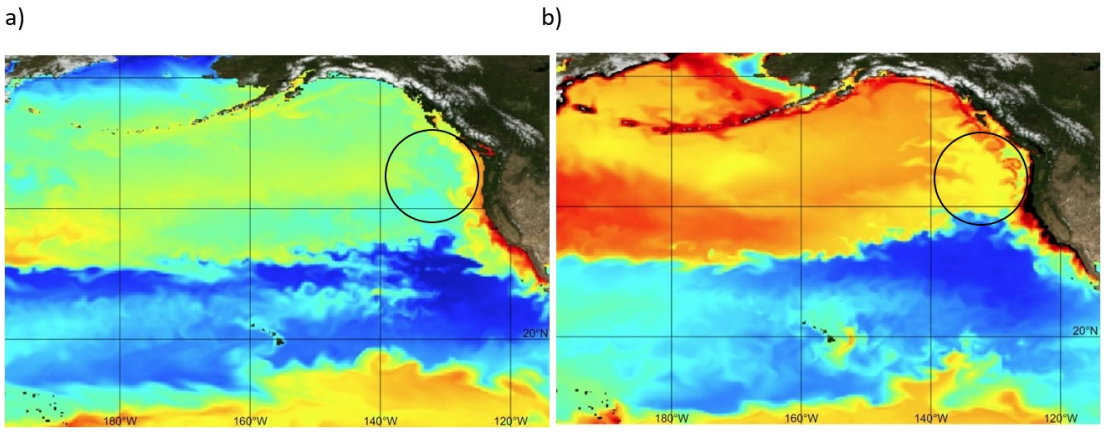

Figure 5.6.5: Monthly averages of the net primary production of biomass in January (a) and June (b) 2017 expressed via the carbon concentration ranging from 0.1 (blue) to 50 (red) mg/m^3 in the Pacific in the GLOBAL_REALANALYSIS_BIO_001_029 dataset of the Copernicus Marine Service (Perruche et al. 2018). Coastal regions shown in black exceed the range of concentrations stated above. The region of sampling stations CL-21 and CL-20 indicated by the black circles. The biomass production in the marked region shows both large local variations as well as a pronounced seasonal cycle.

Despite an oceanographic interpretation is usually beyond the scope of a diploma thesis in physics, a thorough literature research was carried out for the relevant region. The findings are presented in the following together with a tentative in-

terpretation. All depth profiles included in this comparison in figures 5.6.3 and 5.6.4 except for CL-21 (and maybe the incomplete CL-20) exhibit a subsurface maximum. This maximum both sinks and is spread over a larger range of depth over time, as illustrated by the fit functions for the 1973, 1978 and 1997 samples (Livingston et al. 2001) in figures 5.6.3 and 5.6.4. This process is more pronounced in samples collected at northern latitudes presented in figure 5.6.3 and which are in the range of influence of the Kuroshio and North Pacific Current. While the activity at CL-21 is consistently among the lowest for the first 1000 m, this reverses around 1500 m depth, indicating a higher vertical plutonium flux for this region. The vertical flux of plutonium in the water column has been linked to the flux of particles, especially plankton fecal pellets and alumino-silicates in (Fowler et al. 1983). Increased particle densities that would increase the vertical plutonium flux are typically associated with proximity to the coast or river estuaries.

As already stated, the shape of the CL-21 profile is very similar to that of the DYFAMED profile, except for the higher surface water concentrations in the latter. While the vertical flux of plutonium typically correlates with the total mass flux it does so poorly at the DYFAMED station (Bressac et al. 2017). This may be due to the short residence time of the Saharan dust particles making up a considerable and highly variable component of the total vertical particle flux, or a low affinity of plutonium to those aluminum silicates (Bressac et al. 2017). The vertical transport of plutonium at the DYFAMED station is explained by Bressac mainly by sinking particulate organic carbon, with most of the plutonium removal from the water column occurring near the coasts with high sedimentation rates. No direct link between the conditions around the DYFAMED station and near CL-21 is apparent. A closer look at the bathymetry around station CL-21 reveals, that it is situated on the Cobb-Eickelberg Seamount chain, a series of seamounts formed by the Cobb hotspot (Chadwick et al. 2014). Another Seamount rising to ≈500 m depth is 40 km southeast of CL-21, while the summit of Cobb Seamount at a depth of only 30 m below the surface lies 30 km to the south. The distance from the sampling station to the base of Cobb Seamount where it begins to rise from the seafloor is ≈17 km. All distances and depths were measured in Google Earth Pro based on the underwater terrain model. Both seamounts are shown in the top image

in figure 5.6.6, while the middle and bottom image show the currents in 100 m and 1000 m depth. In the following some potential mechanisms by which these seamounts could influence the vertical distribution of plutonium will be explored. Cobb seamount has been studied extensively and significantly increased biological activity mainly due to the shallow depth of the summit plateau has been reported (Dower et al. 1992). An increase in the zooplankton populations was detected up to 30 km from the summit (Dower et al. 1996). A first candidate for particulate matter that might influence the vertical distribution of plutonium at CL-21 would therefore be fecal pellets from zooplankton that are highly effective at binding and transporting plutonium as discussed in the previous paragraph.

A second source of influence would be the seamounts themselves. Erosion through waves and currents might contribute to an increased concentration of suspended particles in the region. The high seismic activity of the region and the active underwater volcano Axial Seamount with major eruptions in 1998, 2011 and 2015 each accompanied by swarms of earthquakes might have increased the overall concentration of particulate matter in the water column (Wilcock et al. 2018). The eruption in 2015 released material with a volume of $2.88 \cdot 10^8\,\mathrm{m}^3$ along with a large amount of thermal energy into the ocean. While the distance to CL-21 is 130 km, this large amount of material released along with advection caused by the input of thermal energy could still change the concentration of suspended particles near the sampling station, depending on local currents.

The North Pacific Current splits into the southward Californian Current and the northward Alaska Current off the US west coast as can be seen in figure 5.6.1. A convergence of water masses typically causes downwelling, while the divergence of currents like that of the southward and northward arm of the North Pacific Current and the Subpolar Current typically cause upwelling (Webb 2019). Along the Alaska Current wind-driven Eikman downwelling occurs (Reid Jr. 1962). Figure 5.6.5 a) shows increased biological activity in the epipelagic zone of the Subpolar Gyre. This indicates that upwelling - whereby nutrient-rich deep water is transported towards the upper layers penetrated by sunlight - plays a more important part for the Subpolar Gyre than for the Subtropical Gyre with the Kuroshio and the North Pacific Current. Increased vertical mixing would also influence the shape of the

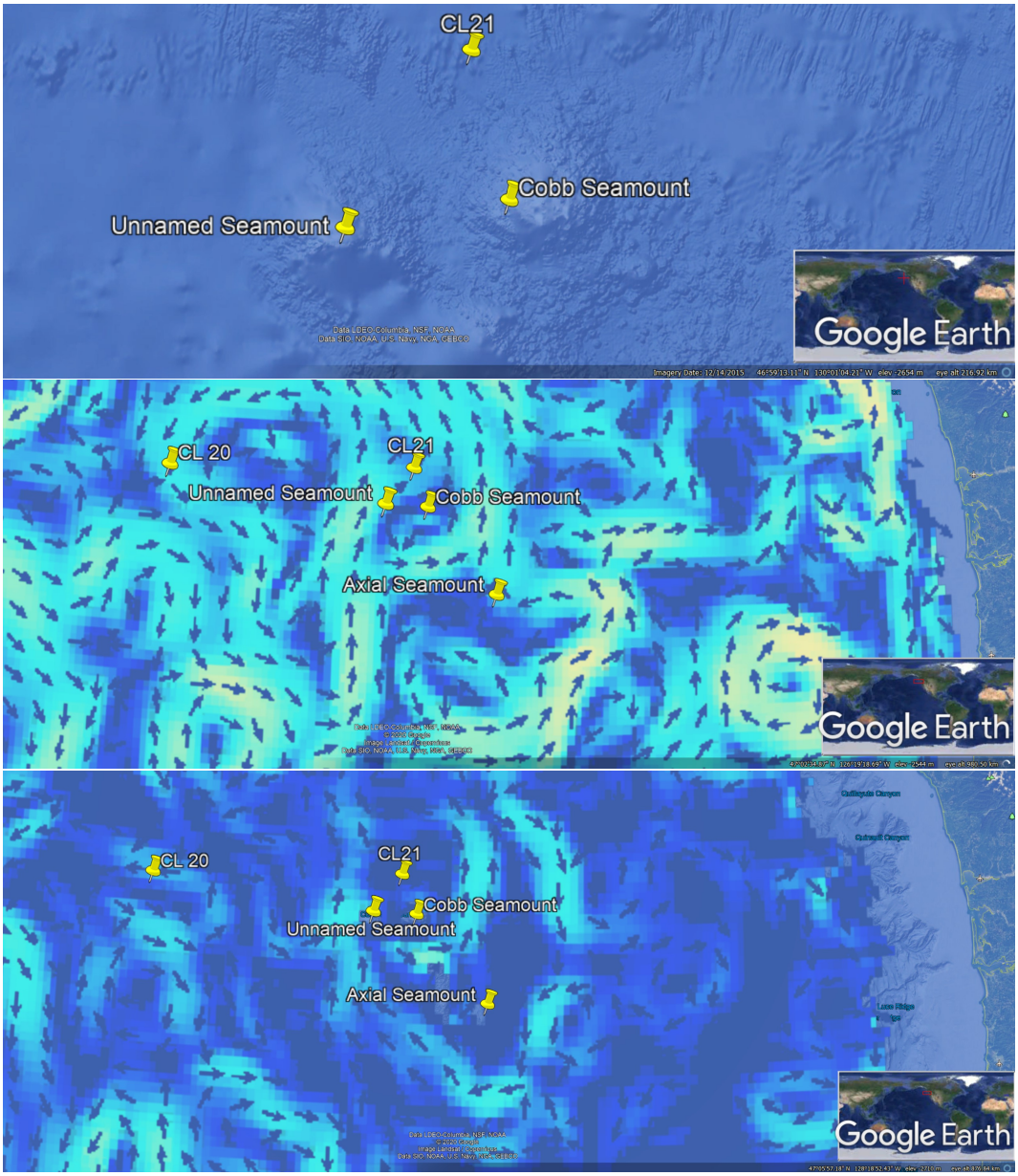

Figure 5.6.6: The top image shows the topography with two mayor seamounts near CL-21 based on the Google Earth underwater terrain model. The current model GLOBAL-ANALYSIS-FORECAST-PHY-001-024 (Copernicus Marine Service 2019) was used to create averaged water velocity layers for the month before the samples were taken near the sampling stations CL-21 and CL-20 in 100 m (middle image) and 1000 m (bottom image) depth. These were placed in Google Earth to georeference the locations of the two sampling stations, two relevant seamounts near CL-21 and the active underwater volcano Axial Seamount. Lighter colors indicate higher velocity, arrows show the direction of flow.

plutonium depth profiles at the sampling stations.

The Copernicus Marine Service provides a global model for oceanic currents based on local stations and satellite data (Copernicus Marine Service 2019). This model was used to calculate the monthly average water-flow in the month prior to sample extraction in 2017 in 100 m and 1000 m depth. The resulting velocity fields were laid over a Google Earth image of the region, so that the sampling stations and potentially relevant seamounts could be georeferenced. The middle image in figure 5.6.6 shows this overlay for 100 m depth, the bottom image for 1000 m depth. Such a general ocean model will be limited in its accuracy, and the velocity field changes drastically over time.

The main takeaway from this model is that some combination of the eastward currents in the North Pacific, the coastline and the fracture zones and seamounts placed before it result in complex, turbulent and changing currents near the sampling stations. At least some of the time water will flow over and around the two closest seamounts towards CL-21, and some vertical mixing and vertical advection might occur, resulting in a third factor that might influence the vertical distribution of plutonium at CL-21. Some increase in $^{239+240}$Pu activity near the seafloor can be observed in several samples in figures 5.6.3 and 5.6.4. This increase might be caused by remobilization from the sediment or could indicate a significant contribution of fast sinking large particles in the scavenging of the plutonium that reach the seafloor before the plutonium is released by degradation.

In conclusion the vertical distribution of ^{239}Pu and ^{240}Pu at CL-21 is atypical for open seawater. Local bathymetry, geology and the complex currents in the region provide potential explanations for this behavior. However, a single complete depth profile is clearly not sufficient to give a definitive answer to this question but demonstrates that this sampling area is a very interesting region for further investigations.

The total $^{239+240}$Pu activity in the water column at station CL-21 has been calculated as $67.1 \pm 3.1\,\mathrm{Bq/m^2}$ by interpolating the activities between the data points with straight lines and integrating the resulting function from 0 m to 3087 m. By adding (subtracting) the 1σ uncertainties from the data points, interpolating as above and integrating the resulting function the upper (lower) 1σ limit for the

inventory was calculated. Livingston calculated the half-residence time for plutonium for the West Pacific water column with a linear fit of inventories collected in the years 1973 to 1997 at 46.0±11.2 years (Livingston et al. 2001) which would correspond to a range of 124 Bq/m^2 to 220 Bq/m^2 in 1962. However, the extrapolation of this result for an additional 20 years without additional data to a location in the Northeastern Pacific with an unusual vertical distribution of ^{239}Pu and ^{240}Pu and a water column with half the depth of those used to determine this model can not be expected to be reliable even when the problem of lateral transport is ignored. Yamada determined an average decrease of (2.6±0.2)Bq $m^{-2}yr^{-1}$ per year based on two plutonium depth profiles from the central Bering Sea, compared to (0.89±0.07) Bq $m^{-2}yr^{-1}$ at the equator and (0.16±0.07)Bq $m^{-2}yr^{-1}$ in the South Pacific (Yamada et al. 2020) and attributes this large difference to the high biological productivity of the Bering Sea.

In figure 5.6.7 a collection of $^{239+240}Pu$ inventories for the 1973 GEOSECS stations from (Bowen et al. 1980) is shown. As the original data (black) was stated in the now outdated unit mCi/km^2 the corresponding values in Bq/m^2 were added for each data point (blue). To the right of the map the estimated global fallout inventories expected for 10° latitude bands are stated in mCi/km^2 (black) and Bq/m^2 (blue). Inside the red rectangle the location and inventory in 2017 for sampling station CL-21 was marked. The highest $^{239+240}Pu$ activity (92.5Bq/m^2-148.0Bq $m^{-2}yr^{-1}$) inventories in figure 5.6.7 are found east of Japan, in the areas influenced by the Kuroshio and its extension toward the North Pacific Current, as well as in the central North Pacific (96.2 Bq/m^2-122.1 Bq/m^2) in the area of the Subpolar Gyre. Based on the Livingston model, a $^{239+240}Pu$ inventory of $\approx$ 130Bq/m^2 would be estimated for CL-21 in 1973, while the Yamada Model would lead to an estimate of $\approx$ 180mBq/m^2. This large discrepancy between the models demonstrates the necessity of a local time series for a reliable model for the removal rate of plutonium in the Eastern North Pacific.

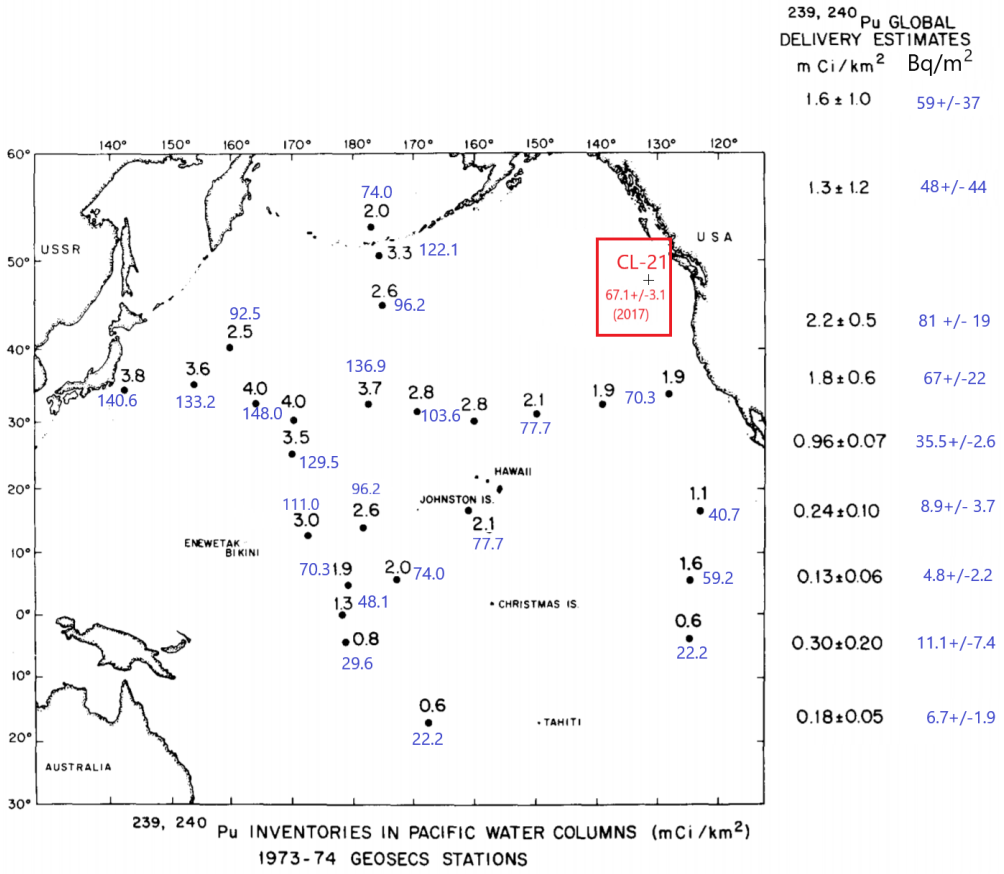

Figure 5.6.7: $^{239+240}$Pu inventories in the Pacific Ocean and global fallout delivery estimates depending on the latitude in mCi/km^2 (black) (Bowen et al. 1980). The corresponding values in Bq/m^2 (blue) as well as the CL-21 inventories in 2017 and 1973 estimated via extrapolation (red) were added to the original figure in Bq/m^2.

Figure 5.6.8 contains the isotopic ratios for all AMS samples shown in figure 5.6.2. The ^{240}Pu/^{239}Pu ratios for two surface water samples from the eastern North Pacific, taken 350 km north as well as 750 km and 1700 km east of station CL-20 from (Yamada et al. 2020) are also included in the figure.

The ^{240}Pu/^{239}Pu ratios for the Canada Basin and DYFAMED samples from (Lòpez Lora 2019) are all close to the global fallout ratio of 0.178±0.014 (Krey et al. 1976), while the ratios at CL-21 and CL-20 from this work, the Sagami Bay (Yamada et al. 2007) and the Bering Sea (Yamada et al. 2020) are elevated, indicating the influence of an additional source. All ^{240}Pu/^{239}Pu ratios measured in samples from

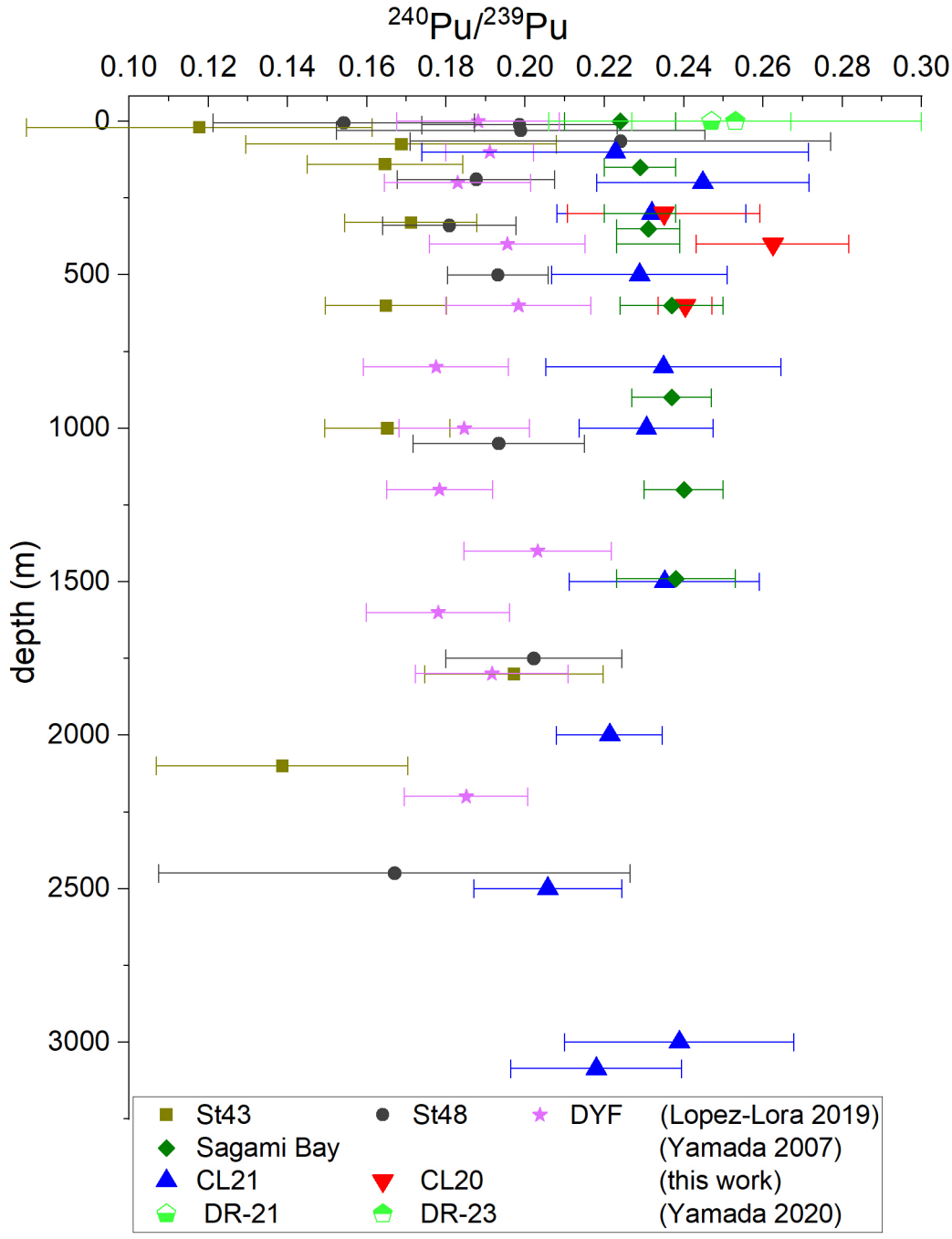

Figure 5.6.8: $^{240}Pu/^{239}Pu$ for stations CL-21, CL-20 as well as for the two stations from the Canada Basin and the DYFAMED station from (Lòpez Lora 2019) previously discussed. The two stations analyzed for the present work show consistently elevated $^{240}Pu/^{239}Pu$ ratios relative to these and are comparable to the samples from the western and central North Pacific (Yamada et al. 2007; Yamada et al. 2020).

sampling stations CL-21 and CL-20 are in the range of 0.211±0.019 to 0.253±0.010. These ratios are consistent with a combination of global fallout and tropospheric local fallout from the Pacific Proving Grounds. The $^{240}Pu/^{239}Pu$ ratios measured by Yamada in the Sagami Bay in the West Pacific as well as the Bering Sea are also compatible with those of CL-21 and CL-20. There is no indication of the presence of weapons-grade plutonium at either of the two stations from this work. The BD-17 0 m result with a blank corrected $^{240}Pu/^{239}Pu$ atom ratio of (0.08 ± 0.02) from (Hain et al. 2017) cannot be confirmed by the samples analyzed for this thesis. The BD-17 0m sample was measured in three different beamtimes, including one in the 5+ charge state to exclude the interference of $^{238}UH^{3+}$ (Steier et al. 2019) so a measurement problem is considered unlikely. Besides the isotopic ratio, the BD-17 0 m sample was also remarkable due to the very low concentrations of ^{239}Pu and ^{240}Pu at 0.32±0.05 mBq/m^3 and 0.09±0.02 mBq/m^3. The $^{239+240}Pu$ activity of all samples from the top 60 m of the water column of CL-21 and the surface water of CL-20 is lower than 0.3 mBq/m^3 as can be seen in figures 5.4.1 and 5.5.1. For the surface water the smaller size of the present samples of 5 l compared to the 20 l used for the BD 17 sample (Hain et al. 2017) proved challenging, and for three out of the four samples from this depth only an upper limit could be determined. In contrast, all profiles presented in (Lindahl et al. 2010) or the other sampling stations from (Hain et al. 2017) show a combined $^{239+240}Pu$ activity of several mBq/m^3 near the surface. Amongst 47 surface water samples taken in the mid-latitude region of the Pacific from longitudes 150E to 70W only three are below 1mBq/m^3 and only one of these is below 0.8mBq/m^3. All surface water samples from the Sea of Japan analyzed in (Lee et al. 2005) have combined $^{239+240}Pu$ activities of at least 3.5 ± 0.6 mBq/m^3. This extraordinarily low $^{239+240}Pu$ activity in surface water samples from the eastern North Pacific compared to samples from other regions in the Pacific indicates a comparably fast removal from surface water, which is likely connected with the unusual shape of the CL-21 depth profiles discussed above. However, for the BD-17 0 m sample this might also be an explanation for the low isotopic ratio measured as demonstrated by table 5.6.1 which shows the number of ^{239}Pu and ^{240}Pu atoms as well as the $^{240}Pu/^{239}Pu$ ratio for sample BD-17 and the corresponding blank before blank correction.

sample	^{239}Pu (10^6 at)	^{240}Pu (10^5 at)	^{240}Pu/^{239}Pu
BD17-0m	11.2±1.4	10.6±0.9	0.095±0.014
Blank-5E9	3.01±0.69	4.4±1.2	0.146±0.052

Table 5.6.1: ^{239}Pu, ^{240}Pu and ^{240}Pu /^{239}Pu for sample BD-17 and the corresponding blank before blank correction with 1σ uncertainties (Hain et al. 2017)

Sample BD-17 is close to the blank level. The large relative uncertainty of the isotopic ratio of the blank further complicates the situation, as with the large 1σ range of ≈0.1 to ≈0.2 the identification of the source is impossible. It would be compatible with global fallout, as well as with a combination of global fallout and natural ^{239}Pu or weapons-grade material. The ratio observed in the BD-17 sample could either be a statistical artifact or caused by a small contamination with a very low isotopic ratio. It is possible that either a ^{239}Pu spike or a sample from nuclear reactions experiments with a significant ^{239}Pu co-production was handled in the laboratory in Munich several years before the samples for (Hain et al. 2017) were prepared there. As the labware used for the sample was purchased for the Plutonium AMS project, a laboratory contamination entering the sample via dust particles in the air remains as a possible pathway. A similar dust-related background was recently observed in the laboratory at the DTU Denmark (Lin, Mu et al, manuscript in preparation). The concept of the chemistry blank can only account for a contamination in the reagents used for blanks and samples, while a small laboratory contamination that may reach individual samples would be inherently randomized. It is also possible that the ratio actually reflects that of the seawater at station BD-17. In this case the source must have been small and localized enough so that through diffusion and mixing the ^{240}Pu/^{239}Pu ratios at CL-20 and CL-21 five years later are not or no longer affected by it. As CL-21 is closer to the estuary of the Columbia River than BD-17 the hypothesis of emissions or remobilization of plutonium from the Hanford Site or its contaminated areas cannot be supported by the results of the present study.

6 Isotopic ratios of uranium in environmental samples

6.1 Blank levels for ^{233}U and ^{236}U

The ^{236}U and ^{233}U countrates for all four samples taken at CL-20 exceed their corresponding blanks by at least a factor of 6 as can be seen in figure 6.1.1 and table 8.0.1 in the appendix. The impact of the contaminations constituting the blank levels can be neglected for the ^{236}U/^{238}U and ^{233}U/^{236}U results of the four CL-20 samples.

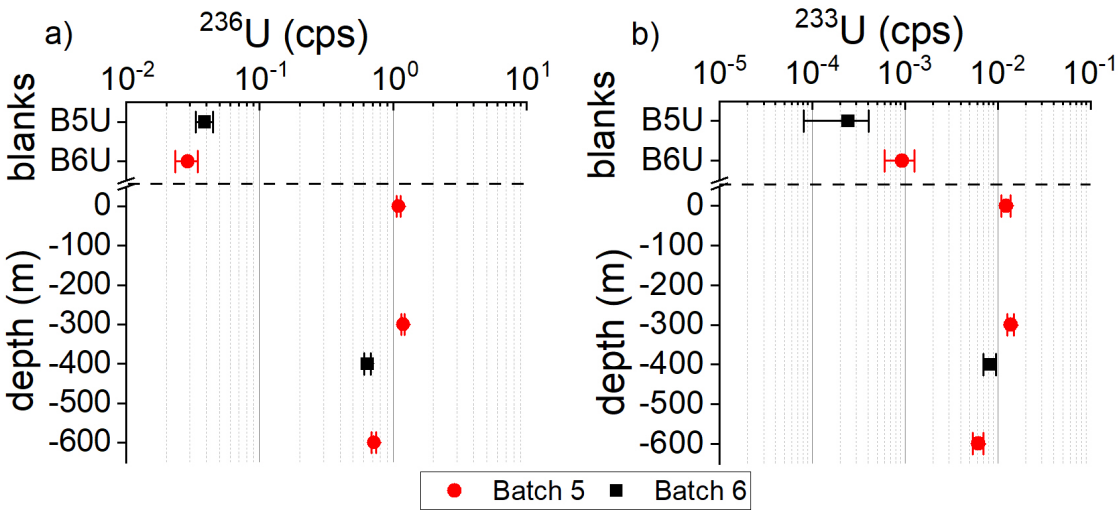

Figure 6.1.1: Plot a) shows the average ^{236}U countrates while plot b) shows the average ^{233}U countrates for all CL-20 samples in the form of a depth profile. Each chemistry batch is assigned a color and symbol according to the legend below the graphs. The corresponding blanks are plotted above the depth profiles as labeled.

Figure 6.1.2 shows the ^{236}U and ^{233}U countrates and blank levels for the samples from station CL-21. The data underlying figure 6.1.2 can be found in table 8.0.2 in the appendix. The ^{236}U countrates of all samples collected above 2000 m depth are considerably higher than those of their corresponding blanks, while the ^{236}U countrate for the sample from 2000 m depth exceeds that of the corresponding blank by a factor of 3.6. This is just above the threshold set for the qualitative blank correction in 4.4, so the proximity to the blank level should be considered when drawing conclusions from the ^{236}U/^{238}U ratio of this sample. The ^{236}U countrates for the 3000 m sample is very close to that of the corresponding blank, while those of the samples taken at 2500 m and 3087 m depth are below it, so only an upper limit can be derived and discussed. The high countrate on the 1000 m sample comparable to that at the surface is unexpected for this depth, and the sample will be discussed in more detail in chapter 6.2.

Due to the lower countrates and increased statistical uncertainty the ^{233}U blank levels require a detailed investigation. The ^{233}U countrates for the samples collected at 0 m, 60 m, 100 m and 1500 m depth are well above those of all blanks as can be seen in figure 6.1.2 b). countrates of the samples from 20 m, 200 m, 300 m, 500 m, 800 m and 3087 m are well above those of the corresponding blanks, while those at 2500 m and 3000 m are below it. The ^{233}U countrate of the sample from 1000 m and 2000 m depth exceed that of the corresponding blank only by a factor of 1.1 and 1.8 respectively. For the ^{233}U/^{236}U ratio both the ^{236}U and the ^{233}U countrate have to be considered. In conclusion the ^{236}U/^{238}U results for the samples from 2500 m, 3000 m and 3087 m and the ^{233}U/^{236}U results for the samples from 1000 m, 2000 m, 2500 m, 3000 m and 3087 m have to be considered heavily influenced by the contaminations constituting the corresponding blank levels.

Compared to the other samples, the results obtained for 1000m and 1500m are noteworthy: The ^{233}U count rate of $(6.70 \pm 0.74) \cdot 10^{-3}$ cps for the 1000 m sample is barely above that of the corresponding blank at $(5.85 \pm 0.76) \cdot 10^{-3}$ cps, yet has the highest ^{236}U countrate of all samples. In the case of the 1500 m sample the opposite is true: it has the overall highest ^{233}U count rate, whilst positioned in the lower half for ^{236}U. This indicates a potential problem with those two samples and therefore will be addressed in more detail in the following section.

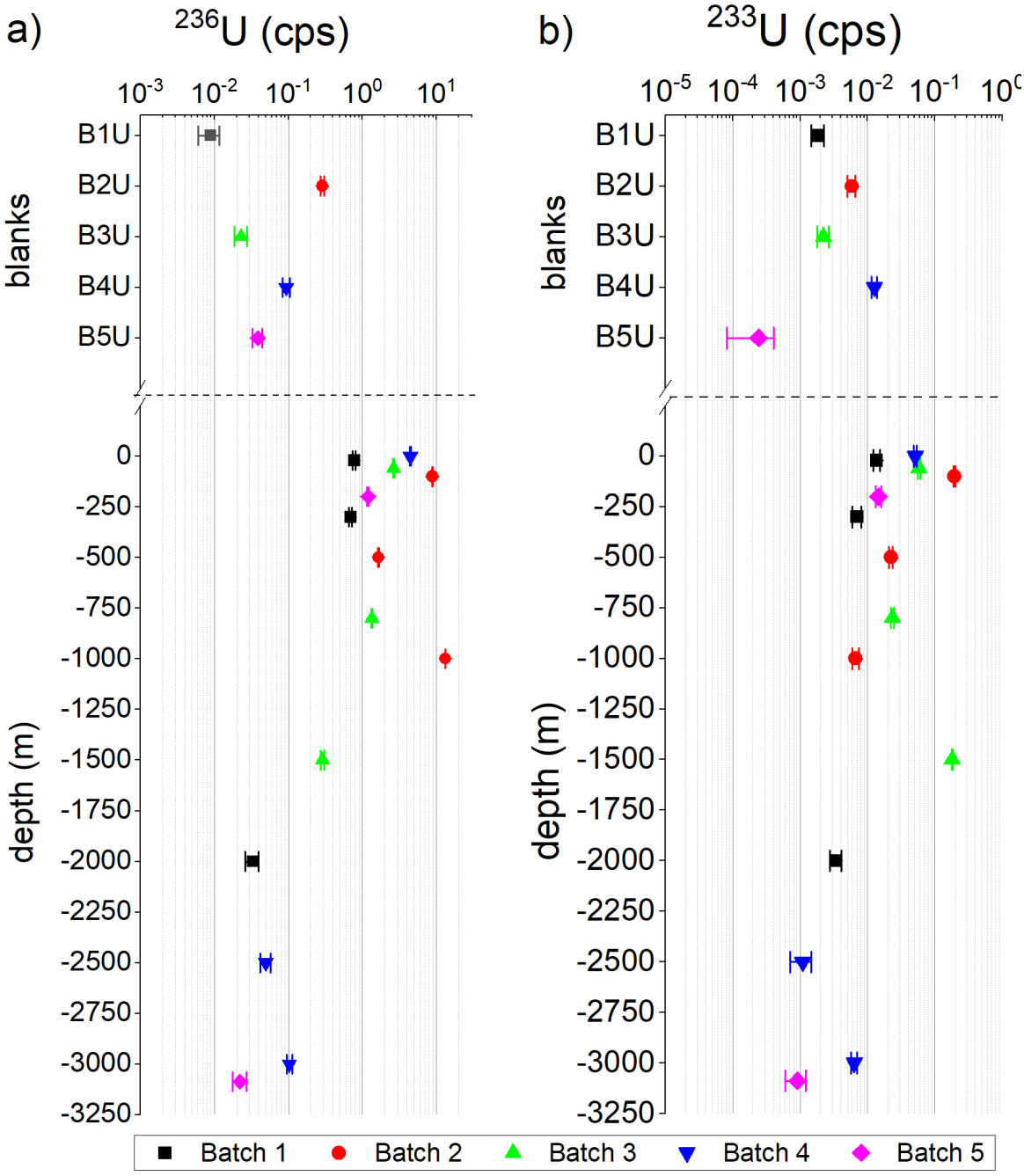

Figure 6.1.2: Plot a) shows the average ^{236}U countrates while plot b) shows the average ^{233}U countrates for all CL-21 samples in the form of a depth profile. Each chemistry batch is assigned a color according to the legend below the graphs. The corresponding blanks are plotted above the depth profiles as labeled.

6.2 Investigating the 1000 m and 1500 m results

The samples CL-21 1000 m and 1500 m stand out in figure 6.1.2 because they do not follow the same trend as other samples from comparable depths. This is especially problematic, as for each sample either the ^{233}U or ^{236}U countrate is conspicuous, but not the other. While it might be tempting to dismiss these two samples as outliers it is very hard to justify doing so.

The conservative chemical behavior of uranium in seawater generally leads to the expectation of a depth profile similar to those shown in figure 2.2.3 and a sharp increase in one specific depth is at odds with the diffusion model underlying the vertical distribution in the mentioned figure. While this is cause for suspicion, there simply is not sufficient data on the behavior of these uranium isotopes - especially ^{233}U - in the environment in general and the Northeast Pacific in particular to define a normal pattern these samples could deviate from.

For individual runs on a target, this problem can be resolved, as the remaining runs can serve as a benchmark for a single run with unexpected results. The first step with investigating unexpected results is therefore to compare the individual runs on a target and identify potential problems in those runs. A set of four plots shown in figure 6.2.1 for the ^{236}U/^{238}U measurements on sample CL-21 1000 m is routinely used to monitor the ^{238}U current, the countrate for the isotope of interest, their ratio and the ratio corrected using the detection efficiency for each turn (as explained in 4.2) of an actinide measurement both during the measurement and the subsequent data evaluation. The horizontal axis of these plots shows the wheel turn number, while the points are data for the individual runs. Should a target have two runs in one turn, two data-points are plotted at the same horizontal position. The overall increase in current and count rate over the duration of the measurement is typical for the extraction of UO^- from the Cs sputter ion source and not yet fully understood. Turn 25 is revealed as a clear outlier, so it is likely that something went wrong with either the ^{236}U or the ^{238}U measurements on CL-21 1000 m in this turn and consequently the data was discarded.

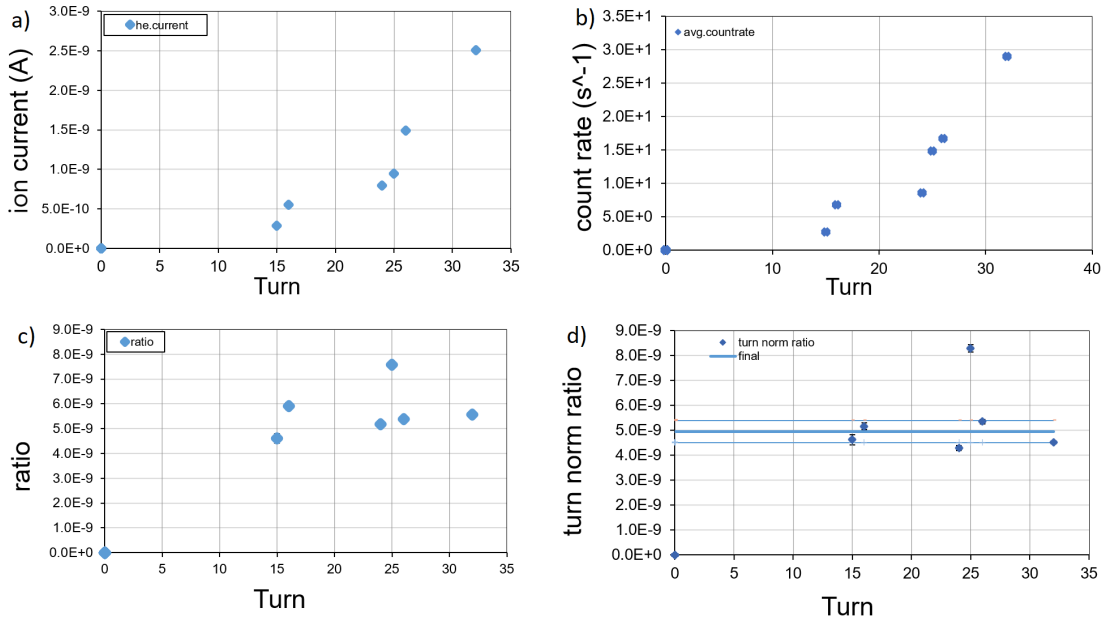

Figure 6.2.1: ^{238}U current a), ^{236}U countrate b) the ^{236}U/^{238}U ratio c) and the ^{236}U/^{238}U ratio after correction for the turn-by-turn detection efficiency d) in each turn for the CL-21 1000 m target. The positions of the turn 25 result in plots a) and b) are dissimilar, and it can be identified as an outlier in plot d). No other anomalies can be identified in these four plots.

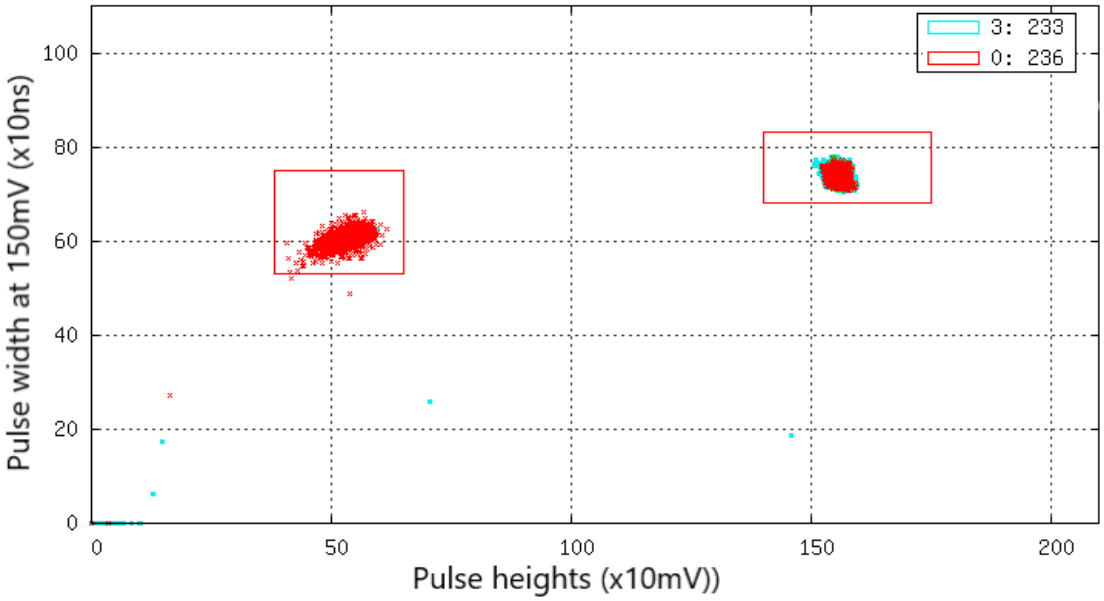

Figure 6.2.2: Pulse height vs. peak width diagram for turn 25 on CL-21 1000 m, showing the regions of interest (red rectangles) for trace ions (left) and of an electronic pulse generator used as time base (right) for the ^{233}U and ^{236}U measurements. The spectrum does not indicate any problems that could explain the deviating CL-21 1000 m result.

Problems with the detection of isotopes as events in the detector can sometimes be identified in the peak height vs peak width diagram introduced in 4.2.1. Typical problems would be events drifting outside the set regions of interest, or a large number of events outside the regions of interest in the spectrum. Should other events as introduced in figure 4.2.1 overlap with the trace ion region of interest, this might explain an increased countrate on mass 236. Figure 6.2.2 shows this plot for the CL-21 1000 m sample in turn 25 of the heavy/oct2019b beamtime. There are no indications for problems with the event measurements (only ^{233}U in light blue superimposed by ^{236}U in red are shown) visible in this graph.

Figure 6.2.3 shows fluctuations in the currents leaving the ion source during this run. Discontinuities that could be caused by small sparks in the ion source are recognized automatically and discarded as bad cycles. These are marked by the red vertical bars in the currents plot in figure 6.2.3. The gradual increase between the marked discontinuities is unproblematic, as the uranium measurement procedure utilizes fast sequencing to measure the $^{238}U^{16}O^-$ current in short intervals during the event collection periods for $^{233}U^{3+}$ and $^{236}U^{3+}$.

Neither the plot of currents in figure 6.2.3 nor the plot of events in figure 6.2.2 can explain the deviation in this measurement identified in figure 6.2.1 d). However, even discarding the CL-21 1000 m measurement in turn 25 of heavy/oct2019b as an outlier based on figure 6.2.1 d) only reduces the $^{236}U/^{238}U$ ratio from $(4.96 \pm 0.44) \cdot 10^{-9}$ to $(4.71 \pm 0.19) \cdot 10^{-9}$, which is still an order of magnitude higher than the samples above and below it in the depth profile. As no other irregularities can be identified in the data, it is not possible to resolve this issue with this approach. A contamination of this sample with ^{236}U would explain the result, which could be confirmed by re-measuring this sample. In this context, it is interesting to note, that the corresponding blank B2U has the highest ^{236}U countrate of all blanks as can be seen in figure 6.1.2. However, the ^{236}U countrate of CL-21 1000 m is almost two orders of magnitude above that of the blank, and an order of magnitude above where it would be expected by interpolating from the samples above and below it in the depth profile.

If a contamination is responsible, it is unlikely by a reagent used in all samples and the blank, and a residue on the surface of a utensil or contaminated dust particles

would be more plausible pathways for any excess ^{236}U in this sample. During the preparation of this batch heavy rain caused an intrusion of water through the exhaust onto the work bench, transporting dirt accumulated in the chimney to the working place and thus, onto the samples. While these were covered with watch glasses, some of this material with unknown composition might have entered the samples either directly or during the cleanup effort. A ^{236}U contamination in the exhaust could have gone unnoticed as long as the material carrying it either remained on the walls or was transported outside by the air current over time. A small amount of ^{236}U carrying material from the exhaust might have been swept into sample CL-21 1000 m on this occasion.

The CL-21 1500 m sample does not show any obvious irregularities in the turn-wise diagrams, the peak height versus peak width spectra or the current plots for the individual runs. The high ^{233}U countrate results in a ^{233}U/^{236}U ratio of $(0.599 \pm 0.069) \cdot 10^{-2}$ and hence is the highest ^{233}U/^{236}U value ever measured while (0.01-0.02)$\cdot 10^{-2}$ are observed in most samples. Also in projects besides the present work, an as of yet unidentified problem causes elevated ^{233}U results on a small number of sputter targets analyzed at VERA obtained from very different sample matrices. The CL-21 1500 m target was measured again in the heavy/jan2019c beamtime as part of a general investigation into this problem. While the ^{233}U/^{236}U ratio has dropped somewhat to $(0.351 \pm 0.096) \cdot 10^{-2}$ in this second measurement, it is still an order of magnitude higher than expected. This second measurement is included in the depth profile as a separate point for the same depth, as the two ratios are not compatible within the calculated uncertainties.

The large variation of the measurement results from different beamtimes indicates that this effect either depends on some parameter of the setup different in these beamtimes or does not affect all of the target material equally. A localized ^{233}U contamination - for example on the surface - would be reduced over time as it is destroyed by sputtering. Except for turn 25 the normalized ^{233}U/^{236}U ratio for this target decreases with increasing sputter time. In chapter 4.6 the role ^{232}ThH^{3+} molecules might play for the ^{233}U/^{236}U result of this sample was already addressed using this specific sample and excluded as an explanation due to the lack of a correlation with the ^{232}Th countrates. A third measurement of this sample in the

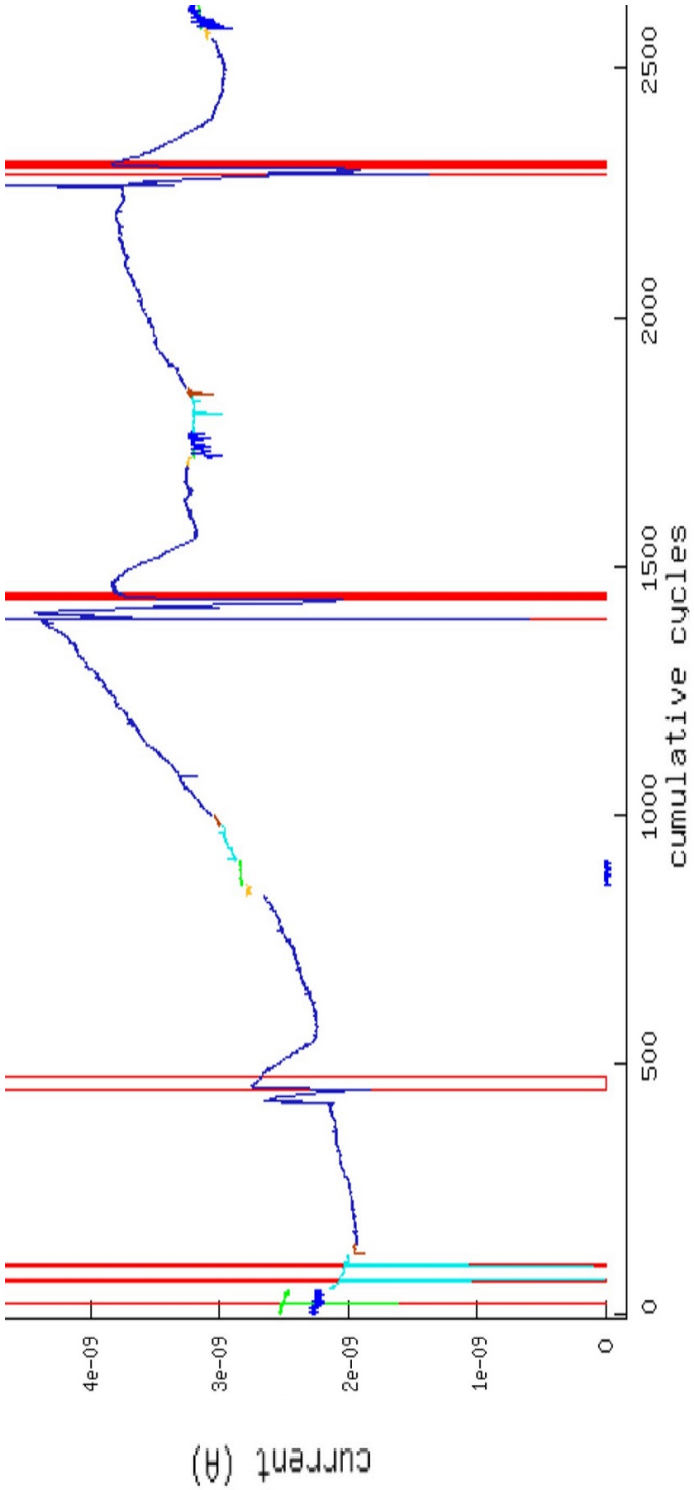

Figure 6.2.3: Negative ion current of mass 238+16 from sample CL-21 1000 m during turn 25, beamtime heavy/oct2019b measured in the Faraday cup between the ion source S1 and the first electrostatic analyzer. The color of the line indicates the mass selected for the detector in each cycle with 233 in blue and 236 in cyan. Short measurements on masses 239 (green) and 232 (brown) to monitor hydrides and 234 (yellow) to calculate ^{238}U from ^{234}U for targets with insufficient ^{238}U currents are also visible. The red rectangles indicate cycles automatically discarded due to discontinuities typically caused by sparks in the ion source. The mass 236 cycles not discarded are unremarkable, and the variations between the discontinuities do not affect the ^{236}U/^{238}U ratio due to the fast sequencing used for uranium measurements.

5+ state with oxygen stripping confirms the elevated ratio at $(0.40 \pm 0.14) \cdot 10^{-2}$. While the cause for this sporadic problem with some ^{233}U samples is still under investigation the CL-20 1500 m target is clearly affected by it. In this high charge state molecular isobars can be entirely discarded as the explanation, and it has to be assumed, that the high ratios are caused by an elevated ^{233}U concentration in this sample and others from different projects also affected by this phenomenon. Whilst not excluded altogether for the sake of completeness and documentation, the $^{233}U/^{236}U$ ratio of the 1500 m sample along with the $^{233}U/^{236}U$ and $^{236}U/^{238}U$ ratios of the1000 m sample will be marked red in the depth profile and has to be considered highly questionable when it comes to interpreting the depth profiles.

6.3 $^{236}U/^{238}U$ and $^{233}U/^{236}U$ at sampling station CL-21

The results for the $^{236}U/^{238}U$ and $^{233}U/^{236}U$ ratios at sampling station CL-21 are listed in table 6.3.1 and graphically presented as depth profiles in figure 6.3.1. Due to its conservative behavior, the residence time of uranium in seawater is estimated at $2.3 \cdot 10^5$ years in (Bloch 1980), so it is not surprising, that most of the anthropogenic uranium would still be found in the upper 1000 m of the water column. The samples at 2500 m, 3000 m and 3087 m depth were shown to have ^{236}U countrates comparable to or even below their process blanks, as were those at 2000 m, 2500 m and 3000 m for ^{233}U in 6.1.2. The samples where at least one of the countrates relevant is very close to or even below the corresponding blank are shown as empty squares in figure 6.3.1 and marked in table 6.3.1. All four of these show an elevated $^{233}U/^{236}U$ ratio. This may simply be due to the large statistical uncertainty of samples with a very low content of ^{233}U or ^{236}U in deep water samples. The total number of counts for each sample can be found in table 8.0.2 in the appendix. As the $^{233}U/^{236}U$ ratios of the blanks B1U and B4U relevant for the samples from 2000 m, 2500 m and 3000 m are both higher than 0.1 even a small influence of the contaminations constituting the blank levels for ^{233}U and ^{236}U could also explain the elevated $^{233}U/^{236}U$ ratios in these samples. These, along with the two samples at 1000 m and 1500 m depth already discussed above, were

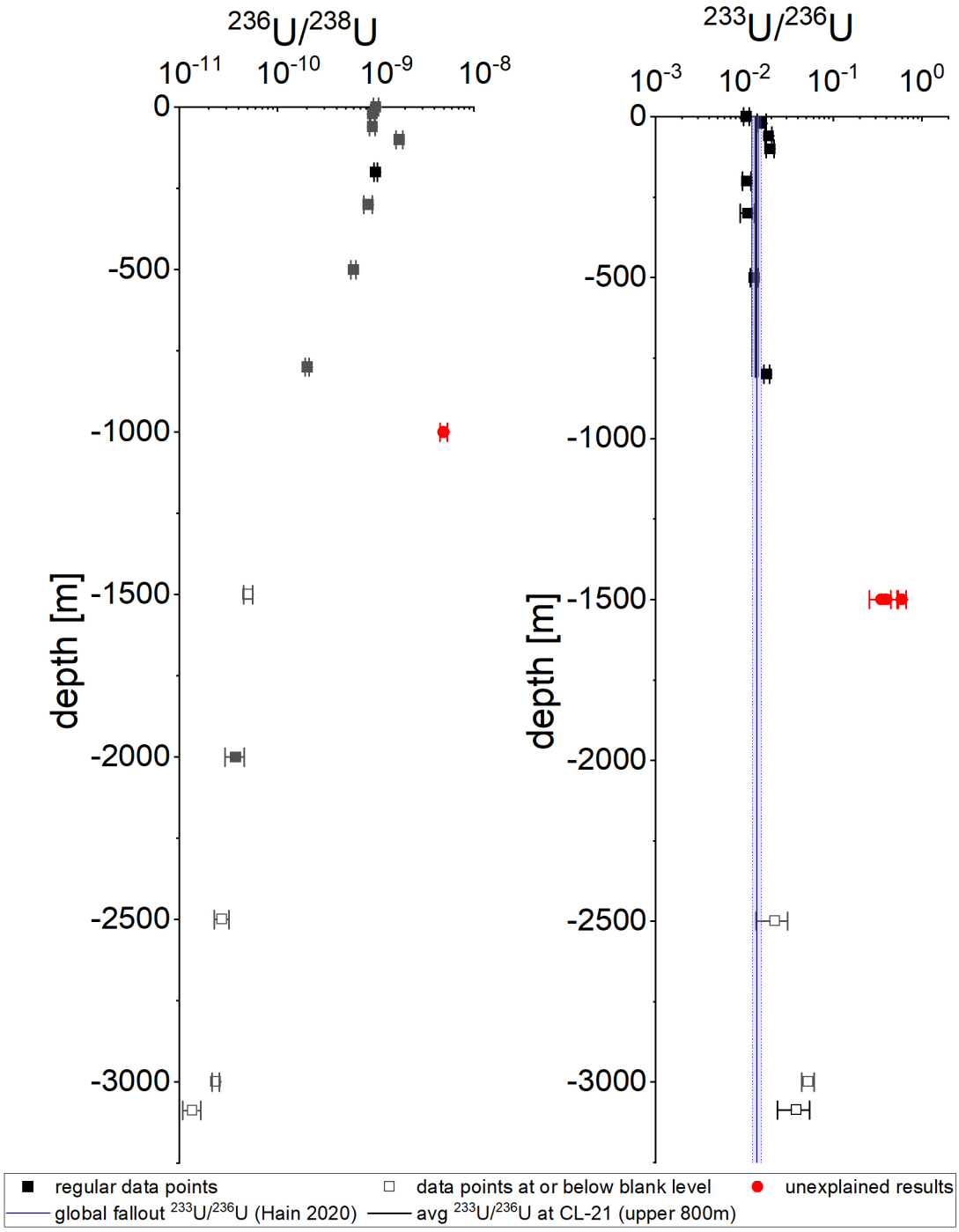

Figure 6.3.1: Vertical distribution of $^{236}U/^{238}U$ (left) and $^{233}U/^{236}U$ (right) atom ratios at CL-21. Red dots mark the samples showing irregularities as discussed above, and samples close to or below the blank level are represented by empty squares. The vertical blue line represents the estimated global fallout ratio for $^{233}U/^{236}U$ of (1.40±0.15)% (Hain et al. 2020) and the black line represents the average ratio calculated at (1.33 ± 0.13)% from the present results down to a depth of 800 m.

depth (m)	$^{236}U/^{238}U$ $(\cdot 10^{-10})$	$^{233}U/^{236}U$ $(\cdot 10^{-2})$
0	10.11 ± 0.56	1.058 ± 0.081
-20	9.32 ± 0.41	1.58 ± 0.19
-60	9.30 ± 0.62	1.88 ± 0.16
-100	17.5 ± 1.4	1.96 ± 0.20
-200	10.04 ± 0.36	1.07 ± 0.12
-300	8.47 ± 0.85	1.10 ± 0.20
-500	5.97 ± 0.34	1.29 ± 0.12
-800	2.015 ± 0.085	1.78 ± 0.13
-1000	49.6 ± 4.4 (**)	0.0490 ± 0.0072 (**)
-1500	0.505 ± 0.054	59.9 ± 6.9 35.1 ± 9.6 (**)
-2000	0.321 ± 0.065	8.8 ± 2.6 (*)
-2500	0.273 ± 0.046 (*)	2.23 ± 0.87 (*)
-3000	0.238 ± 0.020 (*)	5.25 ± 0.84 (*)
-3087	0.137 ± 0.029 (*)	3.9 ± 0.15 (*)

Table 6.3.1: $^{236}U/^{238}U$ and $^{233}U/^{236}U$ atom ratios at CL-21. (*) indicates samples close to or consistent with the blank level, and (**) marks the two samples discussed in 6.2.

left out of the calculation of the average $^{233}U/^{236}U$ ratio of $(1.37 \pm 0.14) \cdot 10^{-2}$ that consequently only represents the top 800 m of the water column, where reliable data could be obtained. In this depth range, the average $^{233}U/^{236}U$ ratio for CL-21 is compatible with the global fallout ratio of $(1.40 \pm 0.15) \cdot 10^{-2}$ (Hain et al. 2020). The two red dots for the 1500 m sample represent the two independent measurements of the $^{233}U/^{236}U$ ratio of that sample in separate beamtimes.

6.4 ^{236}U/^{238}U and ^{233}U/^{236}U at sampling station CL-20

The vertical distributions for ^{236}U/^{238}U and ^{233}U/^{236}U at station CL-20 are plotted in figure 6.4.1. The ^{236}U/^{238}U ratios show the expected decline with increasing depth. The results are listed in table 6.4.1 along with the corresponding ^{233}U/^{236}U ratios. The comparably large uncertainty of the sample CL-20 400 m is due to the lower number of ^{233}U and ^{236}U events. This is most likely caused by a low chemistry yield. For CL-20 0 m the external uncertainty is twice as large as the statistical uncertainty which can indicate a systematic error. An investigation as for CL-21 1000 m in 6.2 reveals an unusually large scatter in the ^{236}U/^{238}U ratios, but no apparent cause and no individual outlier. Unfortunately these samples were only measured in five turns, while CL-20 300 m was measured in eight and CL-20 600 m in seven turns due to some technical problems that reduced the length of the beamtime heavy/dec2019a. The average of the ^{233}U/^{236}U ratio lies within the 1σ uncertainties of three out of the four samples, and within the 2σ uncertainty for the fourth. The data is in good agreement with the hypothesis of a constant ratio defined by the weighted average of $(0.970 \pm 0.073) \cdot 10^{-2}$. This average ratio for CL-20 along with the standard deviation of the mean is included in in plot b) figure 6.4.1 as a black vertical line. The average ^{233}U/^{236}U ratio for the upper 800 m of CL-21 at $(1.37 \pm 0.14) \cdot 10^{-2}$ as well as the global fallout ratio of $(1.40 \pm 0.15) \cdot 10^{-2}$ (Hain et al. 2020) were included in the same plot. While the average for CL-21 is clearly consistent with the global fallout ratio, the ratio at CL-20 appears to be lower. A one-sided two-sample t-test with Welsh's correction for unequal variances based on the weighted means was conducted. The null hypothesis, the probability for the CL-21 mean being equal or smaller than the CL-20 mean has a probability of 0.023, so the difference of the ^{233}U/^{236}U ratios is not statistically significant using the 5σ standard. Based on the data available at present, the average ^{233}U/^{236}U ratio is consistent with the value for global fallout.

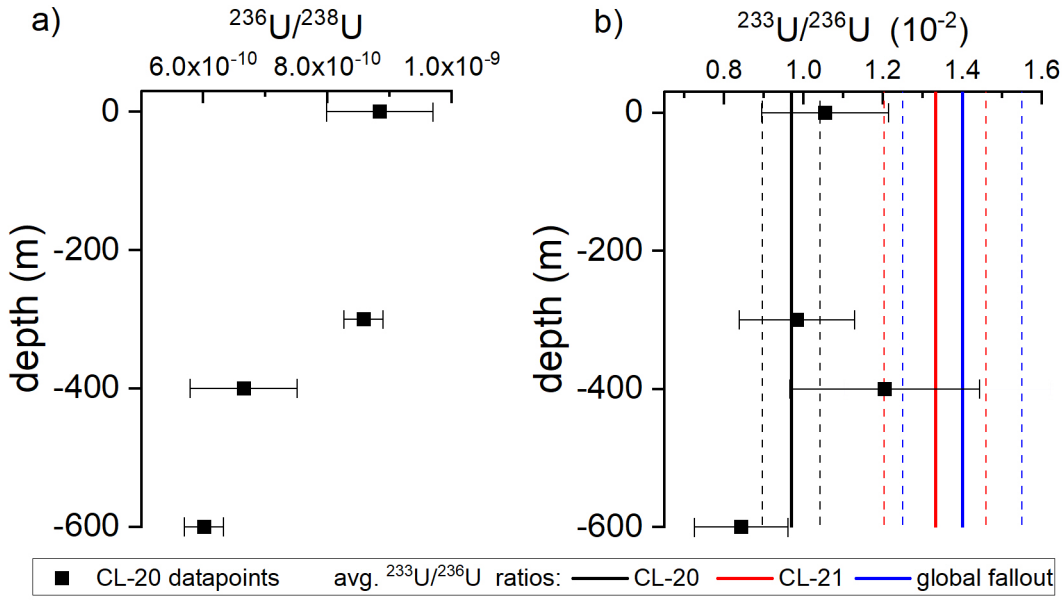

Figure 6.4.1: Depth profiles for $^{236}U/^{238}U$ (a) and $^{233}U/^{236}U$ (b) atom ratios at sampling station CL-20. In figure b) the vertical lines show weighted mean $^{233}U/^{236}U$ ratios with the dashed lines indicating the 1σ uncertainty for CL-20 at (0.970 ± 0.073) (black), CL-21 at $(1.33 \pm 0.13) \cdot 10^{-2}$ (red) and global fallout at $(1.40 \pm 0.15) \cdot 10^{-2}$ (blue) (Hain et al. 2020).

depth (m)	$^{236}U/^{238}U$ $(\cdot 10^{-10})$	$^{233}U/^{236}U$ $(\cdot 10^{-2})$
0	8.84 ± 0.86	1.06 ± 0.16
-300	8.58 ± 0.31	0.98 ± 0.15
-400	6.65 ± 0.89	1.21 ± 0.23
-600	6.01 ± 0.31	0.84 ± 0.12

Table 6.4.1: $^{236}U/^{238}U$ and $^{233}U/^{236}U$ atom ratios at CL 20

6.5 Interpretation of the uranium results

For comparison with the results on the behavior of uranium in the oceans from previous studies in the following the results of the present work are plotted alongside a selection of previously published depth profiles. Figure 6.5.1 combines two collections of $^{236}U/^{238}U$ depth profiles. Plot a) shows the uranium results from the same stations in the Canada Basin (St43 and St 48) and the Mediterranean Sea (DYF) from (Lòpez Lora 2019) already introduced in 5.3, the CR58 sample from the Japan Sea published in (Sakaguchi et al. 2012) as well as samples St1 and St11 from the South Pacific from (Villa-Alfageme et al. 2019). Plot b) contains the BD7-BD15 samples from the Subarctic Current in the North Pacific and the TR4, TR13 samples from the Kuroshio Extension published in (Eigl et al. 2017) in addition to the CL-21 and CL-20 results from this work. The samples used for the first $^{236}U/^{238}U$ depth profile in the northeast Pacific Ocean (Eigl et al. 2016) were taken at the same BD-17 sampling station as the BD-17 0 m sample discussed in the plutonium part of this work. This depth profile is included in figure 6.5.1 b) as well. See figure 6.5.3 for an overview of the locations of the Pacific Ocean samples. As most of the anthropogenic entry of uranium is expected in the upper layers of the water column, a more detailed view of this part helps to distinguish the different profiles. Figure 6.5.2 shows the upper 2000 m for both depth profiles from figure 6.5.1, as below this depth the results of this study are unreliable due to the closeness to the blank level. In figure 6.5.1 the ratios of the CL-21 samples from 2500 m to 3087 m depth are marked as empty triangles due to the closeness to the blank level, as is the sample from 1000 m depth due to the issues discussed in 6.2

Most $^{236}U/^{238}U$ ratios shown in figures 6.5.1 and 6.5.2 decline with depth after a shallow water maximum between 50 m to 200 m. Going from highest to lowest surface concentration the $^{236}U/^{238}U$ ratios from the Subpolar Gyre exceed those from all others for the upper 1000 m and show the expected continuous decrease down from a range of $(0.7 - 1.4)\cdot10^{-8}$ near the surface to a minimum of $\approx 10^{-10}$ in a depth of 2000 m - 4000 m depending on the profile. This is followed by an increase by a factor of 2-4 in the abyssal water (Eigl et al. 2017). According to Eigl, this minimum zone corresponds to the very old pacific deep water, while the

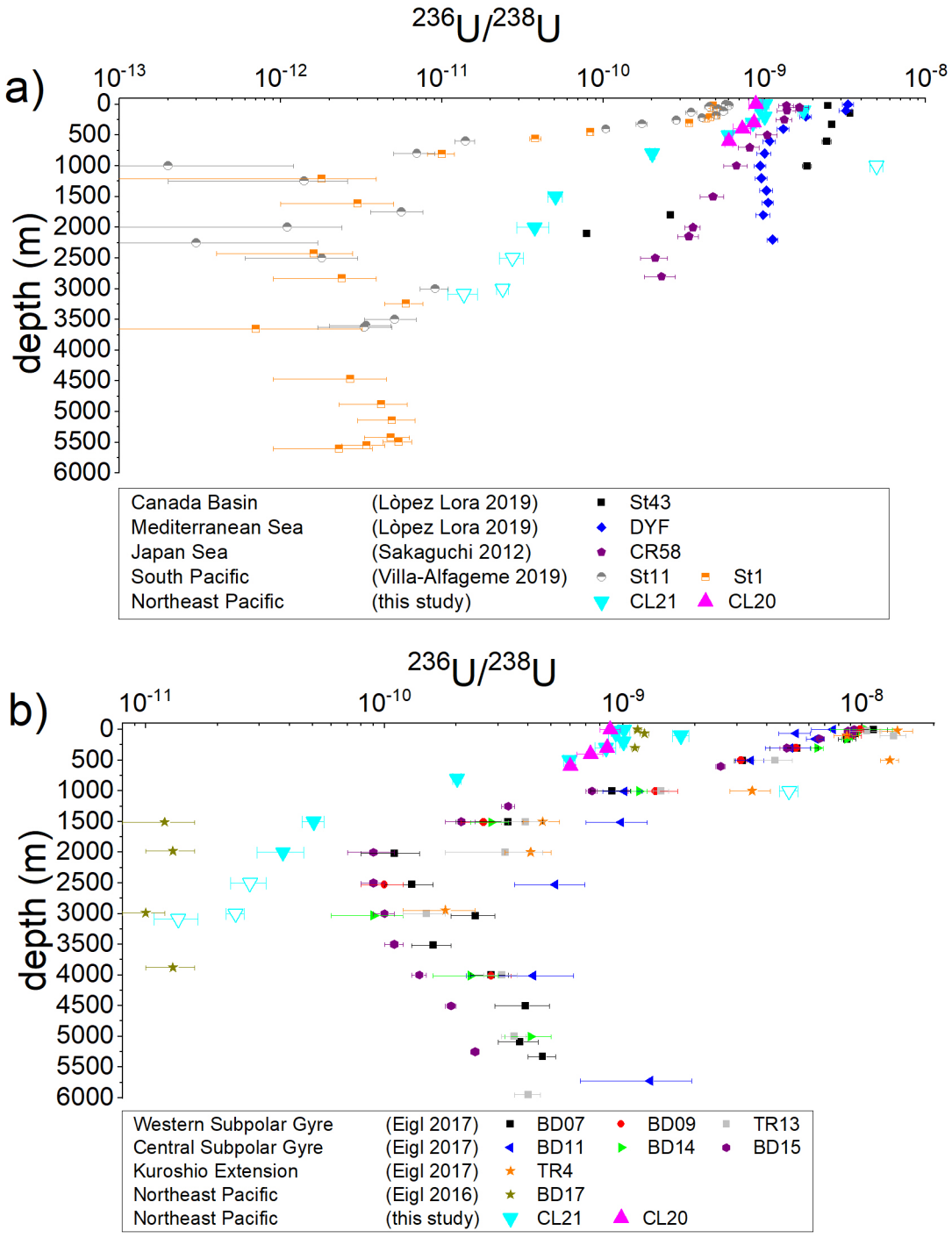

Figure 6.5.1: Plot a) shows depth profiles from the Canada Basin (St43), the Mediterranean (DYF) and the Japan Sea (CR 58) and the South Pacific (St1, St 11) alongside CL-21 and CL-20, while Plot b) contains samples from along the Subarctic Current (BD7-BD17, TR13) and the Kuroshio Extension (TR 4). Empty symbols represent non-reliable results from the present study.

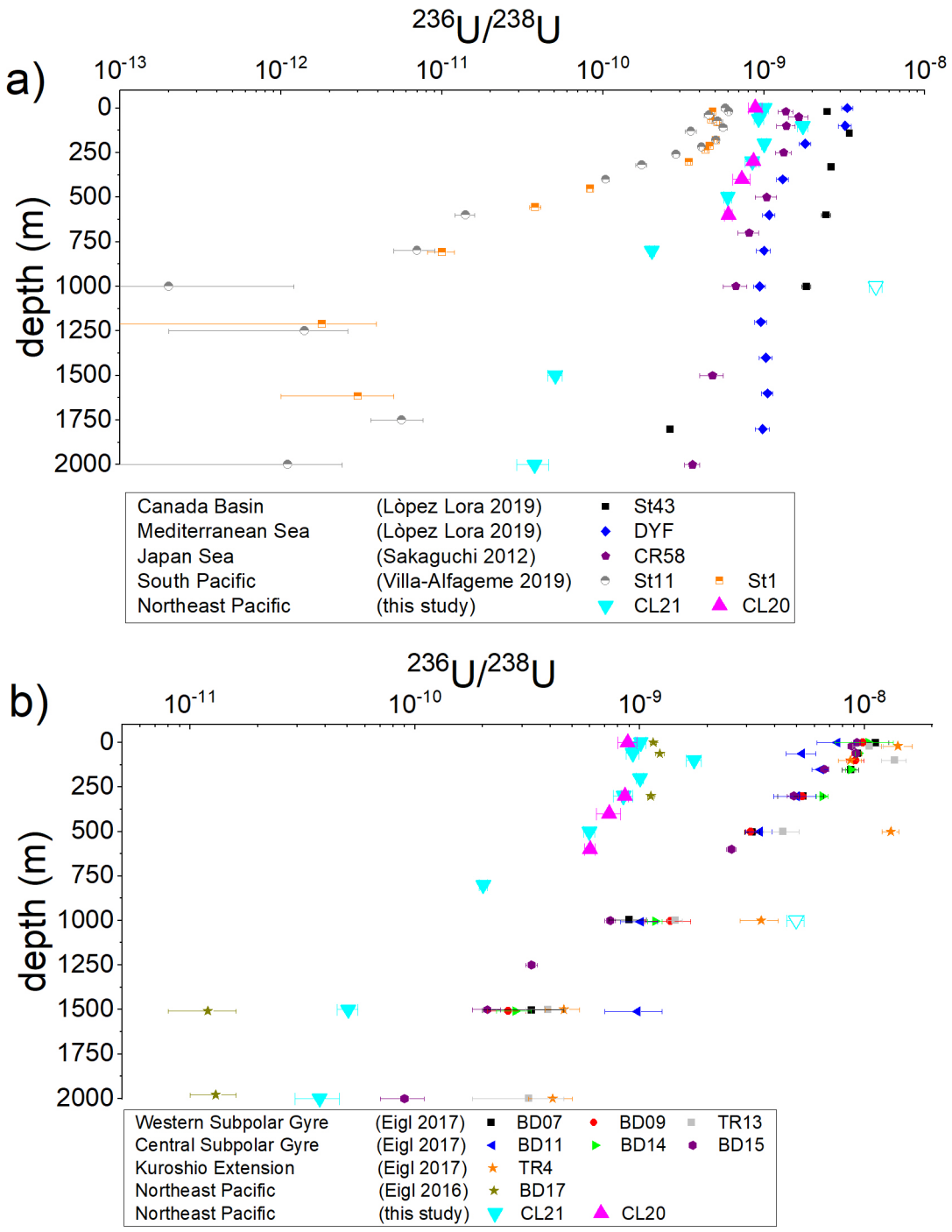

Figure 6.5.2: Zoom on the upper 1500 m of the depth profiles from figure 6.5.1. The highest $^{236}U/^{238}U$ ratios are found in the western and central North Pacific in the Subpolar Gyre, followed by the Canada Basin, the Mediterranean and the Japan Sea. The $^{236}U/^{238}U$ ratio at CL-21, CL-20 and BD-17 from the Northeastern Pacific are consistently lower than all the above mentioned. Only the samples from the South Pacific are even lower.

abyssal layer with the increased ratios is identified as the much younger LCDW introduced in 3.1.3. The ratios of the stations in the western and central part of the Subpolar Gyre are similar which is to be expected, as they are all positioned on or close to the Subarctic Current. Global fallout and tropospheric fallout from the Pacific Proving Grounds transported north by advection are identified as the main sources of ^{236}U in this region by Eigl (Eigl et al. 2017). The TR4 station from the Kuroshio extension has the overall highest ^{236}U/^{238}U ratios.

The depth profile at St43 in the Canada Basin has a maximum in 140 m depth at $(3.40\pm0.15) \cdot 10^{-9}$. Otherwise it remains in the range of $(1.84 \pm 0.12) \cdot 10^{-9}$ to $(2.62 \pm 0.13) \cdot 10^{-9}$ between 15 m and 1000 m depth, followed by a decline towards $(7.88 \pm 0.29) \cdot 10^{-11}$ in 2100 m depth. This depth range of increased ^{236}U/^{238}U ratios coincides with water masses originating in the Atlantic Ocean wedged between a thin layer of Pacific water in the upper 5-20m and the older bottom water below 1000 m. Consequently, the layer of elevated ^{236}U/^{238}U ratios at St43 is ascribed to emissions from the reprocessing plants La Hague and Sellafield into the Atlantic Ocean (Lòpez Lora 2019). The shape of the DYFAMED profile is ascribed by López Lora to a ^{236}U input from the Marcoule reprocessing facility around the time of sampling in 2001 after the previous inputs had been essentially homogenized. This results in a ^{236}U/^{238}U ratio of 3.30 ± 0.26 near the surface followed by a decline to 1.00 ± 0.30 below 330 m depth.

The ^{236}U/^{238}U ratios at CR58 decrease from $(1.65 \pm 0.23) \cdot 10^{-9}$ in 50 m depth to $(2.3 \pm 0.5) \cdot 10^{-11}$ in 2803 m. The ^{236}U concentrations for this station were already shown in 2.2.3 and the depth profile is in good agreement with diffusion models (Sakaguchi et al. 2012).

The BD-17 ^{236}U/^{238}U ratios in the upper 300 m of the water column are all in the range of $(1.12 \pm 0.037) \cdot 10^{-9}$ to $(1.23 \pm 0.054) \cdot 10^{-9}$ whereas those below 1500 m range from $(1.0 \pm 0.02) \cdot 10^{-11}$ to $(1.3 \pm 0.03) \cdot 10^{-11}$. The two groups are separated by two orders of magnitude while the intermediary 600 m and 1500 m samples were lost (Eigl et al. 2016). The low ratios in the deep water have been attributed to the old Pacific Deep Water and the conservative behavior of uranium in seawater.

The samples from the South Pacific shown in figures 6.5.1 and 6.5.2 have the lowest ^{236}U/^{238}U ratios at all depths. This is both plausible as the majority of

nuclear weapons tests were conducted on the northern hemisphere and consistent with recent AMS measurements for surface soils from Chile and Africa reporting ^{236}U concentrations at least two orders below those typical for the northern hemisphere (Salmani-Ghabeshi et al. 2018). However, this is offset to some extent due to the transport of fallout ^{236}U from the North Pacific and the ^{236}U/^{238}U ratios from this region shown in figures 6.5.1 and 6.5.2 are much closer to those from the Northeastern Pacific in the upper 500 m of the water column. The ^{236}U/^{238}U ratios of these samples also show a very rapid decline from a range of $(2\text{-}5) \cdot 10^{-10}$ in the upper 300 m of the water column to less than $9.1 \cdot 10^{-12}$ for all depth below 1000 m. The overall minimum again corresponds to the very old Pacific Deep Water, followed by a slight rise below 3000 m attributed to the much younger LCDW (Villa-Alfageme et al. 2019). Only global fallout is identified as a significant source of ^{236}U in this region in this study and the ratios measured in the depth range of the Pacific Deep Water are the lowest ^{236}U/^{238}U ratios in seawater published to date, approaching the estimate for natural isotopic ratios of 10^{-13} by (Steier et al. 2008).

Neglecting the already discussed CL-21 1000 m sample, the CL-21 and CL-20 depth profiles for ^{236}U/^{238}U show the typical diffusion shape expected in 2.2.3 caused by a surface deposition of anthropogenic uranium, with a narrow subsurface maximum at 100 m depth for CL-21 and a general decline with depth. The depth profiles from the two sampling stations are compatible within the uncertainties in the upper 600 m of the water column where samples from CL-20 were available. The ^{236}U/^{238}U ratios of both are up to an order of magnitude below those from the Subpolar Gyre. This would indicate that the two sampling stations from the present study are not directly influenced by the Subarctic Current or the North Pacific Current feeding it. If the sampling stations are off the main branches of these currents, a reduced influence of the PPG tropospheric and close in fallout material transported in these currents would be expected.

The ^{236}U/^{238}U ratios at the DYFAMED and CR58 stations lie above those of the samples at CL-21 and CL-20, except for the CL-21 100 m sample with a ratio slightly higher than that of the corresponding CR58 sample. While very close to the CR58 ratios near the surface, those at CL-21 decrease much faster and are an

order of magnitude lower in 2000 m. The ratios in samples from the top 300 m of BD-17 are very close to those found at CL-21 and CL-20 in this study, while those at 1500 m and 2000 m depth are below the corresponding CL-21 ratios by a factor of 3 and 4 respectively. A rapid decline in the intermediary depth range similar to that of the CL-21 ratios must occur at BD-17, even if its exact shape could not be determined between 500 m and 1000 m. A similar rapid decrease followed by stabilization or an increase in abyssal waters in the other depth profiles from the Pacific Ocean shown in figures 6.5.1 and 6.5.2 is explained by the very old Pacific Deep Water and the younger LCDW below it as discussed above. Dissolved oxygen has a minimum near 1000 m depth at the two sampling stations from this study as shown in 3.1.2 and at the BD-17 station (Eigl et al. 2016). The rising oxygen concentration below indicates the influence of a younger water mass near the bottom. Likely candidates are either LCDW or the product of local subduction connected to the complex bathymetry in the sampling region discussed in the plutonium chapter. The rate of decrease for the CL-21 ratios appears to slow down in this depth range, compared to the upper 1000 m. Unfortunately, the very low ^{236}U count rates too close or even below the corresponding blanks measured for the samples taken below 2000 m depth did not allow for the reliable determination of the ^{236}U/^{238}U ratios for these depths. Therefore this observation is based almost entirely on the concentration of the CL-21 2000 m sample and could also be explained by a statistical artifact. The ^{236}U/^{238}U ratios of the four BD-17 samples in the depth range from 1500 m to 3878 m remain almost constant. Whilst an increase of this ratio in abyssal waters similar to that of the Subpolar Gyre samples could not be observed, the ^{236}U/^{238}U ratios of these BD-17 samples stabilize two orders of magnitude above the estimate for the natural ^{236}U/^{238}U ratio of $\approx 10^{-13}$ from (Steier et al. 2008) whereas a further decline would be expected for the diffusion of a conservative trace isotope in an otherwise homogeneous water mass.

The two maps in figure 6.5.3 showing the major currents in the North Pacific raise the question of whether the sampling stations CL-21 and CL-20 marked in both maps are directly influenced by the North Pacific Current or the Subarctic Current. The turbulent flow calculated by the Copernikus Marine Service model

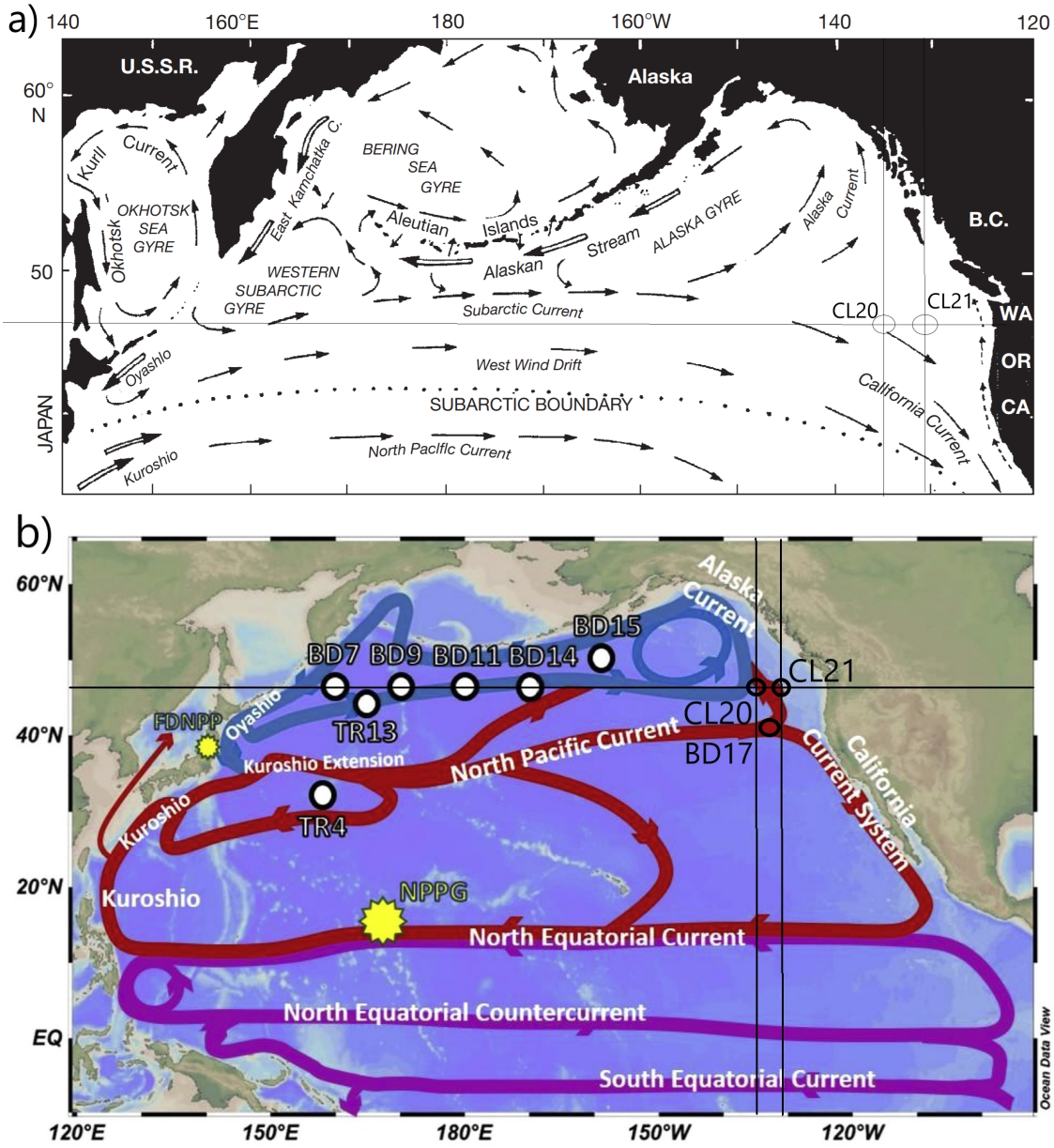

Figure 6.5.3: The upper map a) shows the major wind-driven currents in the North Pacific according to (Hickey et al. 2019) while the map b) from (Eigl et al. 2017) below shows a slightly different current model as well the locations of the BD7 - BD15 sampling stations. Based on a similar map in (Eigl et al. 2016) the location of station BD17 was marked on this map, as were those of CL-21 and CL-20 on both maps.

for the sampling region shown in 5.6.6 indicates that the stations lie off the main arms of these two currents. This is reinforced by the $^{236}U/^{238}U$ ratios found in samples from the present study which are an order of magnitude below those of the TR13 and BD07-BD15 samples for most depths as shown in figures 6.5.1 and 6.5.2 and discussed above. If the map on the right is correct and the North Pacific Current is the main current near the sampling stations, then a significant dilution appears to take place along the way between the Kuroshio Extension with sampling station TR4 and the sampling region for the present study. As TR4 has the highest $^{236}U/^{238}U$ ratios of all depth profiles shown in figures 6.5.1 and 6.5.2, it is unlikely that the North Pacific Current feeding the Subpolar Gyre would provide such a dilution for the Subarctic Current between BD15 and the stations CL-21 and CL-20. The most plausible explanation then is that these two sampling stations and BD-17 are not directly influenced by either current system. Consequently, the ^{236}U from the PPG accumulates there at a much slower rate through diffusion and limited water mass exchange with the two major currents transporting it eastward splitting into the Alaska Current and the California Current west of the sampling region. This explanation would also be in agreement with the complex flow calculated by the Copernikus Marine Service model for the sampling region.

The CL-21 and partial CL-20 $^{233}U/^{236}U$ depth profiles shown in figure 6.5.4 are the first ever obtained for a ocean water column. In (Hain et al. 2020) two surface water samples from the Irish Sea and the Kattegat in the Danish Straits were published. The $^{233}U/^{236}U$ ratios of these two water samples were plotted together with the global fallout ratio published in the same article and the two depth profiles from the present work in figure 6.5.4. Only the upper 800 m of the water column are shown, as the $^{233}U/^{236}U$ results below this depth cannot be considered as reliable. The Irish Sea sample and the two Kattegat samples have $^{233}U/^{236}U$ ratios of $(0.11 \pm 0.01) \cdot 10^{-2}$, $(0.45 \pm 0.02) \cdot 10^{-2}$ and $(0.44 \pm 0.04) \cdot 10^{-2}$. These locations are influenced by the nuclear processing plants of Sellafield and La Hague, which is well documented for the Irish Sea and evidenced by the elevated $^{236}U/^{238}U$ ratios of $(1.34 \pm 0.02) \cdot 10^{-8}$ and $(1.18 \pm 0.03) \cdot 10^{-8}$ for the two Kattegat samples (Hain et al. 2020). The average $^{233}U/^{236}U$ ratios for CL-21 and CL-20 are compatible with each other and the global fallout ratio of $(1.40 \pm 0.15) \cdot 10^{-2}$. While the $^{233}U/^{236}U$

ratios of the Irish Sea and Kattegat samples can be clearly distinguished from those at CL-21 and CL-20, the large uncertainties mainly caused by the low amount of ^{233}U counts detected and the small number of samples especially at CL-20 limit the ability to identify smaller differences. Two potential local sources of ^{233}U were identified in a literature search, the Hanford Site where about 2 tons of ^{233}U were produced (Alvarez 2013) and small amounts of ^{232}Th were added to fuel elements to influence the neutron flux (Zachara et al. 2007) and fallout from the detonation of a 22kT ^{233}U/^{239}Pu device at the Nevada Test Site during Operation Teapot (Hansen et al. 2007)). There is no indication for additional ^{233}U sources influencing the two sampling stations analyzed in the present work, so neither of these potential sources had a significant influence on the ^{233}U/^{236}U ratio in the sampling region. The ^{233}U/^{236}U results of the present study support the hypothesis of large thermonuclear weapons tests as the main source for ^{233}U in the Pacific Ocean stated in (Hain et al. 2020).

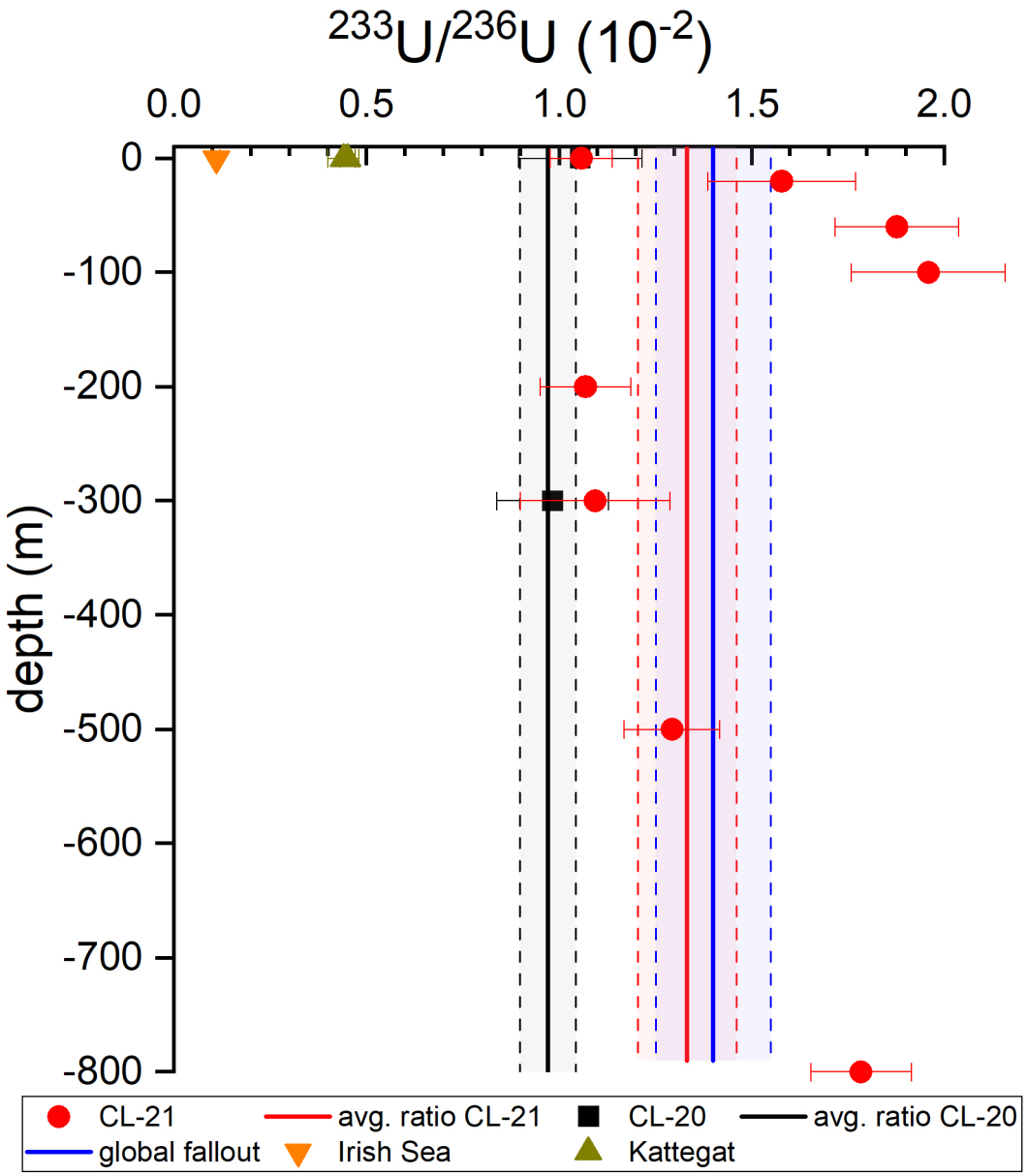

Figure 6.5.4: The first two seawater $^{233}U/^{236}U$ depth profiles along with two $^{233}U/^{236}U$ seawater samples and the global fallout ratio from (Hain et al. 2020)

7 Summary and Outlook

In this work, two depth profiles from the Northeast Pacific were analyzed with respect to their ^{239,240}Pu concentration to answer the question of the presence of weapons-grade plutonium which has been indicated by a previous study (Hain et al. 2017). This finding could not be confirmed and is most likely a statistical artifact due to the extraordinarily low plutonium concentrations in surface waters of this region. The ^{240}Pu/^{239}Pu ratios at both sampling stations show no significant change with depth. The average ^{240}Pu/^{239}Pu ratio at CL-21 is 0.2292±0.0030 while that at CL-20 is 0.2423 ± 0.0049. Both average ratios are compatible with a combination of global fallout with an isotopic ratio of 0.178 ± 0.014 (Krey et al. 1976) and tropospheric fallout from the Pacific Proving Grounds.

Due to the wide range of isotopic ratios from the PPG of 0.24 to 0.34 (Buesseler 1997), the estimate for its contribution to the plutonium in the water column at station CL-21 using equation 2.1.1 spans from 31% to 82%. It is remarkable, that the particle reactive plutonium from the PPG plays such a significant role even in the Northeast Pacific.

The shape of the plutonium depth profile at CL-21 is highly unusual. Instead of the subsurface maximum expected it exhibits an almost constant concentration starting from a depth of 800 m. Though beyond the scope of a typical physics thesis, a thorough literature research on geology, bathymetry and bioactivity was performed, leading to a first tentative interpretation of the results. The influence of these factors and of the interaction of diverging major current systems on the vertical distribution of plutonium in the eastern North Pacific can certainly not be resolved with only one full depth profile.

However, it is clear that local effects play a significant role in this region for the vertical transport of plutonium in the water column. An investigation involving

additional samples taken by a later cruise or collected close-by and ideally a separate analysis of suspended particles at different depths might help shed light on this matter.

Additionally, in order to use the precious sample material most efficiently, the pair of ^{236}U and ^{233}U was analyzed. The ^{233}U/^{236}U ratio has been suggested recently for emission source identification (Hain et al. 2020). A full ^{236}U/^{238}U depth profile for sampling station CL-21 and a partial depth profile for CL-20 (only four samples down to 600 m depth were available) were obtained. Furthermore, the first two ^{233}U/^{236}U depth profiles for ocean water columns are presented. For CL-20 this is again limited to the upper 600 m due to the lack of samples below this depth. At CL-21 reliable results could only be obtained for the upper 800 m of the water column. From 2000 m depth downward either the ^{233}U or the ^{236}U countrates were close to or even below the blank level.

The ^{236}U/^{238}U and ^{233}U/^{236}U depth profiles show that while ^{238}U is in equilibrium and distributed almost uniformly throughout the water column, the two anthropogenic isotopes are still found primarily in the upper layer of the water column. The vertical distribution of ^{236}U/^{238}U and ^{233}U/^{236}U in the upper layers of CL-21 and CL-20 is consistent with diffusion after surface deposition, while the very old Pacific Deep Water indicated by the minimum in dissolved oxygen between 500 m and 1500 m depth could explain the very rapid decline of the ^{236}U/^{238}U ratio in this depth range. The ^{233}U/^{236}U ratios remain constant within the uncertainties for all depths where reliable results could be obtained, and the difference between the two sampling stations is not statistically significant. The average ^{233}U/^{236}U ratios of $(1.37\pm0.14)\cdot10^{-2}$ at CL-21 and $(0.970\pm0.073)\cdot10^{-2}$ CL-20 are compatible with the global fallout ratio of $(1.40 \pm 0.15) \cdot 10^{-2}$ (Hain et al. 2020).

Three outliers in the dataset, which were not included in the interpretation, show the need for further methodical optimization. The exceptionally high ^{239}Pu and ^{240}Pu concentration in the 600 m sample at CL-20 should be investigated by a re-measurement. If confirmed additional samples would also help to understand the cause of the unusual vertical distribution of plutonium in the Northeast Pacific.

The countrates of ^{233}U on sample CL-21 1500 m and ^{236}U on sample CL-21 1000 m were exceptionally high compared to the samples above and below them in the

water column and resulted in the highest $^{233}U/^{236}U$ ratio ever measured for sample CL-21 1500 m at $(59.9 \pm 6.9) \cdot 10^{-2}$. Two additional beamtimes confirmed the elevated ratio even though it declined to $(35.1 \pm 9.6) \cdot 10^{-2}$ and $(40 \pm 14) \cdot 10^{-2}$. The third beamtime used the 5+ charge state after stripping to exclude a molecular background. As the $^{233}U/^{236}U$ ratio remains very high the counts registered are indeed ^{233}U. With this possibility of surviving molecular isobars as well as a measurement problem excluded, a small contamination in the laboratory or some of the labware used remains as the most likely explanation. Preparing environmental uranium samples in a laboratory where no ^{233}U spiked samples and no samples with high ^{236}U content were ever handled might help reduce the blank level and would remove a laboratory contamination from the list of possible explanations for the problems with the CL-21 1000 m and 1500 m samples discussed in 6.2. This could also reduce the average laboratory background, which is the limiting factor for the sensitivity. Re-measuring the $^{236}U/^{238}U$ ratio of the CL-21 1000 m uranium sample could be a next step in investigating this problem.

The use of fluorides instead of oxides as target material promises increased ionization yields over oxides (Cornett et al. 2015) which besides the laboratory background is a limiting factor for further increasing the detection efficiency for actinides at VERA. This would help reduce the necessary measurement time and enable the measurement of samples with smaller volumes or even lower concentrations of the isotopes of interest, which is especially relevant for deep water ^{233}U or surface water plutonium samples. Currently, promising work is being done at VERA by Michael Kern for in-situ-fluoridation of uranium oxide during the sputtering process based on the work of (Kieser et al. 2012).

Bibliography

Alvarez, R. (2013). "Managing the Uranium 233 Stockpile of the United States". In: *Science and Global Security* 21.1, pp. 53–69. DOI: 10.1080/08929882.2013.754311.

Beasley, T. M. et al. (1984). "The inventories of plutonium-239, -240, americium-241, cesium-137, and cobalt-60 in Columbia River sediments from Hanford to the Columbia River Estuary." In: *Environmental science & technology* 18.3, pp. 207–212. DOI: 10.1021/es00121a014.

Bloch, S. (1980). "Some factors controlling the concentration of uranium in the world ocean". In: *Geochimica et Cosmochimica Acta* 44.2, pp. 373–377. DOI: 10.1016/0016-7037(80)90145-3.

Bowen, V. T. et al. (1980). "Fallout radionuclides in the Pacific Ocean: Vertical and horizontal distributions, largely from GEOSECS stations". In: *Earth and Planetary Science Letters* 49.2, pp. 411–434. DOI: https://doi.org/10.1016/0012-821X(80)90083-7.

Bressac, M. et al. (2017). "Temporal evolution of 137Cs, 237Np, and 239+240Pu and estimated vertical 239+240Pu export in the northwestern Mediterranean Sea". In: *Science of The Total Environment* 595, pp. 178–190. DOI: https://doi.org/10.1016/j.scitotenv.2017.03.137.

Bu, W. et al. (2014). "Ultra-trace plutonium determination in small volume seawater by sector field inductively coupled plasma mass spectrometry with application to Fukushima seawater samples". In: *Journal of Chromatography A* 1337, pp. 171–178. DOI: 10.1016/j.chroma.2014.02.066.

Buesseler, K. O. (1997). "The isotopic signature of fallout plutonium in the North Pacific". In: *Journal of Environmental Radioactivity* 36.1, pp. 69–83. DOI: 10.1016/S0265-931X(96)00071-9.

Casacuberta, N. et al. (2014). "A first transect of 236U in the North Atlantic Ocean". In: *Geochimica et Cosmochimica Acta* 133, pp. 34–46. DOI: 10.1016/j.gca.2014.02.012.

Castrillejo Iridoy, M. et al. (2020). "Unravelling 5 decades of anthropogenic 236U discharge from nuclear reprocessing plants". In: *Science of The Total Environment* 717, p. 137094. DOI: 10.1016/j.scitotenv.2020.137094.

Chadwick, J. (1932). "Possible existence of a neutron". In: *Nature* 129.3252, pp. 312–312. DOI: 10.1038/129312a0.

Chadwick, J. et al. (2014). "The Cobb hot spot: HIMU-DMM mixing and melting controlled by a progressively thinning lithospheric lid". In: *Geochemistry, Geophysics, Geosystems* 15.8, pp. 3107–3122. DOI: 10.1002/2014GC005334.

Chen, M.-H. et al. (2014). "Stratigraphic distribution of the radiolarian Spongodiscus biconcavus Haeckel at IODP Site U1340 in the Bering Sea and its paleoceanographic significance". In: *Palaeoworld* 23.1, pp. 90–104. DOI: https://doi.org/10.1016/j.palwor.2013.11.001.

Chen, J. H. et al. (1986). "238U, 234U and 232Th in seawater". In: *Earth and Planetary Science Letters* 80.3, pp. 241–251. DOI: https://doi.org/10.1016/0012-821X(86)90108-1.

Child, D. P. et al. (2013). "Plutonium and uranium contamination in soils from former nuclear weapon test sites in Australia". In: *Nuclear Instruments and Methods in Physics Research Section B: Beam Interactions with Materials and Atoms* 294. Proceedings of the Twelfth International Conference on Accelerator Mass Spectrometry, Wellington, New Zealand, 20-25 March 2011, pp. 642–646. DOI: https://doi.org/10.1016/j.nimb.2012.05.018.

Clark, D. (2000). "The Chemical Complexities of Plutonium". In: *Los Alamos Science: Challenges in Plutoinium Science Volume II* 26, pp. 364–381.

Cleveland, J. M. (1979). *The chemistry of plutonium*. La Grange Park, Ill.: American Nuclear Soc.

Cooper, L. W. et al. (2001). "Iodine-129 Concentrations in Marginal Seas of the North Pacific and Pacific-influenced Waters of the Arctic Ocean". In: *Marine Pollution Bulletin* 42.12, pp. 1347–1356. DOI: https://doi.org/10.1016/S0025-326X(01)00151-5.

Copernicus Marine Service (2019). *Global Ocean 1/12° Physics Analysis and Forecast updated Daily GLOBAL_ANALYSIS_FORECAST_PHY_001_024*. URL: https://view.marine.copernicus.eu/ViewService/?permalinking=true&bgmap=Blue%20Marble&dataset=http://nrt.cmems-du.eu/thredds/wms/global-analysis-forecast-phy-001-024-monthly&numColorBands=250&logScale=true&bbox=-144.60903001958,34.958248093942,-120.43910814458,52.536373093942&abovemaxcolor=0x000000&belowmincolor=0x000000&nodatacolor=null&layer=sea_water_velocity&time=2017-07-16T12%253A00%253A00.000Z&elevation=-1684.2840576171875&palette=rainbow&style=vector&scaleRange=0.0148634855,.9653645&displayScaleRange=0.0148634855,.9653645&opacity=0.75&record_id=eec7a997-c57e-4dfa-9194-4c72154f5cc5&dataset_id=Monthly%20mean%20fields%20for%20product%20GLOBAL_ANALYSIS_FORECAST_PHY_001_024 (visited on 04/20/2020).

Cornett, R. J. et al. (2015). "Actinide measurements by AMS using fluoride matrices". In: *Nuclear Instruments and Methods in Physics Research Section B: Beam Interactions with Materials and Atoms* 361. The Thirteenth Accelerator Mass Spectrometry Conference, pp. 317–321. DOI: https://doi.org/10.1016/j.nimb.2015.02.039.

Dai, M. et al. (2005). "Plutonium in groundwater at the 100K-Area of the U.S. DOE Hanford Site". In: *Journal of Contaminant Hydrology* 76.3, pp. 167–189. DOI: 10.1016/j.jconhyd.2004.08.004.

Diamond, H. et al. (1960). "Heavy Isotope Abundances in Mike Thermonuclear Device". In: *Physical Review* 119 (6), pp. 2000–2004. DOI: 10.1103/PhysRev.119.2000.

Dower, J. et al. (1992). "A strong biological response to oceanic flow past Cobb Seamount". In: *Deep Sea Research Part A. Oceanographic Research Papers* 39.7, pp. 1139–1145. DOI: https://doi.org/10.1016/0198-0149(92)90061-W.

Dower, J. F. et al. (1996). ""Seamount effects" in the zooplankton community near Cobb Seamount". In: *Deep Sea Research Part I: Oceanographic Research Papers* 43.6, pp. 837–858. DOI: https://doi.org/10.1016/0967-0637(96)00040-4.

Dunk, R. M. et al. (2002). "A reevaluation of the oceanic uranium budget for the Holocene". In: *Chemical Geology* 190.1. Geochemistry of Crustal Fluids-

Fluids in the Crust and Chemical Fluxes at the Earth's Surface, pp. 45–67. DOI: https://doi.org/10.1016/S0009-2541(02)00110-9.

Eichrom (2018). *Americium, Plutonium and Uranium in Water*. URL: https://www.eichrom.com/wp-content/uploads/2018/02/acw03-22_am-pu-u-water.pdf (visited on 04/02/2020).

Eichrom (2020a). *TEVA® Resin*. Eichrom Technologies Inc. URL: https://www.eichrom.com/eichrom/products/teva-resin/ (visited on 04/02/2020).

Eichrom (2020b). *UTEVA® Resin*. URL: https://www.eichrom.com/eichrom/products/uteva-resin/ (visited on 04/02/2020).

Eigl, R. et al. (2013). "236U/238U and 240Pu/239Pu isotopic ratios in small (2 L) sea and river water samples". In: *Journal of Environmental Radioactivity* 116, pp. 54–58. DOI: https://doi.org/10.1016/j.jenvrad.2012.09.013.

Eigl, R. et al. (2016). "First study on 236U in the Northeast Pacific Ocean using a new target preparation procedure for AMS measurements". In: *Journal of Environmental Radioactivity* 162-163, pp. 244–250. DOI: 10.1016/j.jenvrad.2016.05.025.

Eigl, R. et al. (2017). "Vertical distribution of 236U in the North Pacific Ocean". In: *Journal of Environmental Radioactivity* 169-170, pp. 70–78. DOI: https://doi.org/10.1016/j.jenvrad.2016.12.010.

Fifield, L. K. et al. (1996). "Accelerator mass spectrometry of plutonium isotopes". In: *Nuclear Instruments and Methods in Physics Research Section B: Beam Interactions with Materials and Atoms* 117.3, pp. 295–303. DOI: https://doi.org/10.1016/0168-583X(96)00287-X.

Fofnoff N. P.and Millard, R. C. (1983). *Algorithms for computation of fundamental properties of seawater*. Tech. rep. Scientific Committee on Oceanic Research, pp. 25–27.

Fowler, S. W. et al. (1983). "Vertical transport of particulate-associated plutonium and americium in the upper water column of the Northeast Pacific". In: *Deep Sea Research Part A. Oceanographic Research Papers* 30.12, pp. 1221–1233. DOI: 10.1016/0198-0149(83)90081-x.

Gebbie, G. et al. (2012). "The mean age of ocean waters inferred from radiocarbon observations: Sensitivity to surface sources and accounting for mixing histories".

In: *Journal of Physical Oceanography* 42.2, pp. 291–305. DOI: 10.1175/jpo-d-11-043.1.

GEOTRACES (2010). "Sampling and Sample-handling Protocols for GEOTRACES Cruises". In: p. 238.

Gorbachev, V. M. et al. (1980). *Nuclear reactions in heavy elements: a data handbook*. Elsevier. DOI: https://doi.org/10.1016/C2013-0-10142-0.

Gray, J. et al. (1995). "Discharges to the environment from the Sellafield site, 1951-1992". In: *Journal of Radiological Protection* 15.2, pp. 99–131. DOI: 10.1088/0952-4746/15/2/001.

Hain, K. et al. (2015). "Analytical method for the determination of Np and Pu in sea water by AMS with respect to the Fukushima accident". In: *Nuclear Instruments and Methods in Physics Research Section B: Beam Interactions with Materials and Atoms* 361. The Thirteenth Accelerator Mass Spectrometry Conference, pp. 505–509. DOI: https://doi.org/10.1016/j.nimb.2015.04.018.

Hain, K. et al. (2017). "Plutonium Isotopes (239-241Pu) Dissolved in Pacific Ocean Waters Detected by Accelerator Mass Spectrometry: No Effects of the Fukushima Accident Observed." eng. In: *Environmental science & technology* 51.4, pp. 2031–2037. DOI: 10.1021/acs.est.6b05605.

Hain, K. et al. (2020). "233U/236U signature allows to distinguish environmental emissions of civil nuclear industry from weapons fallout". In: *Nature Communications* 11.1, pp. 1–11. DOI: 10.1038/s41467-020-15008-2.

Hain, K. (2016). "Development of an ultra-sensitive detection method for transuranium elements with respect to ocean water samples from Fukushima". PhD thesis. TU München.

Hansen, C. et al. (2007). *"The swords of Armageddon"*. English. Sunnyvale, CA: Chukelea Publications.

Hickey, B. M. et al. (2019). "California and Alaska Currents". In: *Encyclopedia of Ocean Sciences (Third Edition)*. Ed. by J. K. Cochran et al. Third Edition. Oxford: Academic Press, pp. 318–329. DOI: https://doi.org/10.1016/B978-0-12-409548-9.11299-0.

Hicks, H. G. et al. (1984). *Nevada test site fallout atom ratios: 240Pu/239Pu and 241Pu/239Pu*. Tech. rep. Lawrence Livermore National Lab., CA (USA); Los Alamos National Lab., NM (USA). DOI: 10.2172/5303010.

Hong, G. H. et al. (2004). "Artificial radionuclides in the western North Pacific: a review". In: *Global environmental change in the ocean and on land*, pp. 147–172.

Horwitz, E. P. et al. (1995). "Separation and preconcentration of actinides by extraction chromatography using a supported liquid anion exchanger: application to the characterization of high-level nuclear waste solutions". In: *Analytica Chimica Acta* 310.1, pp. 63–78. DOI: https://doi.org/10.1016/0003-2670(95)00144-0.

IAEA (2006). *Environmental Consequences of the Chernobyl Accident and their Remediation: Twenty Years of Experience*. Radiological Assessment Reports Series 8. Vienna: INTERNATIONAL ATOMIC ENERGY AGENCY.

IAEA (2020). *Table of Nuclides*. URL: https://www-nds.iaea.org/relnsd/vcharthtml/VChartHTML.html (visited on 03/22/2020).

Joliot, F. et al. (1934). "Artificial Production of a New Kind of Radio-Element". In: *Nature* 133.3354, p. 201. DOI: 10.1038/133201a0.

Kieser, W. et al. (Apr. 2012). "Fluoride sample matrices and reaction cells - New capabilities for isotope measurements in accelerator mass spectrometry". In: *EPJ Web of Conferences* 24, pp. 07007–. DOI: 10.1051/epjconf/20122407007.

Koshlyakov, M. et al. (May 2004). "Pacific deep water in the Southern Ocean". In: *Oceanology* 44, pp. 299–314.

Krey, P. W. et al. (1976). *Mass isotopic composition of global fall-out plutonium in soil*. International Atomic Energy Agency (IAEA): IAEA.

Krishnaswami, S. et al. (2016). "Uranium-Thorium Radionuclides in Ocean Profiles". In: *Encyclopedia of Ocean Sciences (Third Edition)*. Ed. by J. K. Cochran et al. Third Edition. Oxford: Academic Press, pp. 377–391. DOI: https://doi.org/10.1016/B978-0-12-409548-9.09760-8.

Kusakabe, M. (2017). "Distributions of radionuclides in the ocean and their temporal changes". In: *Rep. Mar. Ecol. Res. Inst.* 22.Suppl. Pp. 3–16.

Kutschera, W. et al. (1997). "VERA: A new AMS facility in Vienna". In: *Nuclear Instruments and Methods in Physics Research Section B: Beam Interactions*

with Materials and Atoms 123.1. Accelerator Mass Spectrometry, pp. 47–50. DOI: https://doi.org/10.1016/S0168-583X(96)00782-3.

Lachner, J. et al. (Feb. 2012). "Existence of triply charged actinide-hydride molecules". In: *Physical Review A* 85. DOI: 10.1103/PhysRevA.85.022717.

Lee, S.-H. et al. (2005). "Distribution and inventories of 90Sr, 137Cs, 241Am and Pu isotopes in sediments of the Northwest Pacific Ocean". In: *Marine Geology* 216, pp. 249–263. DOI: 10.1016/j.margeo.2005.02.013.

Levine, C. A. et al. (Nov. 1950). "The occurrence of plutonium in nature". In: DOI: 10.2172/910344.

Libby, W. F. (1958). "RADIOACTIVE FALLOUT". eng. In: *Proceedings of the National Academy of Sciences of the United States of America* 44.16590276, pp. 800–820. DOI: 10.1073/pnas.44.8.800.

Lindahl, P. et al. (2005). "Studies of Np and Pu in the marine environment of Swedish–Danish waters and the North Atlantic Ocean". eng. In: *Journal of Environmental Radioactivity* 82.3, pp. 285–301. DOI: 10.1016/j.jenvrad.2005.01.011.

Lindahl, P. et al. (2010). "Plutonium isotopes as tracers for ocean processes: A review". eng. In: *Marine Environmental Research* 69.2, pp. 73–84. DOI: 10.1016/j.marenvres.2009.08.002.

Litherland, A. E. et al. (1981). "Ultra-sensitive mass spectrometry with tandem accelerators". In: *Nuclear Instruments and Methods in Physics Research* 186.1, pp. 463–477. DOI: https://doi.org/10.1016/0029-554X(81)90941-1.

Livingston, H. D. et al. (2001). "The behaviour of plutonium in the Pacific Ocean". In: *Plutonium in the Environment*. Ed. by A. Kudo. Vol. 1. Radioactivity in the Environment. Elsevier, pp. 267–292. DOI: https://doi.org/10.1016/S1569-4860(01)80019-X.

Lòpez Lora, M. (2019). "Low-Energy Accelerator Mass Spectrometry of actinides (236U, 237Np, 239, 240Pu) at the Centro Nacional de Aceleradores and its applications in oceanography". PhD thesis. Universidad de Sevillia.

Loughlin, T. R. et al., eds. (1999). *Dynamics of the Bering Sea : a summary of physical, chemical, and biological characteristics, and a synopsis of research on the Bering Sea*. Fairbanks, Alaska : University of Alaska Sea Grant College Program Report.

Lovett, M. B. et al. (1990). *The determination of alpha-emitting nuclides of plutonium, americium and curium in environmental materials: Part 1. Sea water*. Vol. 7. MAFF, Directorate of Fisheries Research Lowestoft, UK.

Madland, D. G. (1982). *New Fission Neutron Spectrum Representations for ENDF*. Tech. rep. DOI: 10.2172/5187521.

Mahmoud, M. A. (2018). "Adsorption of U (VI) ions from aqueous solution using silicon dioxide nanopowder". In: *Journal of Saudi Chemical Society* 22.2, pp. 229–238. DOI: https://doi.org/10.1016/j.jscs.2016.04.001.

Martschini, M. et al. (2019). "The ILIAMS project – An RFQ ion beam cooler for selective laser photodetachment at VERA". In: *Nuclear Instruments and Methods in Physics Research Section B: Beam Interactions with Materials and Atoms* 456, pp. 213–217. DOI: https://doi.org/10.1016/j.nimb.2019.04.039.

Meitner, L. et al. (1939). "Disintegration of Uranium by Neutrons: a New Type of Nuclear Reaction". In: *Nature* 143.3615, pp. 239–240. DOI: 10.1038/143239a0.

Middleton, R. (1983). "A versatile high intensity negative ion source". eng. In: *Nuclear Instruments and Methods In Physics Research* 214.2, pp. 139–150. DOI: 10.1016/0167-5087(84)90416-2.

Middleton, R. et al. (Nov. 1999). "Production of metastable negative ions in a cesium sputter source: Verification of the existence of N_2^- and CO^-". In: *Phys. Rev. A* 60 (5), pp. 3786–3799. DOI: 10.1103/PhysRevA.60.3786.

Morss, L. R. et al. (2011). *The Chemistry of the Actinide and Transactinide Elements, 4th Edition (Volumes 1–6)*. 4th ed. Vol. Vol. 1. Springer. Chap. Chapter 5. DOI: 10.1007/978-94-007-0211-0.

Naegeli, R. E. (June 2004). "Calculation of the radionuclides in PWR spent fuel samples for SFR experiment planning." In: DOI: 10.2172/919122.

Nakano, M. et al. (2003). "Modelling the distribution of plutonium in the Pacific Ocean". In: *Journal of environmental radioactivity* 69.1-2, pp. 85–106. DOI: 10.1016/s0265-931x(03)00088-2.

Owens, S. A. et al. (2011). "Re-evaluating the 238U-salinity relationship in seawater: Implications for the 238U–234Th disequilibrium method". In: *Marine Chemistry* 127.1, pp. 31–39. DOI: https://doi.org/10.1016/j.marchem.2011.07.005.

Peppard, D. F. et al. (1952). "Occurrence of the (4n + 1) Series in Nature". In: *Journal of the American Chemical Society* 74.23, pp. 6081–6084. DOI: 10.1021/ja01143a074.

Perruche, C. et al. (2018). *Global ocean biogeochemistry hindcast*. Copernicus Marine Environment Monitoring Service. URL: https://resources.marine.copernicus.eu/?option=com_csw&task=viewer&record_id=9fe675d9-794a-46a1-abcb-471fa4279d2b (visited on 05/11/2020).

Piana, M. E. (2020). *Hadley Cells*. Harvard School of Engeneering and Applied Sciences. URL: https://www.seas.harvard.edu/climate/eli/research/equable/hadley.html (visited on 06/14/2020).

Qiao, J. et al. (2015). "Method for 236U Determination in Seawater Using Flow Injection Extraction Chromatography and Accelerator Mass Spectrometry". In: *Analytical Chemistry* 87.14. PMID: 26105019, pp. 7411–7417. DOI: 10.1021/acs.analchem.5b01608.

Reid Jr., J. L. (1962). "On circulation,phosphate-phosphorus content, and zooplankton volumes in the upper part of the Pacific Ocean". In: *Limnology and Oceanography* 7.3, pp. 287–306. DOI: 10.4319/lo.1962.7.3.0287.

Rella, S. et al. (Feb. 2014). "A Southern Ocean trigger for Northwest Pacific ventilation during the Holocene?" In: *Scientific reports* 4, p. 4046. DOI: 10.1038/srep04046.

Runde, W. H. (2000). "The chemical interactions of actinides in the environment". In: *Los Alamos Science* 26, pp. 392–411. DOI: 10.2136/sssaspecpub59.c2.

Sakaguchi, A. et al. (2009). "First results on U levels in global fallout". In: *The Science of the total environment* 407, pp. 4238–42. DOI: 10.1016/j.scitotenv.2009.01.058.

Sakaguchi, A. et al. (2012). "Uranium-236 as a new oceanic tracer: A first depth profile in the Japan Sea and comparison with caesium-137". In: *Earth and Planetary Science Letters* 333-334, pp. 165–170. DOI: 10.1016/j.epsl.2012.04.004.

Sakaguchi, A. et al. (2014). "Isotopic Compositions of 236U and Pu Isotopes in "Black Substances" Collected from Roadsides in Fukushima Prefecture: Fallout from the Fukushima Dai-ichi Nuclear Power Plant Accident". In: *Environmental Science & Technology* 48.7. PMID: 24601520, pp. 3691–3697. DOI: 10.1021/es405294s.

Salmani-Ghabeshi, S. et al. (Dec. 2018). "Presence of (236)U and (239)(,240)Pu in soils from Southern Hemisphere." eng. In: *Journal of environmental radioactivity* 192, pp. 478–484. DOI: 10.1016/j.jenvrad.2018.08.003.

Seaborg, G. T. et al. (1946). "Radioactive element 94 from deuterons on uranium". In: *Physical Review* 69.7-8, p. 366. DOI: 10.4159/harvard.9780674366701.c83.

Simon, S. L. et al. (1999). "Concentrations and spatial distribution of plutonium in the terrestrial environment of the Marshall Islands". In: *Science of the total environment* 229.1-2, pp. 21–39. DOI: https://doi.org/10.1016/S0048-9697(99)00066-2.

Steier, P. (2000). "Exploring the limits of VERA. PhD thesis". PhD thesis. University of Vienna.

Steier, P. et al. (2004). "VERA, an AMS facility for „all" isotopes". In: *Nuclear Instruments and Methods in Physics Research Section B: Beam Interactions with Materials and Atoms* 223-224, pp. 67–71. DOI: 10.1016/j.nimb.2004.04.017.

Steier, P. et al. (2019). "The actinide beamline at VERA". In: *Nuclear Instruments and Methods in Physics Research Section B: Beam Interactions with Materials and Atoms* 458, pp. 82–89. DOI: 10.1016/j.nimb.2019.07.031.

Steier, P. et al. (2008). "Natural and anthropogenic 236U in environmental samples". In: *Nuclear Instruments and Methods in Physics Research Section B: Beam Interactions with Materials and Atoms* 266.10. Accelerators in Applied Research and Technology, pp. 2246–2250. DOI: 10.1016/j.nimb.2008.03.002.

Sublette, C. (2020). *The nuclear weapon archive - a guide to nuclear weapons.* URL: https://nuclearweaponarchive.org/Usa/Tests/Teapot.html (visited on 02/20/2020).

Talley, L. D. (2011). *Descriptive physical oceanography : an introduction.* eng. 6th ed. London : Academic Press, DOI: https://doi.org/10.1016/C2009-0-24322-4.

Taylor, P. et al. (2000). *Certificate spike isotopic reference material IRMM-85.* IRRM. URL: https://crm.jrc.ec.europa.eu/p/40454/40475/By-application-field/Nuclear/IRMM-085-PLUTONIUM-242-SPIKE-NITRATE-SOLUTION/IRMM-085 (visited on 02/08/2020).

Triskem International (2015). *Produktblatt TEVA Resin*. URL: https://www.triskem-international.com/scripts/files/5c5991c195acf8.90467917/PS_TEVA-Resin_DE_160927.pdf (visited on 02/09/2020).

Tsaletka, R. et al. (1960). "Occurence of the transuranium elements in nature". In: *Russian Chemical Reviews* 29.12, pp. 684–689. DOI: 10.1070/rc1960v029n12abeh001264.

UN, ed. (2000). *Sources and effects of ionizing radiation: United Nations Scientific Committee on the Effects of Atomic Radiation: UNSCEAR 2000 report to the General Assembly, with scientific annexes*. New York: United Nations, p. 160.

Villa-Alfageme, M. et al. (2019). "Distribution of 236U in the U.S. GEOTRACES Eastern Pacific Zonal Transect and its use as a water mass tracer". In: *Chemical Geology* 517, pp. 44–57. DOI: https://doi.org/10.1016/j.chemgeo.2019.04.003.

Vockenhuber, C. et al. (2002). "Accelerator mass spectrometry of the heaviest long-lived radionuclides with a 3-MV tandem accelerator". In: *Pramana* 59.6, pp. 1041–1051. DOI: 10.1007/s12043-002-0154-9.

Vockenhuber, C. et al. (2011). "Accelerator mass spectrometry of 236U at low energies". In: *Nuclear Instruments and Methods in Physics Research Section B: Beam Interactions with Materials and Atoms* 269.24. Proceedings of the 10th European Conference on Accelerators in Applied Research and Technology (ECAART10), pp. 3199–3203. DOI: https://doi.org/10.1016/j.nimb.2011.04.026.

Vogel, J. (Feb. 2016). "Anion formation in sputter ion sources by neutral resonant ionization". In: *Review of Scientific Instruments* 87, 02A504. DOI: 10.1063/1.4934618.

Wang, X. et al. (2013). "Determination of cross sections for the 238U(n,3n)236U reaction induced by 14-MeV neutrons with accelerator mass spectrometry". In: *Phys. Rev. C* 87 (1), p. 014612. DOI: 10.1103/PhysRevC.87.014612.

Webb, P. (2019). *Introduction to Oceanography*. Rebus Community, pp. 210–213.

Wilcock, W. S. D. et al. (2018). "The Recent Volcanic History of Axial Seamount: Geophysical Insights into Past Eruption Dynamics with an Eye Toward Enhanced Observations of Future Eruptions". In: *Oceanography* 31.1, pp. 114–123. DOI: https://doi.org/10.5670/oceanog.2018.117.

Wilson, R. C. et al. (2009). "Laboratory and field studies of polonium and plutonium in marine plankton". In: *Journal of Environmental Radioactivity* 100.8, pp. 665–669. DOI: https://doi.org/10.1016/j.jenvrad.2009.05.007.

Winkler, S. R. et al. (2012). "Bomb fall-out 236U as a global oceanic tracer using an annually resolved coral core". In: *Earth and Planetary Science Letters* 359-360, pp. 124–130. DOI: 10.1016/j.epsl.2012.10.004.

Winkler, S. R. et al. (2015). "He stripping for AMS of 236U and other actinides using a 3MV tandem accelerator". In: *Nuclear Instruments and Methods in Physics Research Section B: Beam Interactions with Materials and Atoms* 361. The Thirteenth Accelerator Mass Spectrometry Conference, pp. 458–464. DOI: https://doi.org/10.1016/j.nimb.2015.04.029.

Wu, J. et al. (2019). "Plutonium in the western North Pacific: Transport along the Kuroshio and implication for the impact of Fukushima Daiichi Nuclear Power Plant accident". In: *Chemical Geology* 511, pp. 256–264. DOI: 10.1016/j.chemgeo.2018.12.006.

Yamada, M. et al. (Feb. 2007). "240Pu/239Pu atom ratios in seawater from Sagami Bay, western Northwest Pacific Ocean: sources and scavenging". In: *Journal of environmental radioactivity* 98, pp. 274–84. DOI: 10.1016/j.jenvrad.2007.05.005.

Yamada, M. et al. (2020). "240Pu/239Pu atom ratios in water columns from the North Pacific Ocean and Bering Sea: Transport of Pacific Proving Grounds-derived Pu by ocean currents". In: *Science of The Total Environment* 718, p. 137362. DOI: https://doi.org/10.1016/j.scitotenv.2020.137362.

Yang, G. et al. (2017). "Isotopic compositions of 236U, 239Pu, and 240Pu in soil contaminated by the Fukushima Daiichi Nuclear Power Plant accident". In: *Scientific Reports* 7.1, p. 13619. DOI: 10.1038/s41598-017-13998-6.

Zachara, J. M. et al. (2007). *A Site Wide Perspective on Uranium Geochemistry at the Hanford Site*. Tech. rep. Pacific Northwest National Laboratory (PNNL), Richland, WA (US), Environmental Molecular Sciences Laboratory (EMSL). DOI: 10.2172/920206.

Zhao, X.-L. et al. (1997). "AMS measurement of environmental U-236 Preliminary results and perspectives". In: *Nuclear Instruments and Methods in Physics Research Section B: Beam Interactions with Materials and Atoms* 126.1. In-

ternational Conference on Electromagnetic Isotope Separators and Techniques Related to Their Applications, pp. 297–300. DOI: 10.1016/S0168-583X(96)01034-8.

Zheng, J. et al. (Dec. 2006). "Vertical distribution of uranium concentrations and 235U/238U atom ratios in the coastal water off Aomori, Japan: A survey prior to the operation of a nuclear fuel reprocessing facility". In: *Journal of Radioanalytical and Nuclear Chemistry* 270. DOI: 10.1007/s10967-006-0446-5.

Zheng, J. et al. (2012). "Isotopic evidence of plutonium release into the environment from the Fukushima DNPP accident". In: *Scientific Reports* 2.1, p. 304. DOI: 10.1038/srep00304.

List of Tables

List of Figures

8 Appendix

Name	Spike (in 10^8 ^{242}Pu atoms)
CL-21_0	2.879 ± 0.026
CL-21_20	3.265 ± 0.026
CL-21_60	2.803 ± 0.026
CL-21_100	3.183 ± 0.026
CL-21_200	2.799 ± 0.026
CL-21_300	3.002 ± 0.026
CL-21_500	3.102 ± 0.026
CL-21_800	3.130 ± 0.026
CL-21_1000	2.929 ± 0.026
CL-21_1500	2.985 ± 0.026
CL-21_2000	3.120 ± 0.026
CL-21_2500	3.061 ± 0.026
CL-21_3000	2.661 ± 0.026
CL-21_3087	2.953 ± 0.026
CL-20_0	2.601 ± 0.026
CL-20_300	2.892 ± 0.026
CL-20_400	2.908 ± 0.026
CL-20_600	3.056 ± 0.026

Table 8.0.3: Number of ^{242}Pu atoms used as spike for each sample

depth (m)	^{236}U (cps)	^{236}U (cts)	^{233}U (10^{-3} cps)	^{233}U (cts)
B5U	0.0387 ± 0.0057	47	0.243 ± 0.162	3
-400	0.641 ± 0.035	387	8.3 ± 1.3	57
B6U	0.0290 ± 0.0056	28	0.93 ± 0.33	9
0	1.095 ± 0.040	749	$12,32 \pm 1.34$	85
-300	1.186 ± 0.033	1315	13.82 ± 1.13	150
-600	0.717 ± 0.027	698	6.21 ± 0.81	60

Table 8.0.1: Average countrates (cps) and total number of detected counts (cts) for ^{236}U and ^{233}U for the CL-20 samples and corresponding blanks.

depth (m)	Batch	^{236}U (cps)	^{236}U (cts)	^{233}U (10^{-2} cps)	^{233}U (cts)
B1U	1	0.0089 ± 0.0028	11	0.185 ± 0.040	23
-20	1	0.776 ± 0.039	526	3.740 ± 0.142	94
-300	1	0.695 ± 0.032	476	0.702 ± 0.102	48
-2000	1	0.0329 ± 0.0067	25	0.342 ± 0.066	28
B2U	2	0.2893 ± 0.0169	293	0.585 ± 0.076	60
-100	2	8.804 ± 0.093	9003	19.50 ± 0.44	1989
-500	2	1.648 ± 0.038	1931	2.246 ± 0.137	271
-1000	2	13.205 ± 0.103	16289	0.670 ± 0.074	82
B3U	3	0.0232 ± 0.0045	27	0.223 ± 0.044	27
-60	3	2.655 ± 0.052	2662	5.84 ± 0.24	598
-800	3	1.341 ± 0.033	1664	2.346 ± 0.138	290
-1500	3	0.288 ± 0.015	348	18.06 ± 0.38	2210
B4U	4	0.0940 ± 0.0099	91	1.269 ± 0.114	125
0	4	4.457 ± 0.066	4583	5.11 ± 0.22	525
-2500	4	0.0498 ± 0.0079	41	0.109 ± 0.038	9
-3000	4	0.1038 ± 0.0086	147	0.634 ± 0.067	90
B5U	5	0.0387 ± 0.0057	47	0.00243 ± 0.00162	3
-200	5	1.190 ± 0.038	992	1.458 ± 0.133	121
-3087	5	0.0224 ± 0.0047	24	0.0091 ± 0.0030	10

Table 8.0.2: Average countrates (cps) and total number of detected counts (cts) for ^{236}U and ^{233}U for the CL-21 samples and corresponding blanks.

AMS	Accelerator Mass Spectrometry
GF	Global Fallout
IAEA	International Atomic Energy Association
IRMM	Institute for Reference Materials and Measurements
LCDW	Lower Circumpolar Deep Water
NPP	Nuclear Power Plant
PDW	Pacific Deep Water
PIXE	Particle Induced X-ray Emission
PPG	Pacific Proving Grounds
PUREX	Plutonium Uranium Reduction Extraction
(SF-)ICP-MS	(Sector Field) Inductively Coupled Plasma Mass Spectrometry
SNICS	Source of Negative Ions by Cesium Sputtering
TOF	Time Of Flight
VERA	Vienna Environmental Research Accelerator

Table 8.0.4: List of abbreviations